12-2017

Characterization of Porosity Defects in Selectively Laser Melted IN718 and Ti- 6A1-4V via Synchrotron X-Ray Computed Tomography

Alexander William Finch
Purdue University

CHARACTERIZATION OF POROSITY DEFECTS IN SELECTIVELY LASER MELTED IN718 AND TI-6AL-4V VIA SYNCHROTRON X-RAY COMPUTED TOMOGRAPHY

by

Alexander William Finch

A Thesis

Submitted to the Faculty of Purdue University

In Partial Fulfillment of the Requirements for the degree of

Master of Science in Aeronautics and Astronautics

School of Aeronautics and Astronautics

West Lafayette, Indiana

December 2017

THE PURDUE UNIVERSITY GRADUATE SCHOOL
STATEMENT OF COMMITTEE APPROVAL

Dr. Michael Sangid, Chair

School of Aeronautics and Astronautics

Dr. Timothee Pourpoint

School of Aeronautics and Astronautics

Dr. Alberto Mello

School of Aeronautics and Astronautics

Approved by:

Dr. Weinong Chen

Head of the Graduate Program

Visualize and achieve.

ACKNOWLEDGEMENTS

Numerous individuals have assisted me in this research endeavor and I am entirely grateful to them for their support. First, I would like to express my gratitude to my advisor, Dr. Michael Sangid, for providing me the opportunity to conduct research as part of the well-respected and highly intelligent ACME^2 laboratory group and for providing me with a project that has a meaningful impact on my interests in the aerospace field. Under Dr. Sangid's guidance and direction, the ACME^2 lab group functions as a productive team and has been a truly integral part of my experience at Purdue University. Thank you to all of my lab mates who I have had the pleasure of learning from and working with, and who I have the utmost confidence in to make significant impacts on the scientific and engineering communities. I would like to mention my utmost gratitude to the GEM Fellowship, for providing me the financial ability to pursue my Master's degree as well as the professional opportunity to work in the aerospace industry. Additionally, I would like to acknowledge the supporting research funding from DARPA (N66001-14-1-4041) under program manager M. Maher and J. Vanderbrande and team: J. Margiotta, D. Cheng, D. Schesser, W. Roy, J. Williams, and B. Cowles. Special mention to R. Martukanitz and K. Meinert at Penn State University's Center for Innovative Materials Processing through Direct Digital Deposition (CIMP-3D) for manufacturing the specimens, Dr. Todd Book for designing and preparing the samples, Dr. Michael Sangid and Peter Coutts of CIMP-3D for scanning the samples, and Dr. Xianghui Xiao at 2-BM of the Advanced Photon Source at Argonne National Laboratory for assistance in tomography. Thank you to my committee: Dr. Michael Sangid, Dr. Alberto Mello, and Dr. Timothee Pourpoint, for taking

the time to receive and review my work. Special mention to Ms. Susan Fisher, Purdue University's GEM coordinator, for her encouragement and assistance in navigating graduate education. Last but certainly not least, I would like to express my indebtedness to my friends, family, and loved ones for providing unwavering support throughout this academic pursuit. I would like to specifically mention my close comrades at Purdue University, including Lt. Daniel Chadwick, Deepak Atyam, Priya Ravi, Eugene Kim, and Arly Black for all the good times.

TABLE OF CONTENTS

LIST OF TABLES

LIST OF FIGURES

LIST OF EQUATIONS

LIST OF ABBREVIATIONS

In order of appearance:

AM – Additively Manufactured

SLA – Stereolithography

SLS – Selective Laser Sintering

SLM – Selective Laser Melting

EBM – Electron Beam Melting

Ti64 – Ti-Al6-V4 Alloy

IN718 – Inconel 718 Alloy

CT – Computed Tomography

HIP – Hot Isostatic Pressing

HT – Heat Treatment

PSU – Pennsylvania State University

CIMP-3D – Center for Innovative Materials Processing through Direct Digital Deposition

DMLS – Direct Metal Laser Sintering

SR – Stress Relieved

APS – Advanced Photon Source at Argonne National Laboratory

LR – Low Resolution Data Set (30 μm voxel size)

HR – High Resolution Data Set (0.65 μm voxel size)

GUI – Graphical user interface

CDF – Cumulative Distribution Function

CIMP-3D – Center for Innovative Materials Processing through Direct Digital Deposition

PDF – Probability Distribution Function

RLP – Random Large Pore

ABSTRACT

Author: Finch, Alexander, W., MSAAE
Institution: Purdue University
Degree Received: December 2017
Title: Characterization of Porosity Defects in Selectively Laser Melted IN719 and Ti-6Al-4V Via Synchrotron X-Ray Computed Tomography
Major Professor: Michael Sangid

Additive manufacturing (AM) is a method of fabrication involving the joining of feedstock material together to form a structure. Additive manufacturing has been developed for use with polymers, ceramics, composites, biomaterials, and metals. Of the metal additive manufacturing techniques, one of the most commonly employed for commercial and government applications is selective laser melting (SLM). SLM operates by using a high-powered laser to melt feedstock metal powder, layer by layer, until the desired near-net shape is completed. Due to the inherent function of AM and particularly SLM, it holds much promise in the ability to design parts without geometrical constraint, cost-effectively manufacture them, and reduce material waste. Because of this, SLM has gained traction in the aerospace, automotive, and medical device industries, which often use uniquely shaped parts for specific functions. These industries also have a tendency to use high performance metallic alloys that can withstand the sometimes-extreme operating conditions that the parts experience. Two alloys that are often used in these parts are Inconel 718 (IN718) and Ti-6Al-4V (Ti64). Both of these materials have been routinely used in SLM processing but have been often marked by porosity defects in the as-built state. Since large amounts of porosity is known to limit material mechanical performance, especially in fatigue life, there is a general need to inspect and quantify this material characteristic before part use in these industries. One of the most advanced porosity inspection methods is via X-ray computed tomography (CT). CT uses a detector to capture scattered X-rays after passing through the part. The detector images are then reconstructed to create a tomograph that can be analyzed using image processing techniques to visualize and quantify porosity. In this research, CT was performed on both materials at a 30 μm "low resolution" (LR) for different build orientations and processing conditions.

Furthermore, a synchrotron beamline was used to conduct CT on small samples of the SLM IN718 and Ti64 specimens at a 0.65 μm "high resolution" (HR), which to the author's knowledge is the highest resolution (for SLM IN718) and matches the highest resolution (for SLM Ti64) reported for porosity CT investigations of these materials. Tomographs were reconstructed using TomoPy 1.0.0, processed using ImageJ and Avizo 9.0.2, and quantified in Avizo and Matlab. Results showed a relatively low amount of porosity in the materials overall, but a several order of magnitude increase in quantifiable porosity volume fraction from LR to HR observations. Furthermore, quantifications and visualizations showed a propensity for more and larger pores to be present near the free surfaces of the specimens. Additionally, a plurality of pores in the HR samples were found to be in close proximity (10 μm or less) to each other.

CHAPTER 1. INTRODUCTION

Additive manufacturing (AM), colloquially termed “3D printing”, is a fabrication process that builds up objects from joining materials together, usually directly from 3D model data [1]. The novelty of AM is clear when contrasted against more conventional subtractive manufacturing techniques, such as machining and stamping, which operate by removing or forming material until the desired object shape is achieved. AM is different from conventional manufacturing, in that the process adds materials together, usually layer-by-layer, until a near-net shape is achieved. Furthermore, AM is enabled directly from computer aided design 3D models, without necessitating any additional tooling or molds [2]. This inherent benefit of AM allows for the efficient creation of geometrically complex parts that can unlock the potential of design optimization, without regard for traditional manufacturing constraints [1]. As such, many products that once required the joining of many different subcomponents can now be created through consolidation into a single object, which increases manufacturing efficiency and potentially reduces operational failure modes [1]. Additionally, AM also has the potential to revolutionize the supply chain for final end-use parts by providing an onsite manufacturing unit for components that are not kept in large inventory, bringing products to the end user faster and using fewer resources [1]. Furthermore, AM has the potential to minimize the waste of raw materials through efficient use of feedstock to create a desired geometry [1][3]. Overall, AM has transformative qualities that make it an attractive solution for many issues associated with manufacturing; however, due to some persistent issues with AM parts in their as-built state, more development work is required for this technology to reach its full societal impact potential.

AM development began in the 1980s, with a wide range of progress made since then [1][3][2]. In the past 20+ years, new ideas have sprouted, numerous patents awarded, and new techniques have been invented and commercialized [3]. According to Levy et al., stereolithography was the first AM technique developed [3]. Stereolithography (SLA) is a layer-by-layer process based on solidification of a liquid plastic monomer through photo-polymerization, where illumination of the liquid layer is in the form of a pattern corresponding to the part cross section [4]. Following the invention of SLA, other AM forms allowing for the incorporation of more materials were developed. One of the earliest AM techniques that enabled the fabrication of metal parts was selective laser sintering (SLS) [3]. SLS is a powder bed-based process where a high powered laser is used to sinter the material powder particles together in the cross sectional shape of the object [1][3][4]. Another layer of the powder is applied and the process is repeated until a final object is built. The SLS technique can also be used to manufacture plastics, ceramics, or polymer substances [5]. The development of SLS gave way to the similar process, selective laser melting (SLM), which operates in the same manner as SLS except that the material powder is fully melted, as opposed to sintered [6]. SLM development was aimed at reducing the porosity content prevalent in many early SLS-made parts [7][8][9]. Building off of the success of SLM, another metal AM powder bed fabrication process, electron beam melting (EBM), was invented [10]. EBM operates similarly to SLM with differences being that material powder is melted by a directed electron beam operating in a vacuum. A note to make is that SLS and SLM are highly similar techniques, and in some cases, SLS machines enact SLM processes by fully melting the powder [4]. For simplification purposes of this research, the metal SLS and SLM processes will be consolidated, verbally, and solely

referred to as SLM. In general, metal powder bed AM processes can be viewed in contrast to metal wire feed systems, which also have the ability to build up metal structures in an additive fashion. Wire feed systems, such as Three Dimensional Welding or Electron Beam Solid Freeform Fabrication, utilize a wire feedstock to deposit material while the energy source (which can be a gas metal arc welder, laser beam, electron beam, or other) liquefies the feedstock, depositing it in layers to form a 3D structure [11][12]. The main benefit of wire feed systems is that they are often characterized by a high deposition rate and have larger build volumes than powder bed systems. However, the downside to wire feed metal AM is that the as-built structure usually requires more extensive post-processing to reach net shape than powder bed systems [11]. As such, powder bed systems are more often utilized for aerospace components, which usually require a high geometrical tolerance. For the purpose of this research, which is aerospace focused in potential and application, powder bed processes are the area of focus, specifically SLM.

AM use has grown since initial inception. SLS, SLM, and EBM are currently the most common metal AM techniques and are widely used throughout several industries. Figure 1 shows the progression of AM into different industries and applications. Guo and Leu described how researchers were the first ones to develop new AM processes and apply them in fields such as aerospace, automotive, biomedical, digital art, and architectural design, among others [2]. However, more recently, industry itself has been the driving force that allowed metal AM to go from a rapid prototype fabrication technique, to rapid tooling and manufacturing [13]. Early industrial applications of metal AM were visual aids and form evaluation and fit assessment tools [2]. Later, progress in metal AM allowed for the use of prototype and low volume quantities of end-use products [2]. However, with

increased effort in research and development for AM materials, processes, software, equipment, and standards, metal AM applications have evolved to be the primary manufacturing method for numerous end-use parts and products [2][1].

This timeline lays out past, present and potential future AM developments and applications.
(courtesy of Graham Tromans)

1988-1994	rapid prototyping
1994	rapid casting
1995	rapid tooling
2001	AM for automotive
2004	aerospace (polymers)
2005	medical (polymer jigs and guides)
2009	medical implants (metals)
2011	aerospace (metals)
2013-2016	nano-manufacturing
2013-2017	architecture
2013-2018	biomedical implants
2013-2022	in situ bio-manufacturing
2013-2032	full body organs

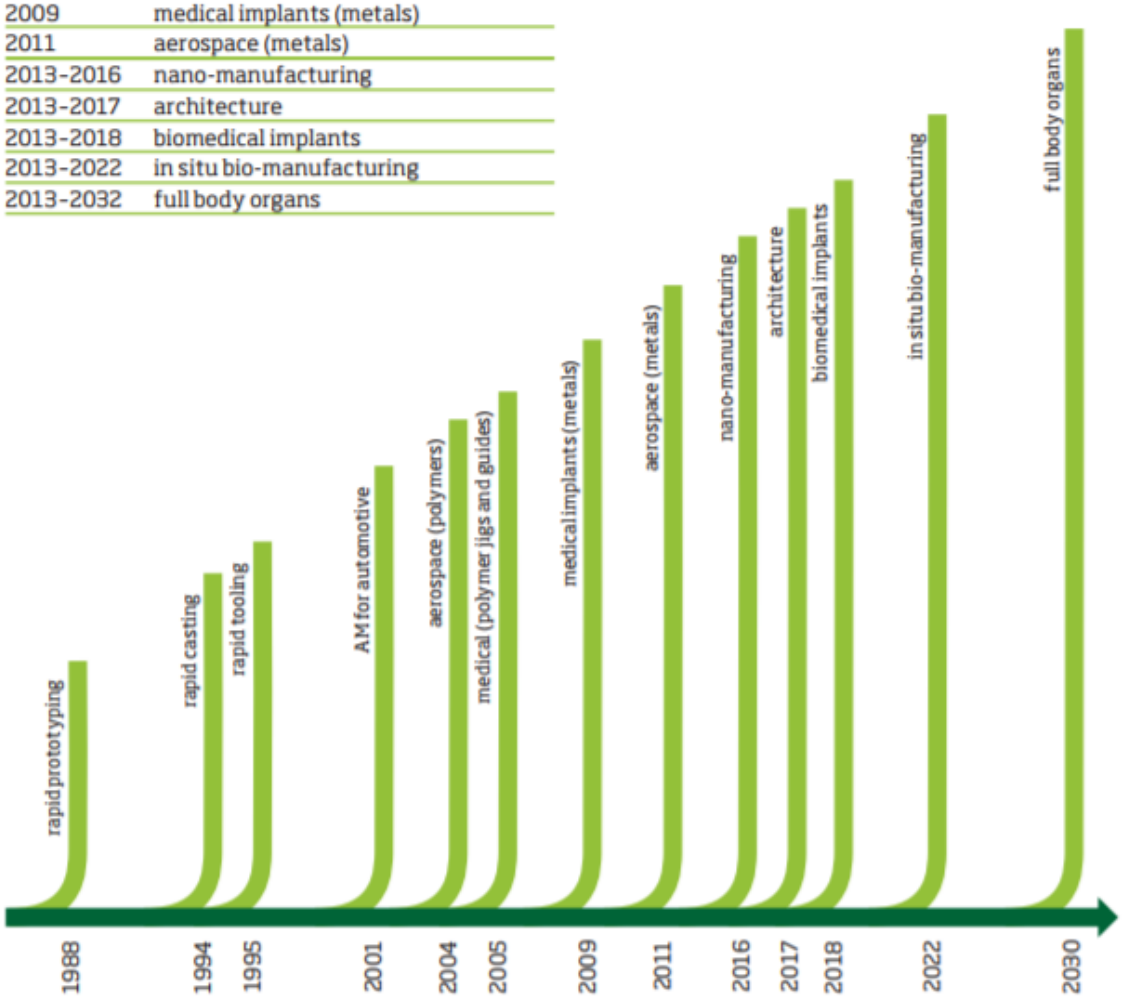

Figure 1: AM applications timeline [14]

Several metal AM product development projects taking place are within the aerospace industry utilizing high temperature resistant nickel and titanium alloys. Lockheed Martin has been pursuing the incorporation of AM for Ti-6Al-4V (Ti64) parts on the F-35 Joint Strike Fighter, including the CTOL/STOVL Flaperon Spar [11]. The launch vehicle manufacturer, SpaceX, announced in 2013 that their SuperDraco rocket engine chamber was created via SLM of an Inconel superalloy, as seen in Figure 2 [15]. The U.S. Army has investigated repair of Inconel 625 3rd stage turbine blades using metal AM [16]. Additionally, Frazier further describes other projects including EBM of a Ti64 airframe component and deposition of Inconel 718 (IN718) features on a forged engine case [11].

Figure 2: SpaceX SuperDraco rocket chamber emerging from build chamber [17]

IN718 and Ti64 are two of the more popular metal alloys used in AM within the aerospace industries, specifically because they are attractive material choices for current AM applications of engine and other low volume, high geometric complexity parts. IN718 is a precipitation hardened Ni-based superalloy. The material has the desired ability to

retain mechanical properties in elevated temperature environments and exhibits excellent resistance to oxidation as well as positive weldability [18]. Furthermore, the superalloy has outstanding combinations of strength, toughness, and crack initiation [19]. Traditionally, IN718 has been manufactured using conventional melting and casting techniques [18]. Ti64 is a Ti-based alloy that is "characterized by its high strength, low density, high corrosion resistance, and good biocompatibility", according to Leuders et al. [20]. Ti64 also has the ability to retain high specific strength at elevated temperatures [21]. According to Book, Ti64 represents over half of all titanium alloys currently produced [19].

Though the use of AM (and specifically SLM) holds many benefits for metal part production, there are still persistent issues that limit its use as a standalone manufacturing process, especially for structurally critical components. Generally, in his overview of AM technologies, Frazier provided areas for desired improvement in metal AM, including [11]:

- process monitoring and control
- reducing variability in properties of as-built parts
- physics based models to connect build parameters with material properties and performance
- use of validated models to decrease the amount of physical part qualification required
- shared material property databases
- integrated structural design tools
- new alloys that optimize properties inherent from the AM process

More specifically, multiple researchers have described the common issues seen in as-built SLM Ni-based superalloys and Ti-based alloys. First, in both materials, as-built parts are characterized by high surface roughness as compared to conventionally manufactured parts [7][22]. Furthermore, Qiu et al. surveyed different research to find that the issues observed in these materials also consisted of cracking, residual stresses caused by high thermal gradients that are inherent with the rapid melting and cooling of SLM, columnar grain structures, greatly textured microstructures, anisotropy in mechanical properties, and porosity defects [23].

This research focuses on the characterization of porosity defects in SLM IN718 and Ti64. Specifically, the aim of this research is to observe porosity utilizing synchrotron-based microscale X-ray computed tomography (CT) as well as commercially available CT to characterize the material defects at resolutions of 0.65 μm and 30 μm per pixel, respectively. While CT has been used previously in both research and industry to characterize porosity, to the author's knowledge, no study has compared the results obtained at one resolution (30 μm/pixel) with another as high as 0.65 μm per pixel. What this comparison allows for is two contributions to the community: for SLM IN718 and Ti64, 1) the observation and characterization of porosity content that is unaccounted for by lower resolution inspections and 2) specifically the characterization of SLM IN718 porosity defects at a resolution of 0.65 μm per pixel, which to the author's knowledge has not been explored. Porosity trends will be identified and placed in a greater context to the potential impact on industrial usage and future research aims.

CHAPTER 2. LITERATURE REVIEW

2.1 Porosity

Porosity is a quality of a material defined as the ratio of the volume of voids present to the volume of the material mass [24]. Porosity is a material defect present in structures, resulting from different types of metallic manufacturing techniques and has previously been widely observed and characterized in cast, welded, powder metallurgical, and forged metals [25][26][27][28][29][30][31]. The presence of porosity defects in solid metals is known to cause a reduction of mechanical properties, as compared to fully defense materials [32][33][34][35]. Specifically for fatigue life, porosity can have a large influence on part mechanical performance. In cast metals, porosity was shown to be the largest influencing factor on fatigue properties when the pore size and quantity exceeded certain critical values [26][27][36]. If pore size and amount were kept below critical values, then the next most dominant factor became operational, as it related to fatigue life [36]. Porosity features have previously been reported and critical defect sizes that influence fatigue life determined for a variety of metal manufacturing methods, displayed in Table 1, to gain a general understanding of the size of singular pores that are currently accepted to be of concern. As a note, the critical defect size was determined by pinpointing the inflection point of the displayed Kitagawa diagram (schematic shown in Figure 5) and reporting the corresponding defect size at that location, per respective reference. Though it is important to note overall porosity volume percentage of a material (generally >99% density is desired) to get an understanding of the overall quality of a part, defects above the critical size are often more detrimental to fatigue life and more important to identify for those

concerns. This importance of identification is especially true for parts operating in the low cycle fatigue regime where high stress amplitudes can induce relatively large stress concentrations around pores.

Table 1: Critical defect sizes for various metals and manufacturing techniques

Manufacturing Method	**Material**	**R** $[\frac{Minimum\ Stress}{Maximum\ Stress}]$	**Stress Amplitude [MPa]**	**Defect Size [µm]**	**Reference**
Cast	Aluminum Alloy	-1	100	~120	[26]
Cast	Ni-based Superalloy PWA 1483	-1	450	~15	[37]
Weld	Weld Metal SM4I	0	225	~50	[38]
Powder Metallurgy	Steel	-1	300	~45	[29]
Forged	Steel	-1	~300	80	[39]
SLM	Ti64	0.1	450	~11	[40]

Furthermore, the presence of porosity is an issue with respect to the fabrication process of AM metals because of the resulting implications on the structural integrity of final part applications, often leading to reduced performance [41][42]. According to Xia et al., porosity is a "major processing-induced phenomena" in AM and was characterized in almost all of their SLM-produced components, with the SLM processing conditions being chiefly responsible for the tendency of pores to form during a build [43]. The relevant literature for porosity, as it relates to AM produced parts, will be presented and discussed in order to define the state of the art of characterization of these defects. Furthermore, the experimental methods and workflow employed throughout this research utilize and build upon existing literature on the subject matter.

2.1.1 Porosity Effects on AM Parts

Primarily, high material porosity results in the reduction of static, dynamic, and fatigue strength of parts, as shown in SLM produced AlSi10Mg specimens by Brandl et al. [41]. Pollock et al. confirmed the negative effects that porosity has on material strength but also on the failure behavior of a part, in Ni-based super alloys [44]. Brandl et al. explain that the reduction of cross-sectional area, due to high levels of porosity, can cause reduced static strength and the presence of the pores themselves can cause stress concentrations, resulting in reduced dynamic strength. Furthermore, the work of Tillman et al. discussed that the stress concentrations that form around pores can lead to premature crack initiation under cyclic loading, resulting in the reduced fatigue strength of an AM part [42].

Circular discontinuities, such as an idealized pore, act as stress concentrators in a continuum field, as first proposed by Kirsch [45]. These stress concentrators are important because they enact a localized increase in stress in the neighboring material. Kirsch defined Equation 1, Equation 2, and Equation 3 for the stress state around a hole in a linear elastic plate under uniaxial loading, as shown in Figure 3. Following, the stress concentration factor, K_t, is the ratio of maximum stress at the hole to the remote stress. Stress concentrations are influencing factors in the fracture mechanics governing fatigue life of materials because the localized increase in stress can lead to increased localized strain and strain energy, one of the governing factors for both crack initiation and crack growth in ductile materials such as metal.

$$\sigma_{rr} = \frac{\sigma_\infty}{2}\left(1 - \left(\frac{a}{r}\right)^2\right) + \frac{\sigma_\infty}{2}\left(1 - 4\left(\frac{a}{r}\right)^2 + 3\left(\frac{a}{r}\right)^4\right)\cos 2\theta$$

Equation 1: Radial stress state around a hole in a plate in uniaxial tension [45]

$$\sigma_{\theta\theta} = \frac{\sigma_\infty}{2}\left(1 - \left(\frac{a}{r}\right)^2\right) + \frac{\sigma_\infty}{2}\left(1 + 3\left(\frac{a}{r}\right)^4\right)\cos 2\theta$$

Equation 2: Hoop stress state around a hole in a plate in uniaxial tension [45]

$$\tau_{r\theta} = -\frac{\sigma_\infty}{2}\left(1 + 2\left(\frac{a}{r}\right)^2 - 3\left(\frac{a}{r}\right)^4\right)\sin 2\theta$$

Equation 3: Shear stress state around a hole in a plate in uniaxial tension [45]

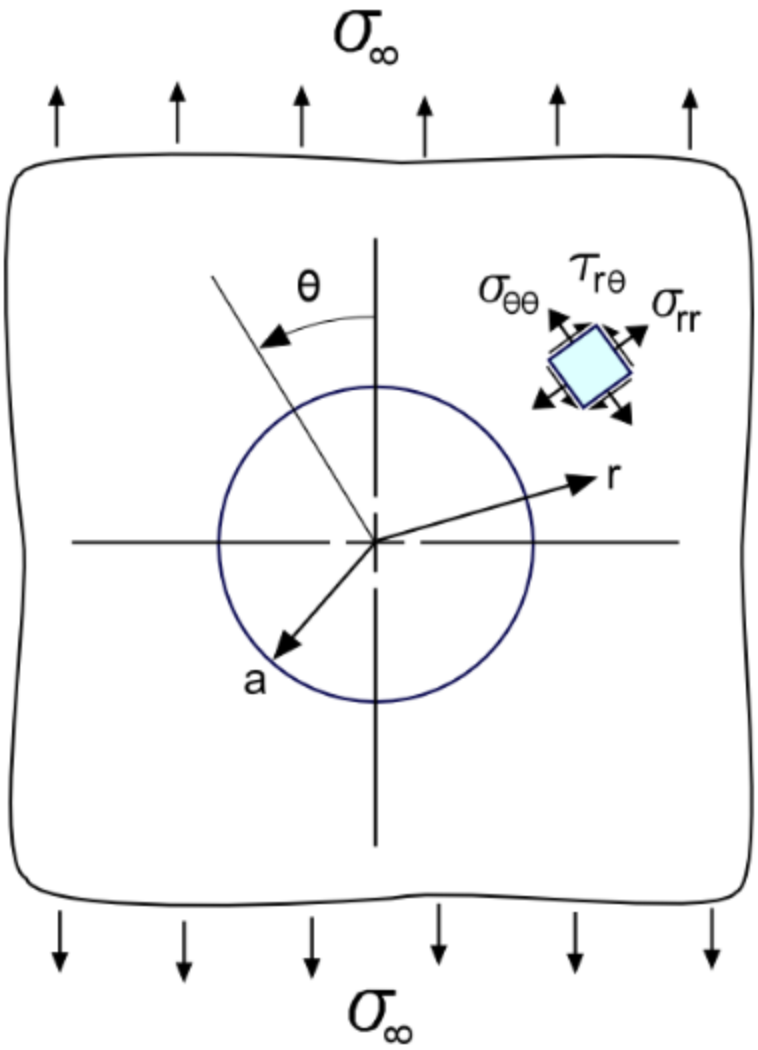

Figure 3: Schematic of stress states around a hole in a plate under uniaxial loading [46]

In addition to the work provided by Kirsch, Danninger and Weis reported that clusters of pores in a matrix can be a greater detriment to the mechanical performance of the material than any one of the pores themselves [29]. Investigating fractographs of cast specimens that had undergone fatigue loading, Danninger and Weis observed that cracks were initiating from defects previously thought to be subcritical, as theorized in a Kitagawa diagram for the material used [29]. However, when observed further, firstly it was noted that each crack-initiating singular defect was coupled with a smooth circular area about double the size of the defect itself and was concluded that the effective defect size is given

by the dimensions of the stress field surrounding the individual crack-initiating defect [29]. Secondly, the researchers observed that in every specimen, the crack initiation site actually consisted of a group of two neighboring secondary pores, with the radius of the stress field surrounding the cluster of defects amounting to about twice the geometrical radius of the clusters themselves [29]. Using this effective radius of the stress field of two neighboring pores, the effective defect size aligned with what was theorized from the Kitagawa diagram [29]. This small pore cluster phenomenon reported by Danninger and Weis is important because it shows that smaller defects that are theoretically determined to be subcritical could in fact be supercritical and cause fatigue failure, putting the onus on inspectors to potentially seek out observation of small defects that were previously ignored.

2.1.2 Porosity Effects on Fatigue Performance

The research conducted in this thesis covers the characterization of porosity in AM Ti64 and IN718 built by the SLM process. With respect to the materials of interest in this research, the fatigue performance of AM parts has been specifically explored in existing literature and key trends have been noted to help form a general top-level framework for research aims.

Several researchers have studied the fatigue characteristics of AM IN718 parts and related performance back to the presence, or lack thereof, of porosity. Gribbin, et al. investigated the strength and low cycle fatigue life of SLM IN718 with results showing that the importance of porosity is not as significant at low strain amplitudes as it is at high strain amplitudes [47]. Post-processing and specimen build orientation can also play a role in the fatigue life of AM parts. Scott-Emuakpor et al. have shown variability in fatigue performance between different vendors providing SLM IN718 specimens for testing,

possibly being caused by the differences in post-processing of the parts, including Hot Isostatic Pressing (HIP) and stress relief, that was used to remove defects like porosity that contribute to fatigue life [48]. However, it was noted that fatigue performance of SLM IN718 could match or even exceed that of cold-rolled IN718 with the right post-processing. Tillman et al. noted that most of the pores in their samples seemed to be found in the boundary region (between contour and hatching) of the scan strategy utilized [42]. Kelley et al. observed that the fatigue strength of SLM IN718 specimens built in a horizontal orientation was greater than that of specimens built in a vertical orientation, using an island scan strategy [49]. Furthermore, it was shown that machined specimens had at least a 7 times improvement over as-built specimens with respect to fatigue life [49].

Similar characteristics have been noted by researchers observing the performance of AM Ti64 parts. Scott-Emuakpor et al. show variability in fatigue properties in SLM Ti64 specimens, possibly due to variations in microstructure and defects [50]. Leuders et al. investigated fatigue resistance and crack growth in SLM Ti64 and showed that there is a direct link between the location of porosity near the specimens' surfaces and fatigue life [20]. Leuders' findings are in agreement with those of Eylon for cast Ti64, who stated that all pore-related fatigue failures observed in their test specimens initiated from a defect located close to the specimen surface [51]. Furthermore, Leuders' results are confirmed by the work of Wycisk et al., where all of their as-built SLM Ti64 specimens failed from near-surface defects [40]. SEM images in Figure 4a and Figure 4c showed the failure crack of one of Leuders' specimens initiating from a likely pore close to the surface and the corresponding fatigue life was much lower than that of a specimen whose failure crack initiated from a pore further form the surface (Figure 4b,d) [20].

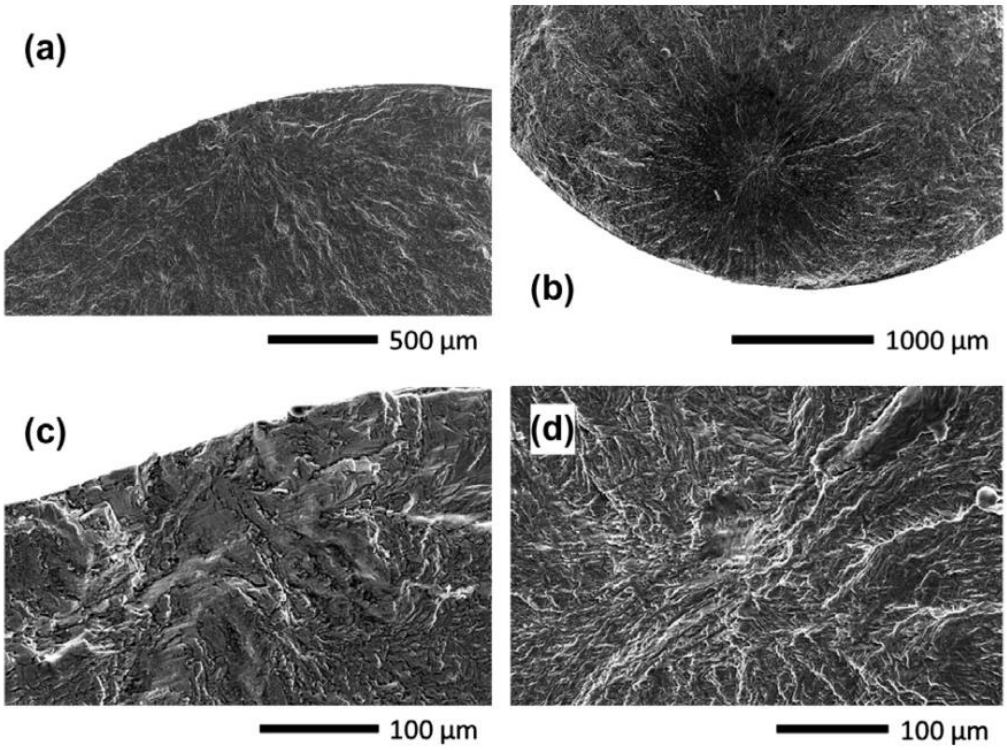

Figure 4: Crack surfaces of hot isostatic pressed SLM Ti64, post fatigue failure for a) and b) low magnification and c) and d) higher magnification [20]

The works discussed for AM IN718 and Ti64 either directly state or imply that surface porosity has a greater impact on the reduction of fatigue life as opposed to porosity occurring within the bulk of the material. For a cast material, the effect of defect location on the stress intensity factor (different from stress concentration factor), ΔK, was obtained and characterized [29]. As applied in Figure 5, sometimes the effective stress intensity threshold, ΔK_{theff}, must be substituted for ΔK_{th} depending on certain conditions [52]. It should be noted that the Kitagawa diagram is only valid for a specific loading criteria (R and number of cycles) and different loadings may produce varying results. As seen, the location of a defect affects the stress intensity threshold (stress intensity limit below which cracks will not grow), ΔK_{th}, resulting in a lower critical defect size for pores located close

to the surface than for those in the bulk of the material. Furthermore, a crack that forms from a pore at the surface will have a lower stress intensity threshold than one that forms from a pore of the same size located in the bulk of the material, leading to a higher crack growth rate for such cases. Eylon provided a possible reason for the larger effect of near-surface porosity on fatigue performance, owing to the fact that many loadings experienced are a mixed mode of axial and bending, inducing max stresses near the surface of the part and creating a higher probability of crack initiation in this region [51].

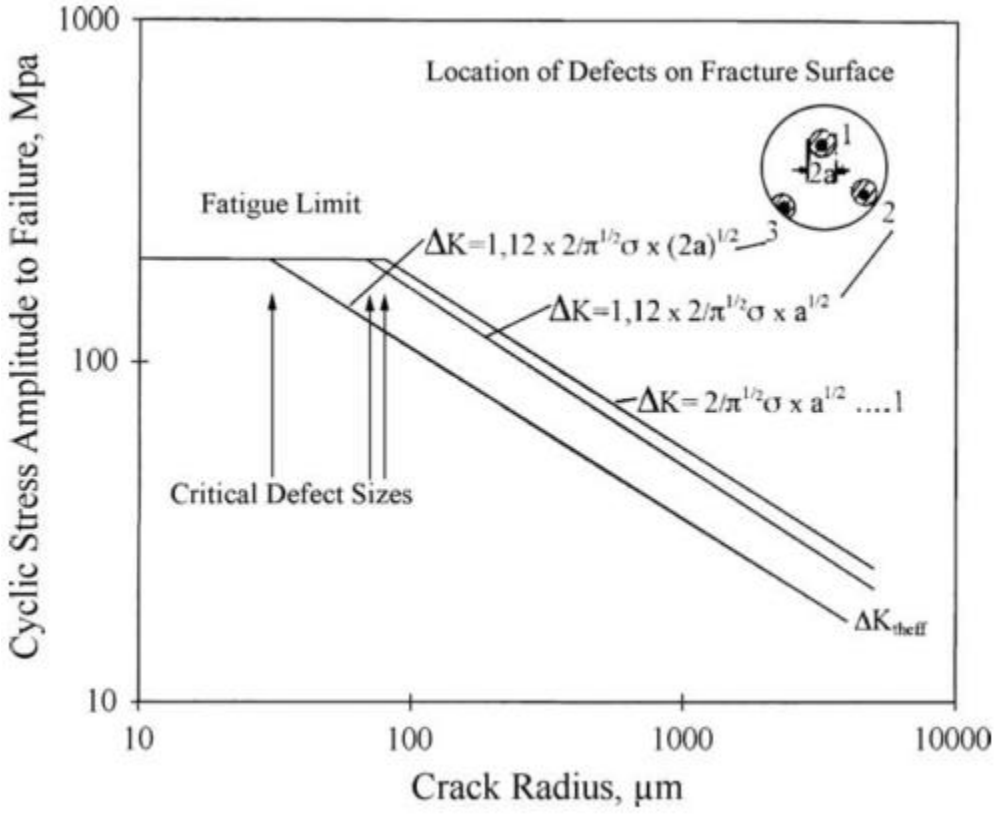

Figure 5: Schematic Kitagawa diagram depicting the effect of defect size and location on fatigue endurance strength [29]

In summary, it is noted that to improve fatigue strength in SLM metals, the phase up to crack initiation and the crack growth phase must be extended [20]. The initiation

phase is controlled mostly by the size, location, and amount of porosity while the latter is dominated by material residual stress [20][53]. Li et al. surveyed different fatigue research conducted on AM Ti64 and compared it with research conducted on wrought Ti64. It was noted that superior AM fatigue performance to wrought and annealed Ti64 is possible and different post-processing treatments, including the removal of internal defects, are recommended to reach a superior performance [54]. However, Li et al. made no such claim that post-processing treatments are entirely necessary to reach superior performance. Due to the lack of available quantitative research linking processing conditions to microstructure and defects, and eventually fatigue performance, Li et al. concluded that there is still great potential for optimization of AM parameters that lead to sufficient structural parts without post-processing [54].

The aim of this research project is to show that post-processing and utilization of optimal build orientations and parameters can reduce porosity content. This thesis specifically, as stated, will characterize the porosity amongst different post processing steps, build orientations, and at different resolutions. We aim to show that synchrotron-based microscale X-ray computed tomography can be effectively used as a non-destructive inspection tool, with the ability to gain information about small pores undetectable through commercially available computed tomography techniques. Furthermore, a discussion will be provided on the possible causes of the observed defects as well as possible mitigation strategies.

2.1.3 Prevalence of Porosity in AM Metals

Porosity rates and distributions are different, depending on material and pre-fabrication, fabrication, and post-fabrication processing. Further literature has been

surveyed to determine porosity rates relating to the materials of interest in this research, IN718 and Ti64. A survey of available literature was conducted, and showed porosity volume percentages ranging from 0.02% to 2% in SLM built IN718 parts [55][56][57][58][59][60][61][62][63][42]. Similarly, available literature on porosity content in SLM Ti64 parts was studied and porosity volume percentages were observed ranging from 0.000226% to 2.36% [64][53][20][22][65][66][67][23][68][69][70].

2.2 Causes of Porosity

Porosity observed in SLM parts can be differentiated by morphology, which is a result of what phenomenon produced the pore of interest. There are four main types of porosity that have been observed consistently in SLM parts: 1) trapped gas, 2) keyhole, 3) balling and 4) lack of fusion.

2.2.1 Trapped Gas

Trapped gas porosity is prevalent in SLM produced parts because the fabrication takes place in an inert gas and not in a vacuum, as some other AM methods. In trapped gas porosity, the pores are spherical in shape and are mostly the result of gas that was introduced during the powder processing step and was unable to escape during the SLM processing step [56][64][65][71][72][73][74][75]. A depiction of trapped gas porosity in the material powder, pre-build, is shown by Cunningham et al. in Figure 6, who suggested that pores larger than 15 μm in the powder do not transfer to the as-built parts [64].

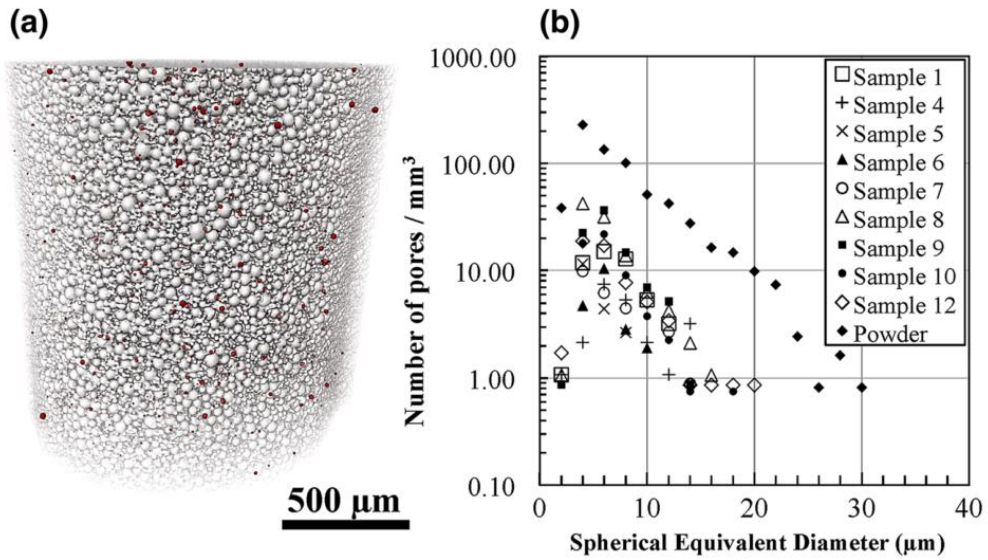

Figure 6: a) Projection of a reconstruction of Ti64 powder containing trapped porosity within the particles (shown in red) and b) volume averaged size distribution of spherical pores detected in the powder vs. samples identified as having gas pores [64]

2.2.2 Keyhole

The keyhole phenomenon, depicted in Figure 7, is a result of high energy density welding. The SLM process is akin to a laser that micro-welds metal powder to form a layer of a part; and the process is repeated until completion of a final structure. As such, SLM is affected by the keyhole phenomenon, observed previously in weldments, which is a result of the laser vaporizing the metal due to a high energy density [76][7][77]. This vaporization creates expanding gas that pushes outward and a high aspect ratio "keyhole" is able to form from the surface downward [78]. As long as the laser energy density is maintained, either through high power or slow scan speeds, the keyhole will remain open [78]. However, if the energy density dips below a certain level, the keyhole will begin to collapse on itself, trapping in pockets of metal vapor and creating spherically or irregularly shaped pores as the molten metal solidifies around it [64][79][77][7][78][76].

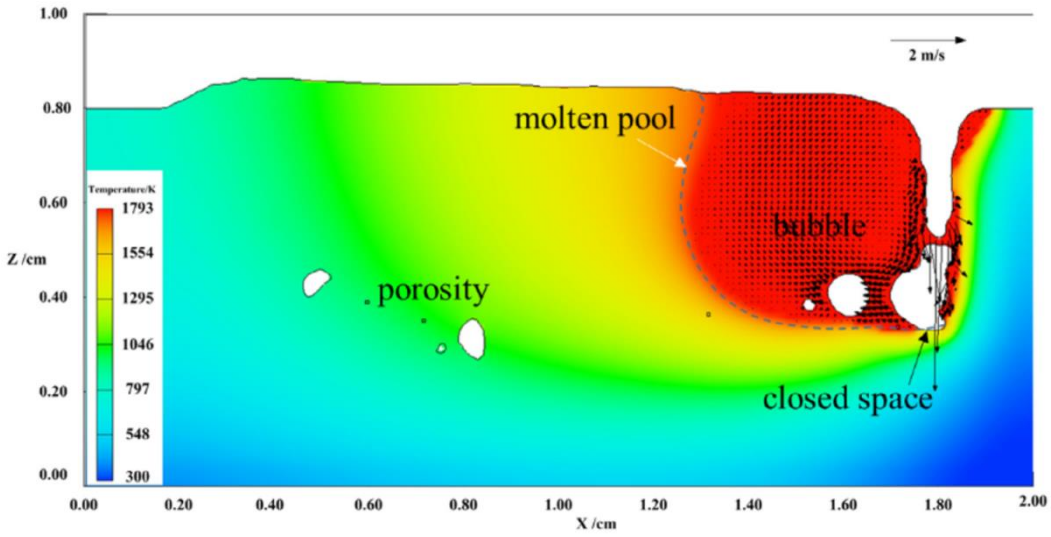

Figure 7: Simulation of keyhole porosity in two dimensions [79]

2.2.3 Balling

Balling is a phenomenon that occurs due to vaporization of the metal powder [80][19]. When vaporization occurs, the recoil pressure from the vapor can eject molten material that is then transferred to the surface of the melt track [80]. Rapid solidification of the ejected molten material can form a spherical particle that may be larger in diameter than the layer size of the build [80]. Once the recoating blade moves across the build surface to spread the next layer of powder, it can scrape off the solidified particle and leave a pit, shown in Figure 8a [80]. If this pit is not filled in subsequent layer formation, due to insufficient melt pool overlap or other means, it will form a pore underneath the new layer [80]. Porosity due to balling is usually spherical in morphology [80].

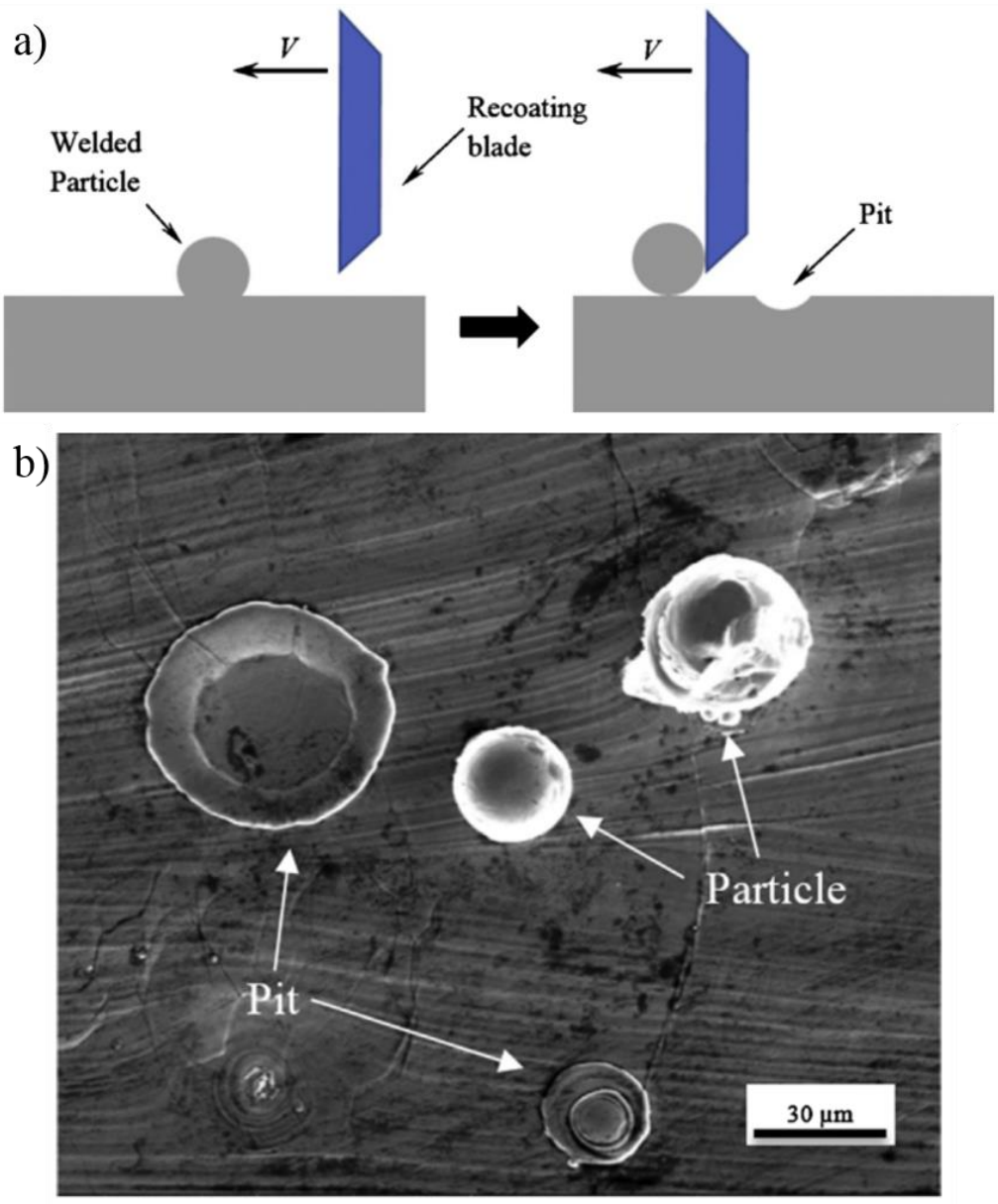

Figure 8: a) Schematic of a balling defect caused by recoating during the SLM process and b) SEM of balling pits and welded particles on top of an SLM sample [80]

2.2.4 Lack of Fusion

Porosity due to lack of fusion is consistently observed, owing to non-optimal SLM processing parameters, and is usually asymmetrical in morphology. Lack of fusion porosity is generated when the energy density is not high enough to fully melt the powder,

but only great enough to sinter the un-melted cores of particles together through necking, visualized in Figure 9 [81]. Thus, lack of fusion porosity is highly dependent on SLM processing parameters, including laser power, scan spacing, and scan speed [56][64][65][23].

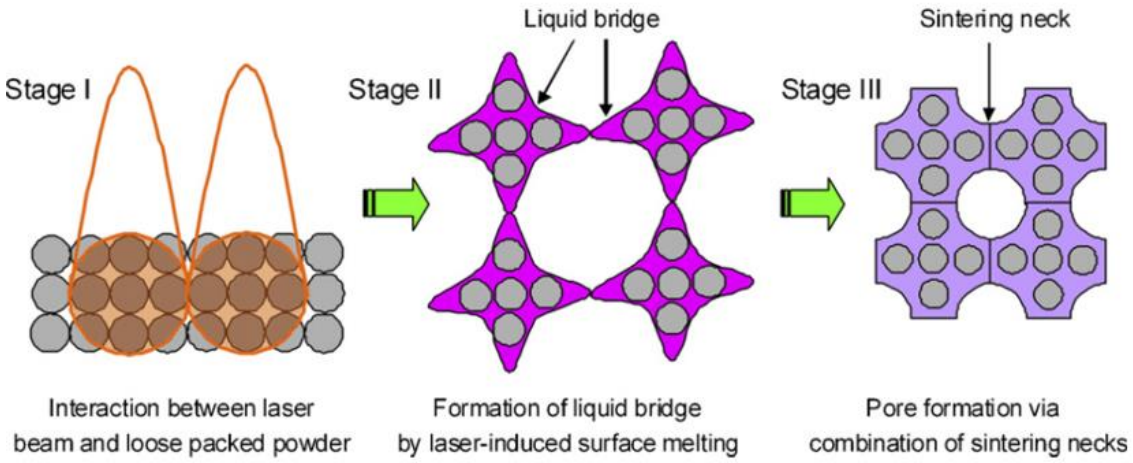

Figure 9: Schematic of lack of fusion pore development during SLM [81]

2.2.5 Contouring and Hatching

The powder bed SLM AM process has developed over time to utilize a contouring and hatching laser scan strategy to build up parts. Contouring is when the laser traces the outline of the cross-sectional layer area and hatching is when the laser scans the inner portion of the layer area. Contouring can either happen before, after, or both before and after the hatching process. According to Qiu et al., the contouring scan strategy is aimed at improving part surface finish [23]. The contouring and hatching scan strategy can be viewed as a tradeoff between manufacturing efficiency and part quality, as it has been shown that certain hatching strategies may increase the amount of defects in AM parts [82].

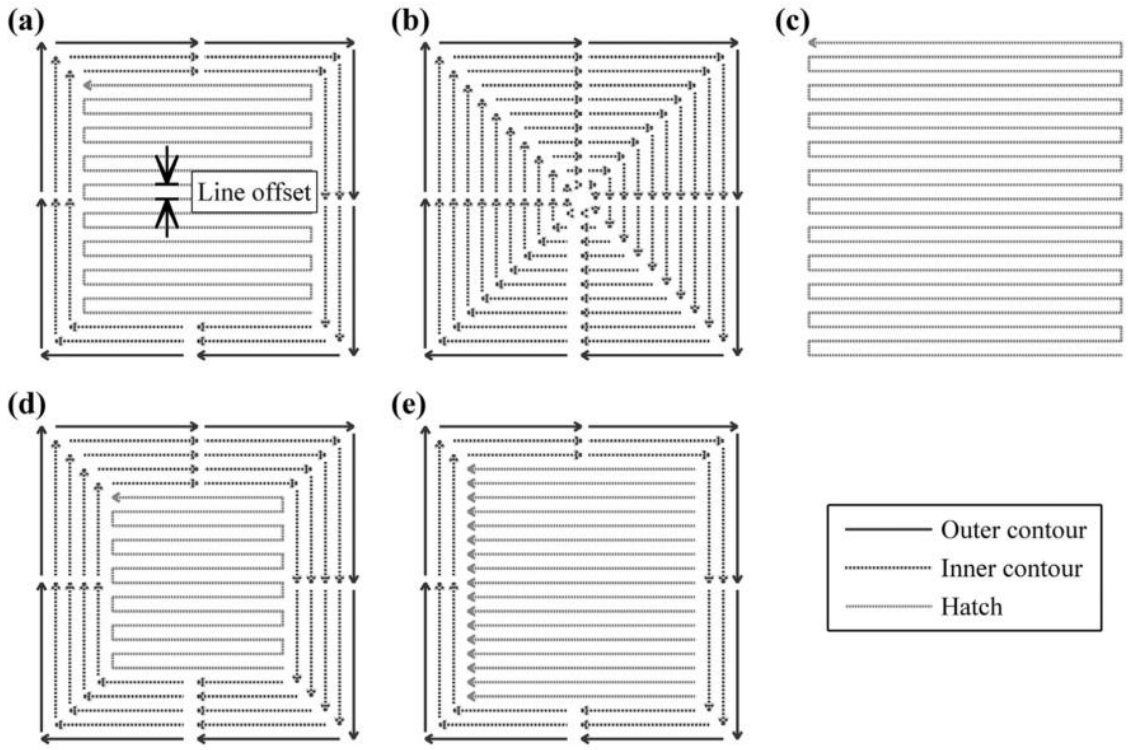

Figure 10: Schematic diagrams of different scan strategies including some employed for experimental purposes, including a) default Arcam EBM, b) contour only, c) hatch only, d) number of contour passes set to 5, giving a smaller hatched region, and e) single direction hatching [82]

Tammas-Williams et al. studied the effects of scan strategy, displayed in Figure 10, on electron beam melted parts and found that porosity can be increased or decreased by altering the amount and/or presence of contouring and hatching [82]. Furthermore, it was shown that the location of porosity was not randomly distributed in the cross-section of the build but instead more probable in the areas where the hatch met the contour, and on the inside of where the laser enacts a 180-degree turn [82][83]. Tammas-Williams et al. gave several possible reasons for how the hatching strategy could be creating porosity. One possible reason for the correlation between hatching and porosity is that the laser scan may be moving gas porosity from inner regions of the cross-sectional area, as a gas bubble is

pushed by the traveling melt pool and deposited when the laser enacts its turn [82]. While this could cause some of the observed porosity, according to Tammas-Williams et al., porosity in this region could also be a result of keyholing or lack of fusion, phenomenon that are both functions of the laser energy density in the material [82].

2.2.6 Energy Density

Thus, it is more likely that the porosity in a specific region is caused by effects of the energy density, as reported by several authors [82][57][84][85][86]. Energy density, E, is defined as the energy delivered by the laser beam per volumetric unit of powder and given by the equation

$$E = \frac{P}{vht}$$

Equation 4: Laser energy density [84]

where P is the laser power, *v* is the laser scanning speed, *h* is the hatching distance, and *t* is the layer thickness [84][87][88]. In general, a low energy density can result in incomplete melting of the metal powder, leading to lack of fusion porosity [81]. One factor that can lower the energy density of a volume is when the hatch spacing is too far apart to create overlap of neighboring melt tracks, shown in Figure 11 [80].

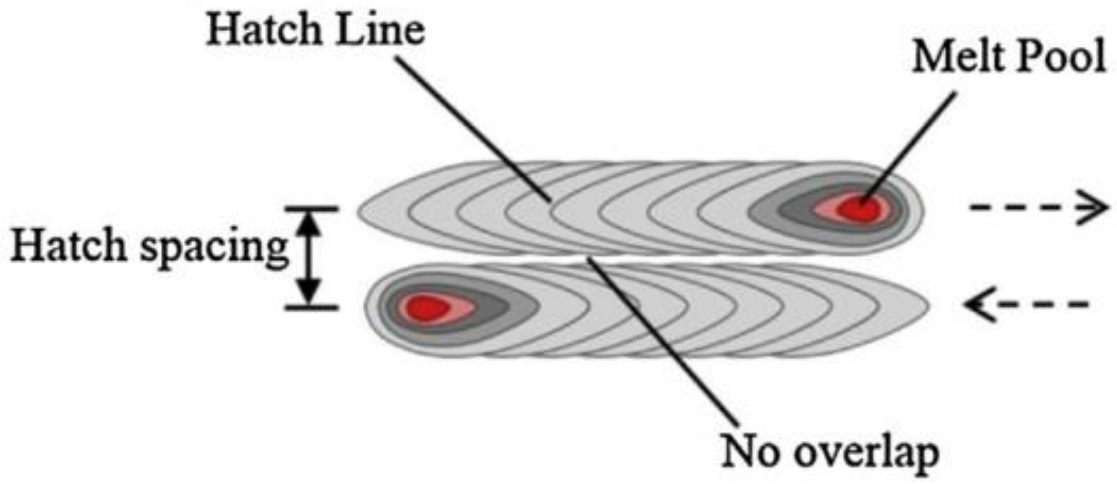

Figure 11: Schematic of SLM melt tracks without overlap [80]

In contrast, a high energy density can cause vaporization, leading to keyhole and balling porosity as well as a poor surface finish [79][80]. As seen in Equation 4, the energy density is controlled by three factors in the scan strategy: laser power, scanning speed, and hatching distance. Gong et al. showed how controlling laser power and scan speed could have significant effects on porosity formation, displayed in Figure 12, with porosity distribution changing as a function of both scan speed and laser power. In the three graphs of Figure 12, Zone OH represents parameters that will not result in successfully built parts due to thermal deformations, Zone I represents parameters that result in nominally fully dense specimens, Zone II are parameters that result in over melting, and Zone III parameters leave incomplete [86]. Due to the different causes of SLM porosity from both high and low energy density, porosity may form in other Zones OH through Zone III.

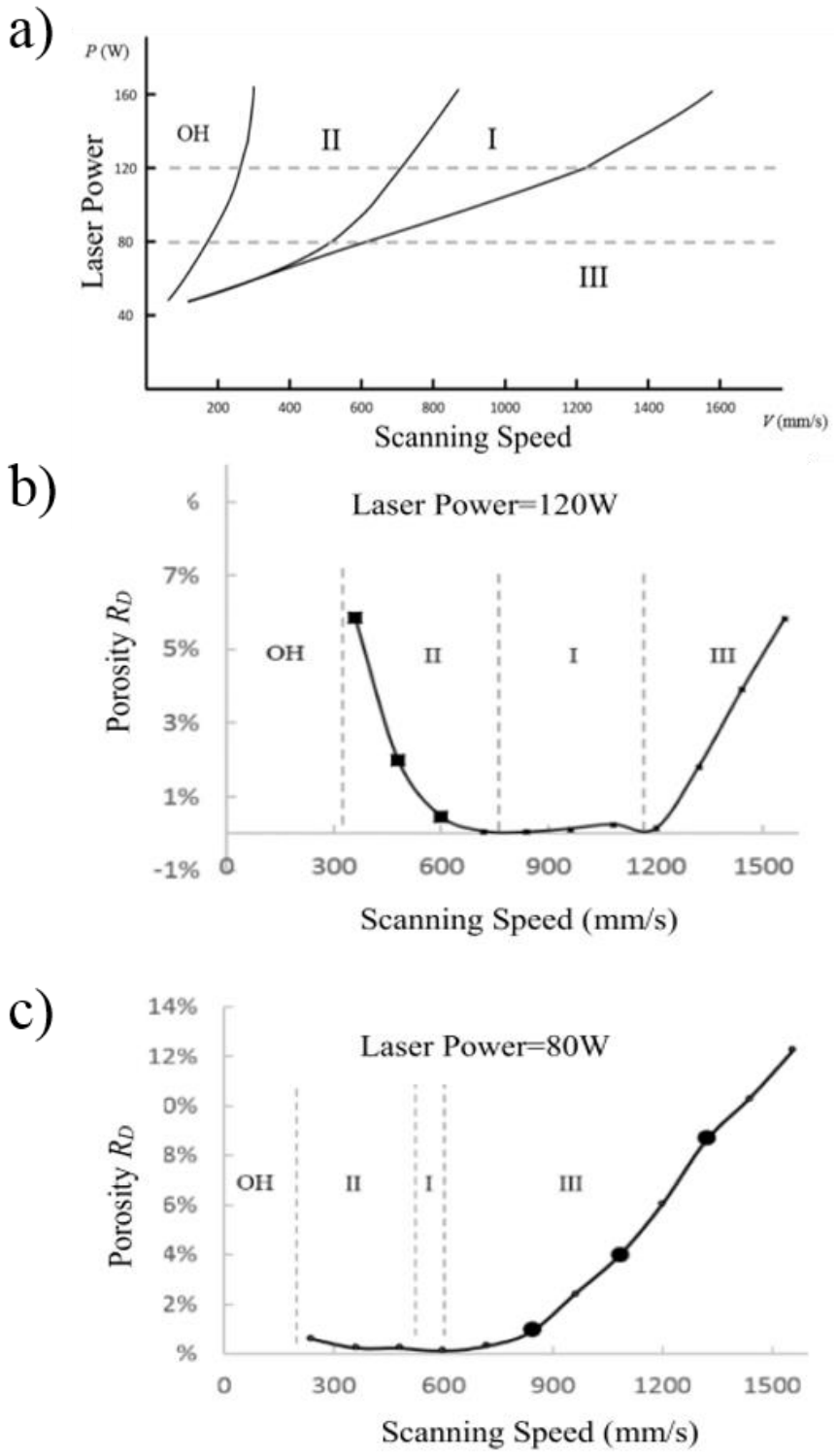

Figure 12: a) Process window of SLM and porosity distribution at b) 120W, and c) 80W [86]

The effects of the laser energy density on defect formation is important to keep in mind when employing a certain scan strategy. When a turn is enacted as a hatch meets the contour, scan strategies often will decrease laser power and/or increase scan speed to keep the energy density in the turn area consistent with the rest of the scan area. Finding the optimal energy density for this region has proven difficult, as the formation of porosity is also influenced by the presence of two melt pools close to each other at the turn [85]. Zhou et al. traced porosity formation to the dynamics of the melt pool, including the thermocapillary surface tension, gas flow shear stress, and surface roughness between scan lines, and traced these characteristics to the parameters that can control such dynamics [85]. From the relationship shown in Figure 13, it is clear that there are different tradeoffs to consider when choosing processing parameters that can affect the final part quality. When coupled with the need to maintain a desired manufacturing efficiency, it is evident that the tradeoffs in the processing parameters of SLM parts are a complex optimization that require further characterization of final part quality and relation to build parameters. Unfortunately, for the purposes of this research, porosity was not able to be related to exact processing parameters due to them being kept proprietary to the manufacturer of the specimens, EOS. However, the observation of porosity in this thesis can potentially serve as a "smoking gun" for the influence of scan strategy on part quality and add to the available data on defect characterization.

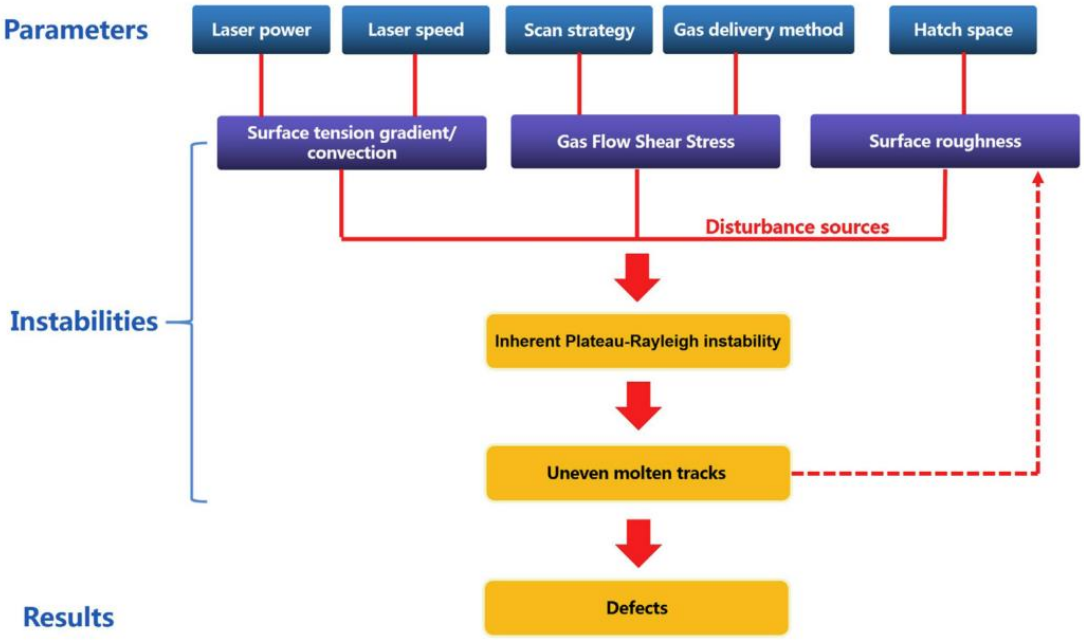

Figure 13: Diagram of the relationship between defect formation mechanisms and fabrication parameters [85]

2.3 AM Part Post-Processing Techniques

Optimizing AM SLM processing parameters to reduce porosity content has the potential to be the most efficient means of defect mitigation; however, much of the work in the space thus far has been focused on exploring the effectiveness of post-processing techniques. Two post-processing steps were surveyed in the current research to gain an understanding of their effect on part defects: hot isostatic pressing (HIP) and heat treatment (HT). HIP is a densification process that utilizes heat and pressure to apply compressive forces to a part in order to close pores. HT can span many different individual processes and is aimed at relieving residual stress and/or changing the part microstructure.

2.3.1 Hot Isostatic Pressing

HIP has been explored in IN718 and Ti64 in terms of the ability to densify parts. Rao et al. showed that IN718 powder that had undergone a HIP process could reach its theoretical density [89]. Work by multiple researchers have shown that a proper HIP treatment can create near fully dense SLM Ti64 parts [20][66]. An example of a computed tomography visualization of SLM Ti64 pre, and post HIP is displayed in Figure 14. Similarly, Tillman et al. investigated the effects of HIP on SLM IN718 and observed that the majority of pores could be densified by HIP, depicted in Figure 15 [42]. However, Tillman et al. also observed that some porosity was unable to be densified by the HIP process, with this phenomenon likely being caused by the presence of entrapped gas from the SLM or powder feedstock processing [42]. In fact, HIP can sometimes worsen overall part quality. The introduction of internal stresses can lead to elastic or plastic deformations caused by the expansion of trapped gas as it is subjected to the high temperatures of the HIP process (gas laws) [42]. In any case, HIP has commonly been used in the post-processing of SLM parts to decrease porosity content because of its ability to generally improve tensile properties, fatigue resistance, and ductility [66][48].

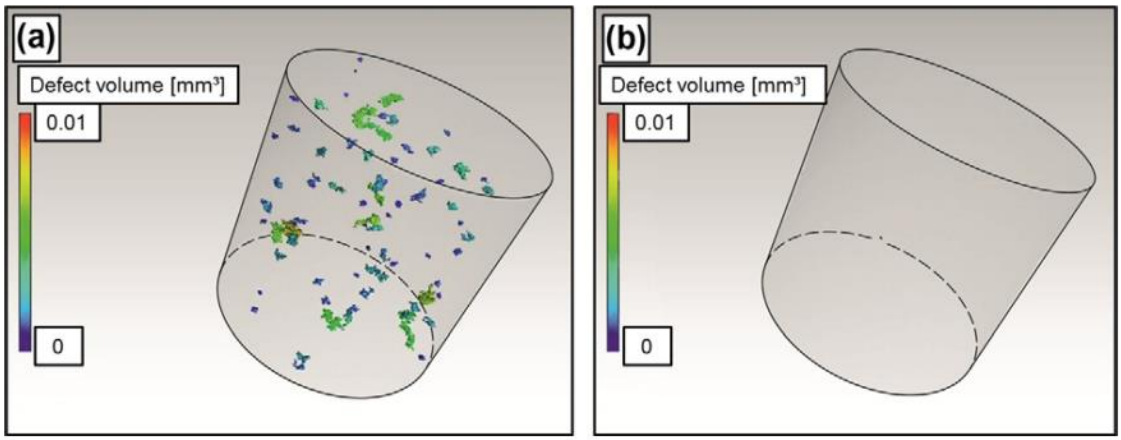

Figure 14: 22 µm-resolution computed tomography images of a) as-built SLM Ti64 specimens, and b) after HIP processing [20]

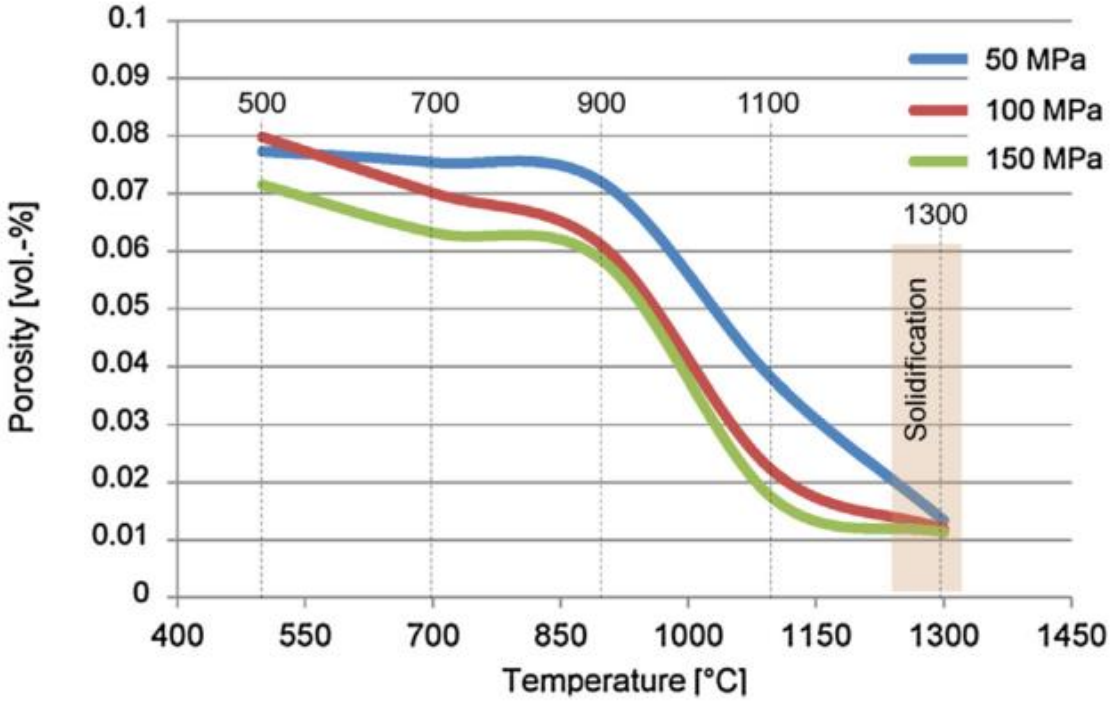

Figure 15: Porosity measured after HIP processing of SLM IN718 with different temperatures and pressures [42]

2.3.2 Heat Treatment

HT has been performed on AM parts with an interest in exploring the effects on the final part material characteristics. Proper HT has been shown to relieve residual stress that is a byproduct of many AM fabrication techniques, including SLM [19][90][91][92]. Furthermore, Zhang et al. utilized HT on as-built SLM IN718 and observed an increase in strength and hardness that was comparable to wrought IN718 [18]. Zhang also noted that the HT specimens exhibited a decrease in ductility compared to their as-built state [18]. Maskery et al. explored the potential effects of HT on the porosity of SLM Al-Si10-Mg as compared with its as-built state and reported that overall density, pore size, and shape distributions were not significantly altered by HT [93]. Leuders et al. conducted a study of the effect of HT on SLM Ti64 and also observed no significant change in pore population [20].

2.4 Porosity Characterization Techniques

In previous work characterizing porosity in metals, three techniques have generally been utilized: 1) Archimedes' Method, 2) Microscopy, and 3) X-ray Computed Tomography.

2.4.1 Archimedes' Method

The Archimedes' Method is a fairly straightforward and simple process to obtain the density of a part. The Method is based on the ancient mathematician Archimedes' Principle of the physical law of buoyancy. The Method involves comparing the mass of a part to the mass of the volume of liquid it dispels when completely submerged, and is also termed pyknometry [94]. The equation for porosity percentage, P, of the part is then given by

$$P = 100\left(1 - \frac{\rho_L}{\rho_{th}} \frac{W_S}{W_S - (W_{sb} - W_b)}\right)$$

Equation 5: Porosity volume percentage via Archimedes' Method [94]

where ρ_L is the density of the liquid, ρ_{th} is the theoretical value of the porosity-free density of the alloy, W_s is the dry-weight sample measurement, W_{sb} is the buoyant-weight sample plus basket measurement, and W_b is the buoyant-weight basket measurement [94]. Several researchers have effectively utilized Archimedes' Method to characterize the porosity content of samples in SLM materials as a limited, but low error method [89][7][72]. The Archimedes' Method, while reliable and accurate based upon the calibration and precision of the scale utilized, can only give information about porosity volume percentage and no other features, and thus, is not suitable for more in depth porosity studies.

2.4.2 Microscopy

Microscopy is a technique that is more complex than Archimedes' Method and can be used to find out more information about the porosity of a part, including volume fraction, distribution, and morphology [23]. Microscopy is performed by choosing a surface of a specimen to explore (either a natural free surface or by slicing the part to create a surface), polishing the surface, and then examining the surface under a microscope, as shown in Figure 16. The observed surface can then be characterized qualitatively by eye or quantitatively utilizing image processing software to calculate distribution, morphological, and area fraction data. To relate the calculated area fraction of porosity on the observed cross-section to volume fraction porosity of the part, a statistical analysis is performed with a specified confidence interval on the data acquired. The microscopy method has been

employed for porosity characterization in numerous papers exploring porosity in AM parts [95][89][50][42][61][23][96]. The downside to investigating porosity via microscopy, is that the accuracy of general conclusions about the subject is statistically dependent on the number of different free surfaces sampled throughout the volume of the part. Because of this, microscopy can sometimes under predict or over predict the quantity and volume of porosity within a specimen, compared to other inspection methods [42]. Furthermore, microscopy is mostly a destructive testing mechanism, with sample preparation and slicing needed to investigate portions of the sample. Lastly, accurate morphology is unable to be quantified through microscopy because it requires information about the third dimension of the pore, which is not obtained in most microscopy studies [97].

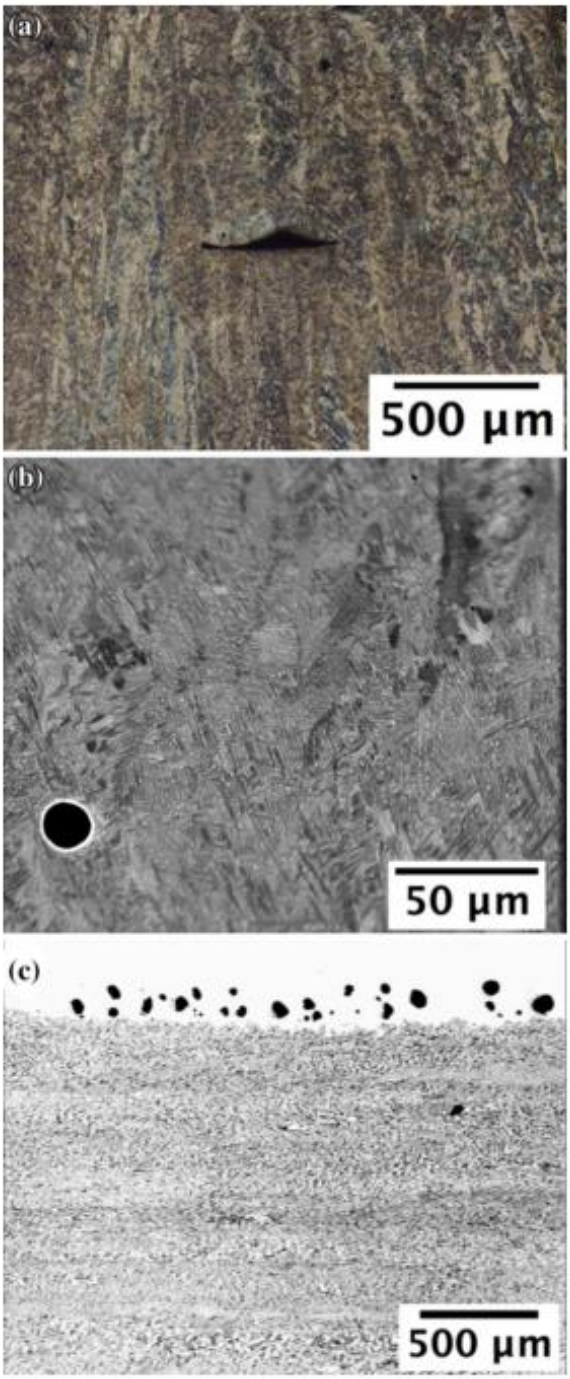

Figure 16: Varying porosity morphologies observed via microscopy including those of an EBM Ti64 a) irregularly shaped lack of fusion porosity, b) backscattered SEM image of spherical porosity, and c) keyhole porosity in melt pool of SLM Ti64 [96]

2.4.3 X-ray Computed Tomography

More recently, researchers have employed CT to be able to increase the scope of characterization of porosity across the entire volume of a 3D part [98][99][100][54][101][93][42][62][53][82][53][64]. CT is a non-destructive inspection method that uses X-ray absorption to generate 2D radiographs across the entire length of a part [96]. These radiographs are then reconstructed into a 3D model of the specimen that can be analyzed via image processing and visualization software to determine pore size, morphology, spatial distribution, and porosity content more definitively than either the Archimedes or Microscopy techniques [96]. The Archimedes and microscopy methods are unable to deliver enough data to sufficiently characterize the aforementioned pore qualities due to constraints on those techniques [96]. In comparison, the ability to analyze the entire 3D volume leaves less doubt in resulting characterizations about the porosity content. Additionally, CT allows for a 3D visualization of the specimen and porosity, giving the researcher more observation freedom. Furthermore, Maskery et al. noted that CT has implications in the validation and process monitoring of SLM parts due to the ability to analyze porosity as a function of build height (z-axis) and relate a defect to the specific time of occurrence in the manufacturing process [93]. These abilities make CT an advantageous method of defect observation and porosity-processing correlation, with implications for industrial quality assurance programs. As CT is the focal point of the analysis of porosity for this research, a more detailed explanation of the entire process will be explained in the research methodology section.

Because no feature smaller than one pixel in length can be distinguished from the rest of a specific scan slice (2D radiograph), the accuracy of porosity characterization

utilizing the CT method is highly dependent on the resolution of the 2D radiographs that are able to be acquired [102]. In recent years, only a few researchers have obtained resolutions smaller than 10 μm for exploring porosity in AM parts by CT, with some utilizing a synchrotron beam source for data acquisition on the order of 1μm [82][62][96][64][85]. For IN718, the smallest resolution obtained in CT analysis on SLM parts of the surveyed literature was 5.3 μm [62]. Alternatively, for Ti64, the smallest resolution observed in literature utilizing CT on SLM parts was 0.65 μm [96]. The present work utilizes a synchrotron beam source to obtain radiographs with a resolution of 0.65 μm, for both IN718 and Ti64, which presents the highest resolution CT porosity analysis for SLM IN718 that has been reported to the author's knowledge thus far, and matching the highest resolution for SLM Ti64. Furthermore, on the survey conducted, no research has been reported comparing the porosity observed in a specimen via CT at commercially standard resolutions (30 μm) with as high of a resolution obtained in this work (0.65 μm).

CHAPTER 3. EXPERIMENTATION

3.1 Sample Build and Data Acquisition

3.1.1 Sample Fabrication and Post Processing

All samples utilized for experimentation and characterization were fabricated via the SLM AM technique in both IN718 and Ti64. AM fabrication was completed at Penn State University's (PSU) Center for Innovative Materials Processing through Direct Digital Deposition (CIMP-3D) on an EOSINT M280 machine, shown in Figure 17.

Figure 17: EOSINT M280 high definition additive manufacturing system [103]

The SLM process, commercially referred to as Direct Metal Laser Sintering (DMLS) for EOSINT machines, is a powder bed additive manufacturing process that utilizes a fiber laser to partially melt a layer of powder to form the cross section of a part. This process is

then repeated with subsequent layers of powder until a final part is built up. Exact additive manufacturing settings used for specimen builds in this research are proprietary to EOS and unable to be published at this time.

The DMLS machine consists of several different components needed to create an efficient system. As shown in Figure 18, there is a stationary laser energy source, a mobile scanner to direct the laser, a powder delivery system, powder roller, and powder bed. The system operates by filling up the powder delivery source, heating the build plate (where the component is fabricated) if necessary for the material used, rolling a layer of powder from the delivery source to the bed, deploying the laser via the scanner to melt a cross section of the component, lowering the powder bed by one layer thickness, and repeating the process from the rolling of powder onward until the part is completely built up [11]. Specifically, the part is formed by the laser melting the powder to form a melt pool, which then solidifies to become a formed section of the structure. The size and depth of the melt pool is controlled by and heavily affected by the laser energy density, as previously discussed. Because the powder can act as a support itself, for overhanging features of the build, additional support structures are often not as necessary as in other AM methods [2].

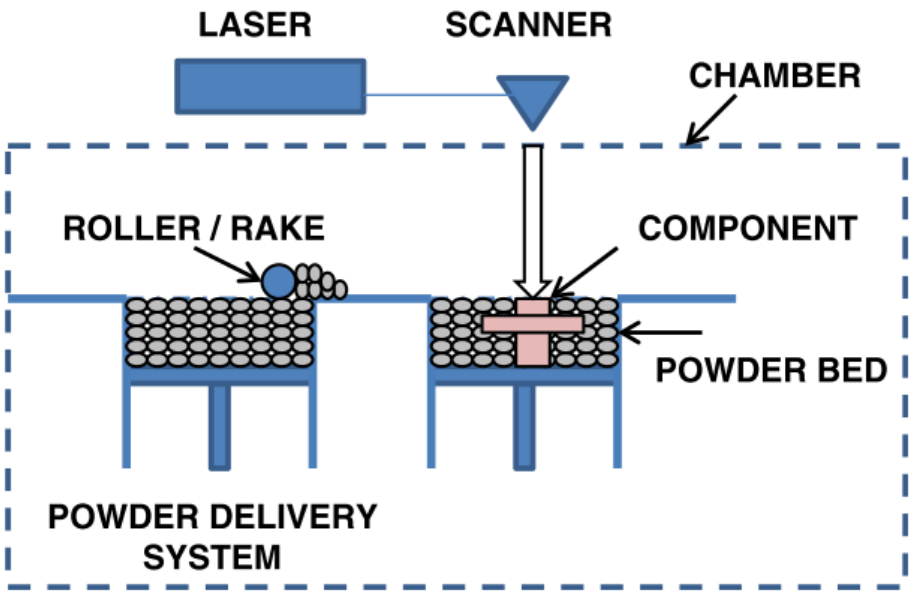

Figure 18: Generic illustration of an AM powder bed system [11]

Experimental test specimens were fabricated in different shapes, build directions, and with different post processing treatments. Some specimens were built in a net dog-bone shape in both the horizontal and vertical direction and are referred to as "as-built". Conversely, other specimens were built in block form in both the horizontal and vertical directions and machined into dog-bone shapes, referred to as "bulk". Figure 19 and Figure 20 display the part dimensions, designed by Todd Book, while Figure 21 shows the IN718 parts still on the build plate in their as-built state [19][103].

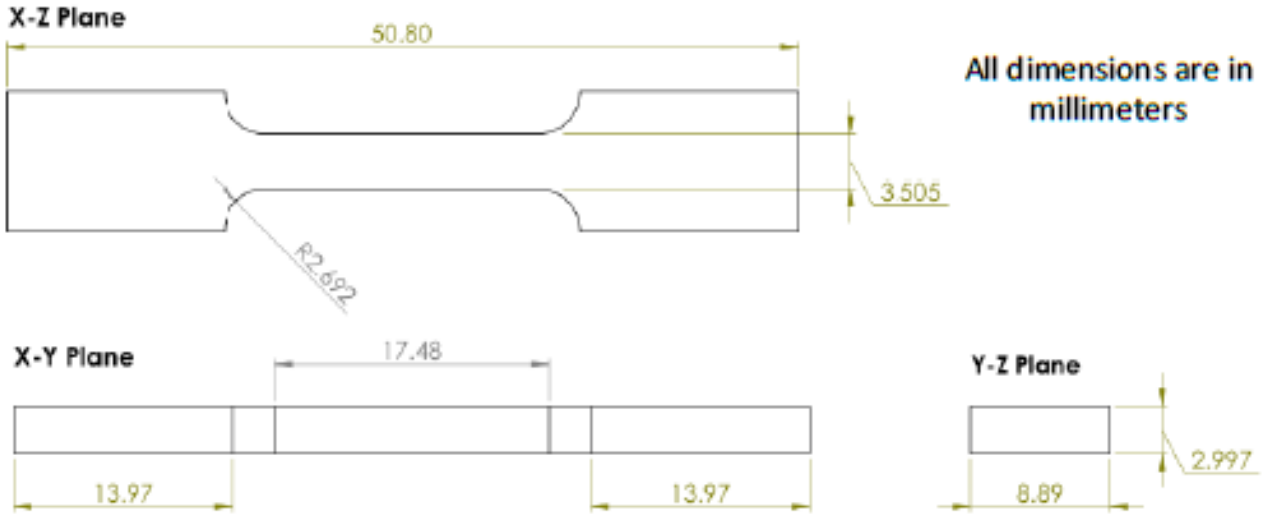

Figure 19: Dog-bone geometry [19]

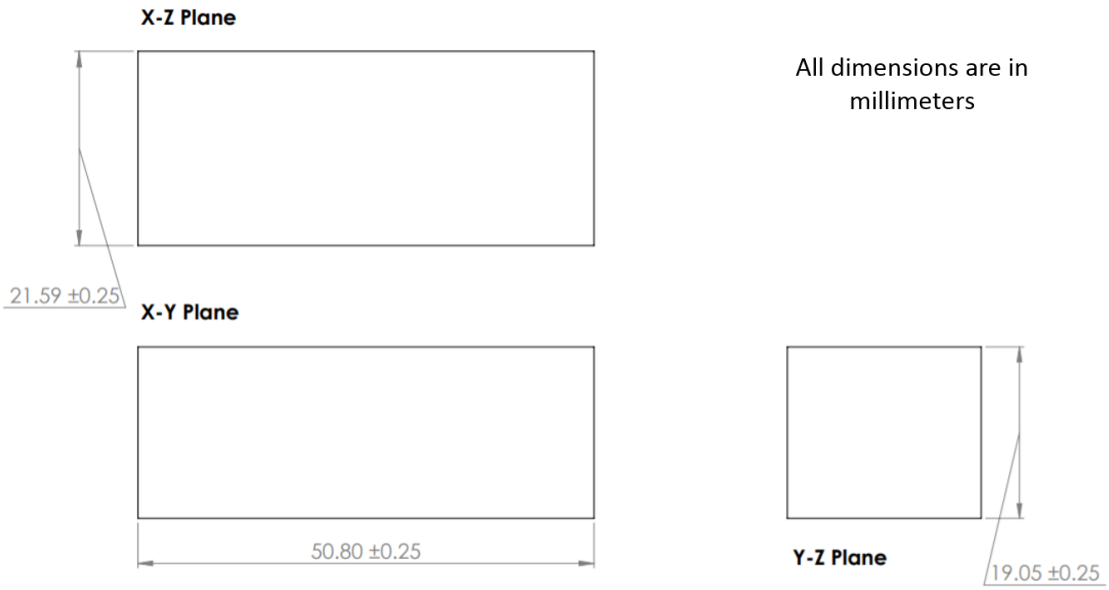

Figure 20: Bulk geometry [19]

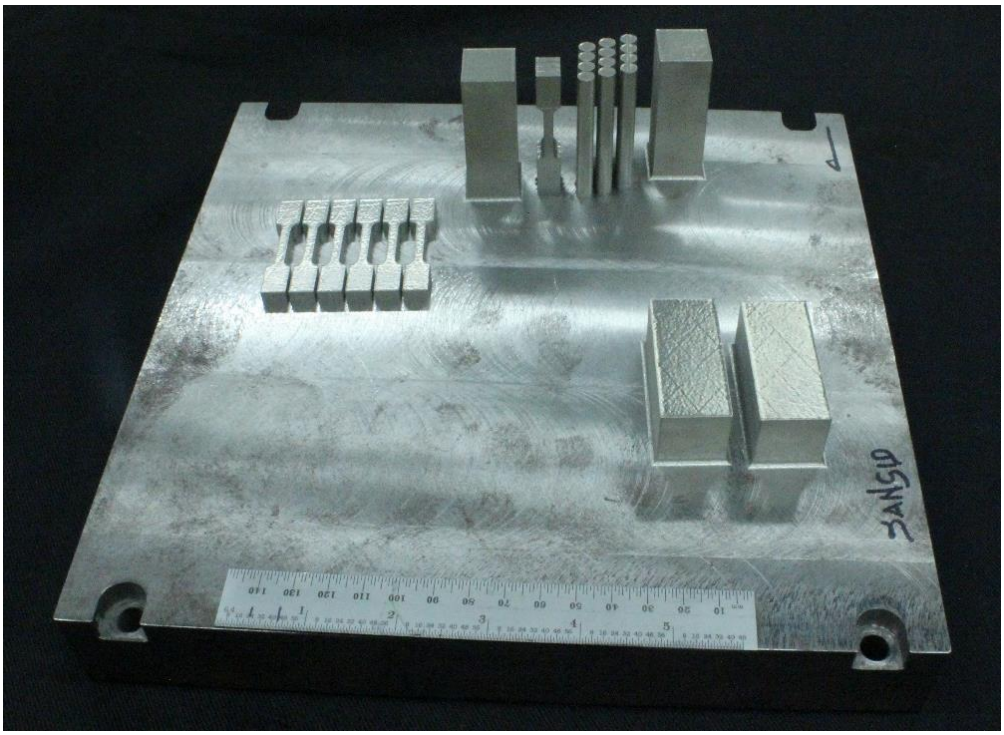

Figure 21: IN718 specimens shown on build plate in as-built state [103]

After the specimens were fabricated and machined (if need be, per their design specifications), they then underwent one or more post-processing treatments as detailed in Table 2 and Table 3. The post-processing treatments were originally performed in order to characterize the effect of different common processing techniques on material mechanical response in Book's work [19]. Some treatments are known to be necessary for most AM-fabricated parts to withstand many aerospace use cases (such as stress relief of inherent residual stress or machining of rough surfaces in the as-built parts). Other treatments (such as HIP, annealing, or other heat treatments) are suggested to be employed on components by researchers and manufacturers of AM parts to be able to reach certain desired material performances. As such, stress relief was performed to all specimens, referred to as SR, and other post-processing treatments were selectively chosen for some specimens, referred to as PP. As shown in Table 2 and Table 3, a SR, homogenization procedure, solution anneal, and aging process were performed for PP IN718 while SR and anneal were performed on Ti64.

For different materials, processing treatments can be utilized for improving different qualities. For IN718, stress relief was performed while the structures were still on the build plate, before EDM wire cutting the parts from the plate, to prevent warping from the cutting process [104]. Next, homogenization was performed to level microscale concentration differences of dendritic and interdendritic regions commonly seen in superalloys [105]. Next, a solution anneal procedure, which can enhance ductility and decrease hardness (making a material more workable), was applied [106]. Lastly, aging (also referred to as precipitation heat treatment), which can strengthen and harden the material due to precipitation of materials in the alloy, was conducted [107]. Surface

finishing including machining, shot peening, and/or polishing can be employed to improve adherance to design dimensions and performance characteristics but was not performed on any of the specimens examined, except for the EDM wire cutting of the specimen off of the build plate [19]. Similarly for Ti64, stress relief was performed pre-removal from the build plate, primarily to prevent distortion, but the process also has the ability to improve crack growth resistance in the material [104]. Following, only an annealing procedure was performed for the Ti64 PP specimens per AMS2801B specifications [108].

Table 2: List of post-build treatments of IN718 specimens consisting of a thermal stress relief, homogenization, solution anneal, and aging

IN718 Post-Build Treatments	
Stress Relief (SR)	1.5 hours -5/+15 minutes at 1950 °F (1066 °C), 2-4 bar argon quench
Post-Processed (PP)	1) SR
	2) Homogenization: 1 hour at 2150 °F (1177 °C) in a vacuum, gas fan argon quench, 100 °F per minute cool down to 1000 °F
	3) Solution Annealed: 1725-1850 °F for a time commensurate with cross-sectional thickness and cooling at a rate equivalent to an air cool or faster
	4) Aging: 8+ hours at 1325 °F ± 15 (718 °C ± 8), cooling at a rate of 100 °F ± 15 (56 °C ± 8) degrees per hour to 1150 °F ± 15 (621 °C ± 8); may also be furnace cooled at any rate provided the time at 1150 °F ± 15 (621 °C ± 8) is adjusted to give a total precipitation heat treatment time of not less than 18 hours

Table 3: List of post-build treatments of Ti64 specimens consisting of a thermal stress relief and mill anneal per AMS2801B specifications

Ti64 Post-Build Treatments	
Stress Relief (SR)	Soaking for 2 hours ± 0.25 at 1100 °F (593 °C) and air or furnace cooling
Post-Processed (PP)	1) SR
	2) Annealing: 2 hours ± 0.25 at 1300 °F (704 °C) and air or furnace cooling

3.1.2 Data Acquisition

After performing post-build treatments, the specimens were then CT scanned to obtain tomographic data. Tomographs were obtained at two different resolutions, 30 μm (50.8 mm / 1680 pixels) and 0.65 μm (1 mm / 1532 pixels) per pixel, by Peter Coutts at PSU's CIMP-3D facility and by Dr. Michael Sangid (Purdue University) at the Advanced Photon Source at Argonne National Laboratory (APS), respectively. To differentiate the two different data sets, the 30 μm data will be referred to as Low Resolution (LR) and conversely the 0.65 μm data will be referred to as High Resolution (HR). Since HR CT scanning is characterized by a deeper penetration of the X-rays compared to traditional X-ray tubes, the result is a much larger data file that takes longer to scan per unit volume [109]. As such, smaller sections were machined from the AM parts for those scans. Figure 22 depicts the machining and sectioning for the HR specimens. Samples were EDM wire cut from near the surface "near-surface" and in the inner bulk "in-bulk" of a selected bulk LR specimen, as shown, with one sample being CT scanned and another held as a backup. Two volumes were scanned from each specimen to provide a greater amount of porosity data for analysis.

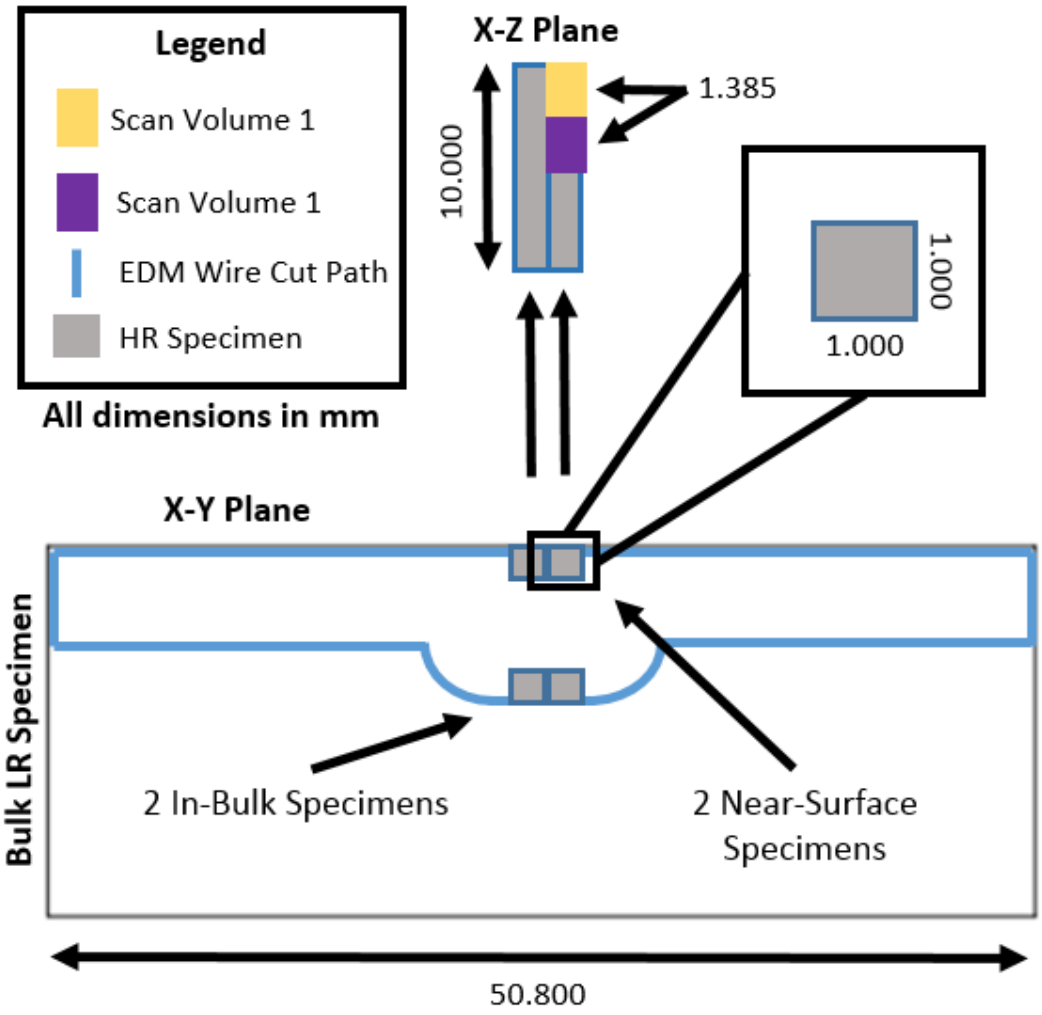

Figure 22: High resolution specimen diagram

A complete list of specimens analyzed for this research is shown in Table 4 and Table 5 for LR and HR, respectively. It should be noted that samples HR-I1, HR-I2, HR-I3, and HR-I4 were cut directly from the specimen for LR-I4. Similarly, HR-T1, HR-T2, HR-T3, and HR-T4 were cut from LR-T8 and HR-T5, HR-T6, HR-T7, and HR-T8 were taken from LR-T9.

Table 4: Low resolution specimens

Specimen ID	Specimen Reference IDs		Material	Resolution [µm]	Specimen Type	Build Direction	Processing State
	PSU CT ID	Book ID					
LR-I1	Tens_2	1F	IN718	30	Dog-bone	Horizontal	SR
LR-I2	Tens_4	1B	IN718	30	Dog-bone	Vertical	SR
LR-I3	Tens_3	1C	IN718	30	Dog-bone	Vertical	PP
LR-I4	Block_2	3B	IN718	30	Bulk	Horizontal	SR
LR-I5	Block_1	3A*	IN718	30	Bulk	Vertical	SR*
LR-T1	Tens_XY-x1	2A	Ti64	30	Dog-bone	Horizontal	SR
LR-T2	Tens_XY1	2B	Ti64	30	Dog-bone	Horizontal	SR
LR-T3	Tens_XY2	2C	Ti64	30	Dog-bone	Horizontal	PP
LR-T4	Tens_XY3	2D	Ti64	30	Dog-bone	Horizontal	PP
LR-T5	Tens_Z1	2E	Ti64	30	Dogbone	Vertical	SR
LR-T6	Tens_Z2	2F	Ti64	30	Dog-bone	Vertical	SR
LR-T7	Tens_Z4	2H	Ti64	30	Dog-bone	Vertical	PP
LR-T8	Block_XY_2	4A	Ti64	30	Bulk	Horizontal	SR
LR-T9	Block_XY_1	4C	Ti64	30	Bulk	Horizontal	PP
LR-T10	Block_Z1	4D	Ti64	30	Bulk	Vertical	PP
*uncertainty in data labelling – may be PP							

Table 5: High resolution specimens

Specimen ID	Specimen Reference IDs			Material	Resolution [µm]	Specimen Location	Build Direction	Processing State
	APS CT ID	PSU CT ID	Book ID					
HR-I1	Exp044	Block_2	3B	IN718	0.65	Near-surface	Horizontal	SR
HR-I2	Exp045	Block_2	3B	IN718	0.65	Near-surface	Horizontal	SR
HR-I3	Exp046	Block_2	3B	IN718	0.65	In-bulk	Horizontal	SR
HR-I4	Exp047	Block_2	3B	IN718	0.65	In-bulk	Horizontal	SR
HR-I5	Exp048	N/A	3D	IN718	0.65	Near-surface	Horizontal	PP
HR-I6	Exp049	N/A	3D	IN718	0.65	Near-surface	Horizontal	PP
HR-I7	Exp050	N/A	3D	IN718	0.65	In-bulk	Horizontal	PP
HR-I8	Exp051	N/A	3D	IN718	0.65	In-bulk	Horizontal	PP
HR-T1	Exp052	Block_XY_2	4A	Ti64	0.65	Near-surface	Horizontal	SR
HR-T2	Exp053	Block_XY_2	4A	Ti64	0.65	Near-surface	Horizontal	SR
HR-T3	Exp054	Block_XY_2	4A	Ti64	0.65	In-bulk	Horizontal	SR
HR-T4	Exp055	Block_XY_2	4A	Ti64	0.65	In-bulk	Horizontal	SR
HR-T5	Exp056	Block_XY_1	4C	Ti64	0.65	Near-surface	Horizontal	PP
HR-T6	Exp057	Block_XY_1	4C	Ti64	0.65	Near-surface	Horizontal	PP
HR-T7	Exp058	Block_XY_1	4C	Ti64	0.65	In-bulk	Horizontal	PP
HR-T8	Exp059	Block_XY_1	4C	Ti64	0.65	In-bulk	Horizontal	PP

A CT system operates utilizing several different parts as depicted in Figure 23. First, the component of interest is placed on a stage that can have rotational and translational degrees of freedom [102]. Next, X-rays from an X-ray source illuminate the rotating and/or translating component [102]. X-rays pass through the object and are attenuated due to absorption or scattering [110]. The amount of X-ray attenuation is determined by several factors including by the intensity of energy of the X-rays, the length

traveled by the X-rays within the absorbing material, the composition of the material, and material density [110]. The attenuation that occurs is then measured via a detector that picks up the X-rays after passing through the component, resulting in a 2D gray image [102][110]. A specific volume of the object of interest is able to be captured as multiple images are taken from different angles and positions of the part [110]. These images are later mathematically reconstructed into 2D tomographic images for image processing and analysis [102].

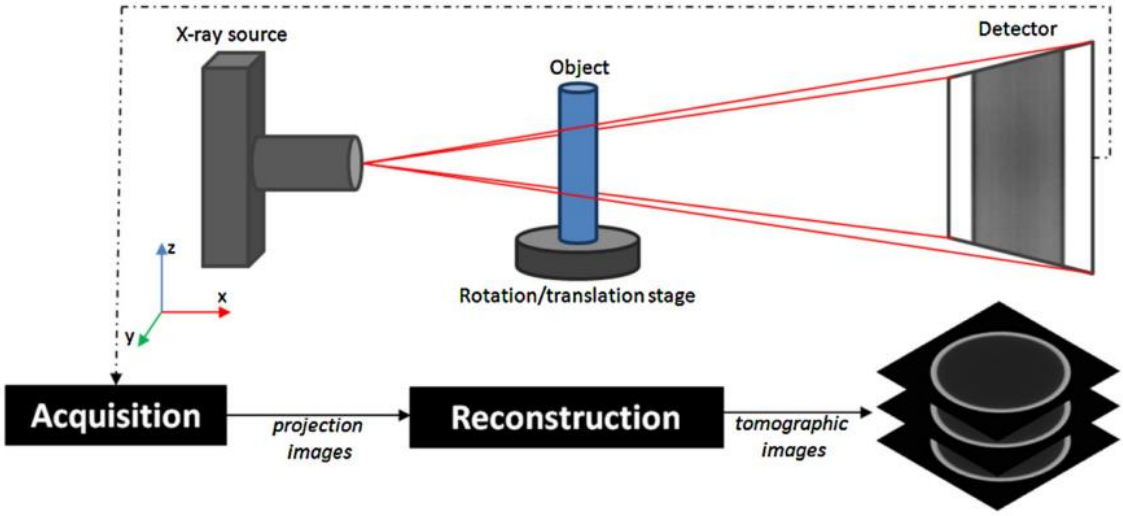

Figure 23: General schematic of X-ray industrial tomography [102]

The 30 μm resolution CT Scan at CIMP-3D was obtained on a GE Phoenix V Tome X M 300 CT System, as shown in Figure 24, with exact settings not provided by CIMP-3D. This system features "industry leading magnification and power" via a dual x-ray tube setup at both 300 kV and 180 kV [111]. It also includes GE's proprietary scatter|correct® technology for improved CT quality above a conventional microfocus cone beam system [111]. Actual experimental setup at CIMP-3D is depicted in Figure 25. The

aforementioned system is a typical commercially available CT system employed by industry.

In contrast, the 0.65 μm resolution CT scan was conducted at the APS synchrotron and was obtained on their 2-BM beamline operating in white beam mode with 2130 projections taken over 180° with a 50 ms exposure time. Synchrotron radiation is an electromagnetic wave that is emitted from charged particles and forced to travel in a curve, with speed approaching the speed of light [109]. Synchrotron X-ray beamlines differ from conventional X-ray tubes in a few different ways. First, the brightness from the produced ray is over a million times greater than that of conventional X-ray tubes [109]. As such, the signal captured from the photon emissions is high enough to observe even very dilute concentrations of a specie within a material [109]. Also differing from singular X-ray tubes, synchrotron beamlines are in the form of long straight beams, allowing for greater experimental customization of a specimen [109]. Furthermore, the high degree of beam collimation increases energy resolution and allows for deeper penetration of a sample [109]. In all, the greatest advantage for this research of utilizing a synchrotron X-ray is the higher resolution at which materials are able to be investigated, allowing for the possible discovery of porosity trends unnoticed with conventional X-ray CT.

Figure 24: GE Phoenix V Tome X M 300 CT System [112]

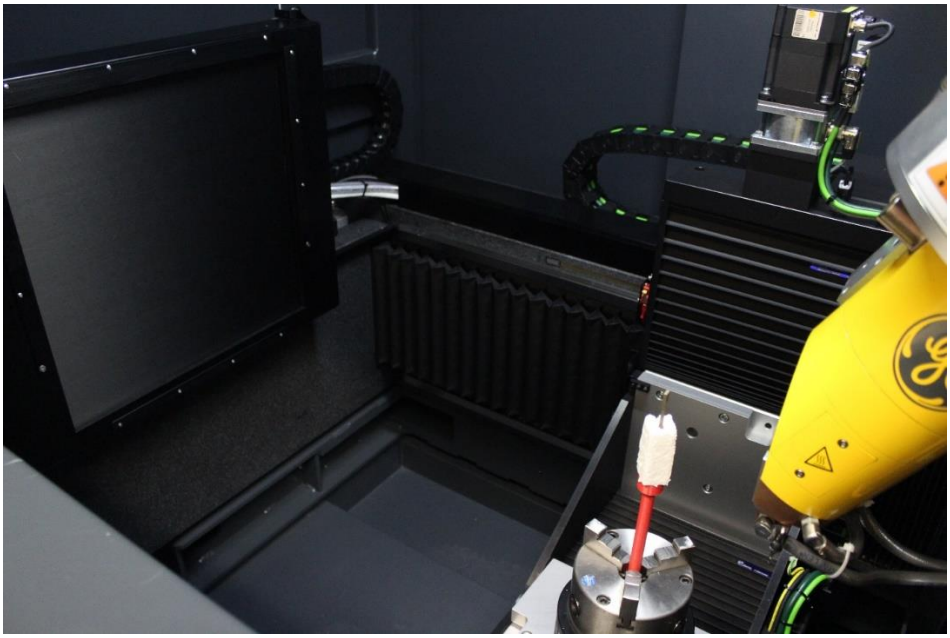

Figure 25: CT experiment setup conducted at PSU CIMP-3D at 30μm resolution [112]

3.2 Data Processing and Analysis

3.2.1 Reconstruction

Tomographic reconstruction is the process of assembling together specific projection images to obtain an estimate of the structure of interest by solving a multidimensional mathematical inverse problem [113]. The inputs for the reconstruction are the different gray value intensities captured on the projection image. These intensities represent the differences in absorptivity of the material and can be traced back to different materials or pores for purposes of identification and quantification [110]. The reconstruction algorithm takes in the detector data file format and outputs a traditional image file format (i.e. .tiff).

One of the biggest influencers on creating an accurate reconstruction is to find the correct center of rotation of the component. Commonly, the center of rotation is a variable that is required to be set in the inputs of the reconstruction code and has a large influence on the ability to resolve features within a 2D tomograph. Figure 26a shows a 2D tomograph with an off-center of rotation input and Figure 26b shows the same tomograph with an accurate center of rotation for reconstruction. Whereas features including edges and internal material defects were previously indistinguishable in the former image, they are clear and defined in the latter.

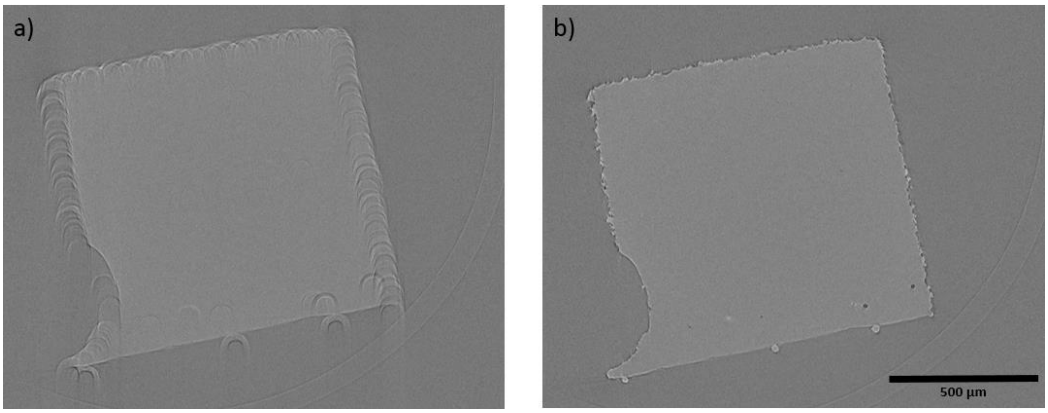

Figure 26: a) IN718 2D radiograph off-center and b) same radiograph after proper center determination

Another strong influencing factor in the quality of reconstructed images is the removal of artifacts that are inherent to the CT scan system. An artifact is a distortion of the image that is not a feature of the actual component. A number of varying phenomenon can cause artifacts including defective pixels that are not accounted for or removed (ring artifacts) as well as sub volumes of the component that absorb the X-rays at a much higher rate than the rest of the component (metal artifacts), among others [110]. Reconstruction software generally have code built in to remove artifacts but some are still usually present in the final tomograph output. The presence of artifacts can influence the analysis of tomographs and should be mitigated if possible, however, some have a negligible effect. An example of a ring artifact is clear in the lower right corner of Figure 26a and Figure 26b that was later cropped out during image processing.

Two other phenomena that may reduce the accuracy of reconstructed images are beam hardening and scatter [110]. Beam hardening is a result of the fact that when X-rays move through the component, low energy photons are attenuated at a faster rate than high energy photons [110]. The resulting effect is that after having passed a certain distance

through the material, the soft X-rays are eliminated and only hard X-rays fully traverse the specimen and reach the detector [110]. This phenomenon displays on a reconstructed tomograph as the edge of the component having a much higher gray intensity (larger accumulation of soft and hard rays) than the interior of the component. Similarly destructive to the reconstructed image, scatter is caused by the deflection of rays in the material, detector, or aperture [110]. Scatter results in an image with a low local signal to noise ratio in affected areas as well as a halo-like artifact without a dedicated structure at the location of the component [110]. It should also be noted that the number of images taken and the exposure time of each during data acquisition contributes to determining the signal to noise ratio. Kruth et al. noted some of the negative effects of beam hardening and scatter, including difficulty in thresholding, observed in Figure 27 [110].

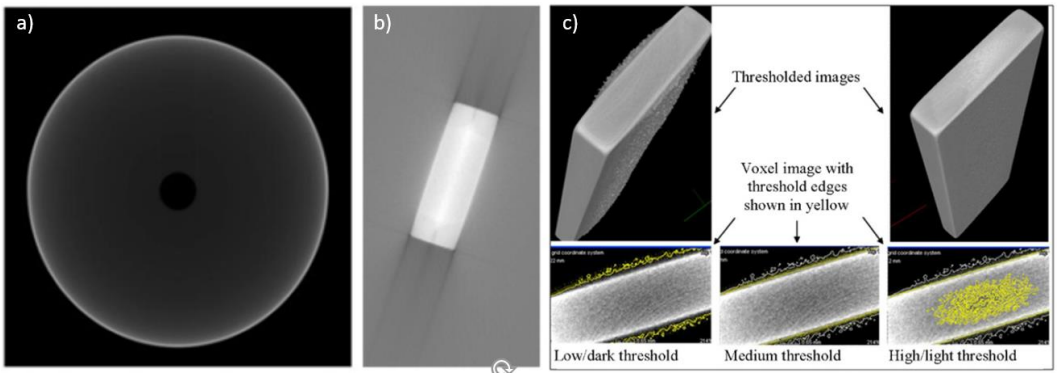

Figure 27: a) example of beam hardening with higher X-ray absorption visible on outer edges b) example of scatter with black artifact stripes visible c) difficulty in thresholding due to effects of beam hardening and scatter (high S/N ratio and gray level variation) [110]

The LR data set was CT scanned and reconstructed at CIMP-3D facilities with grayscale images provided for analysis. The HR data was CT scanned at APS with

reconstruction performed by the author as part of this thesis work. To perform the HR reconstruction, the software TomoPy 1.0.0 was used.

TomoPy is a high performance, parallelizable, open-source python package that was developed at APS for data processing and image reconstruction of tomographic images [114]. TomoPy reconstruction was conducted on Linux Ubuntu 17.04 operating system software. The TomoPy code is controlled through a user-manipulated script that allows for reconstruction customization per the experimental set up of the specific CT scan. The code allows the user to first survey several images for a specific specimen that are used to determine the center of rotation. Once the center is accurately identified, the code commences to fully reconstruct the scanned volume to produce a stack of 2D tomographic tiff files. In section 3 of Figure 28, the workflow and tasks performed by TomoPy for this research work is displayed in a diagram. TomoPy was utilized to reconstruct raw hdf data into 2D tomographic tiff stacks and further image processing was performed externally of the code. The specific reconstruction process performed by TomoPy in this research, controlled by a script developed by Dr. Xianghui Xiao at APS is as follows [114]:

1. Creation of sonograms from raw detector data
2. Removal of corrupted images, if present
3. Removal of high intensity bright spots by a dual process of chunking (grouping together) and application of a median filter
4. Normalization of projection images by use of the flat and dark field projections, helping to remove artifacts created by the pixel-to-pixel variations in the detector
5. Removal of horizontal stripes in the sonogram using a Fourier-Wavelet-based method [115]

6. Single-step phase retrieval using phase-contrast measurements [116]
7. Reconstruction via the Fast Filtered Back Projection, based upon the Fourier grid reconstruction algorithm [117]

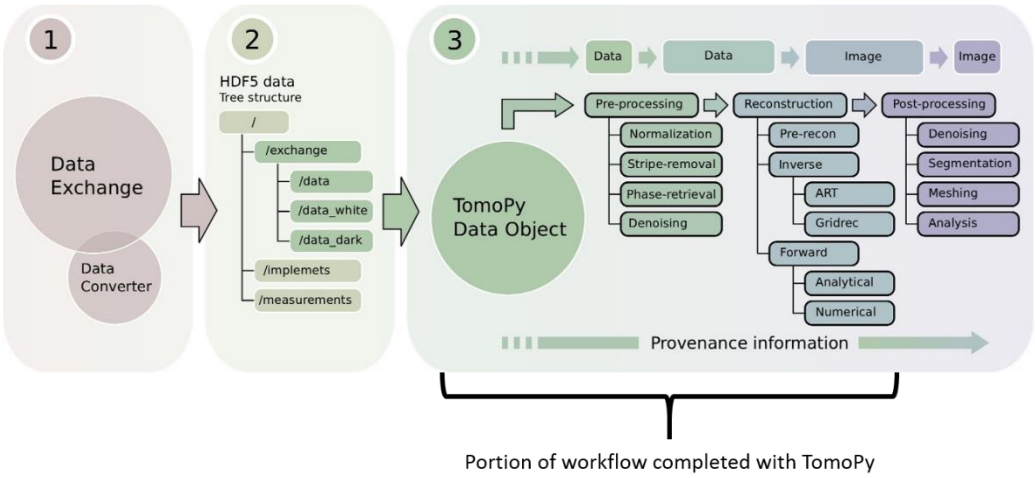

Figure 28: Workflow diagram of tomographic data processing workflow including Tomopy usage [118]

Overall, the reconstruction phase of CT analysis for porosity is important because it lays the foundation for accurate and hassle-free future image processing, visualization, and quantification. Errors, noise, beam hardening, scatter, and artifacts present in a reconstructed tomograph (if not reduced during reconstruction) can propagate throughout the workflow and as a result can increase image processing time (to remove image defects) and/or result in a larger error in final quantification.

3.2.2 Image Processing

In their work exploring the quantitative applications of computed tomography, Maire and Withers explain that to be able to obtain accurate quantitative data from tomographic images, appropriate image processing, segmentation, and analysis is required

[119]. Specifically, image processing is used to "improve" an image so that it is easier to segment [119]. Mostly, image processing involves the altering of grayscale values of an image through normalization, equalization, noise reduction, and contrast adjustment [119]. In the current research, image processing was performed on both LR and HR datasets utilizing the open-source software ImageJ as well as the commercial software Avizo 9.2.0 [120][121].

ImageJ is a software that was developed by the National Institute of Health to originally process bioimagery; however, it has been adopted and applied to a wide range of image processing needs in many disciplines. ImageJ contains tools to filter, segment, and enhance images, among other options. One of the most appealing features of ImageJ is the ability to adjust stacks of 2D images and easily view them. Furthermore, one of the largest timesaving features of the software is the ability to create user macros and utilize them to process stacks in batch format. User macros are an intuitive and effective scripting platform that reduces the repetition inherent in processing many different datasets.

Avizo is a commercial software distributed by FEI Visualization Sciences Group for the purpose of data visualization and analysis. In addition to the visualization capabilities of Avizo, which are necessary for the analysis of porosity in this thesis, the software also has many of the same image processing capabilities as ImageJ. ImageJ was the primary tool of choice for image processing because of the simplistic user interface preferred by the researcher; however, Avizo was also utilized for certain processing features not available in ImageJ.

The step-by-step image processing workflow employed will be detailed for the benefit of potential use by others in similar applications. The workflow was nearly

identical for both the LR and HR datasets, except for an added contrast enhancement filter used on the former. The workflow begins with a 2D tomograph in tiff file format and follows the general progression of: 1) image format conversion, 2) crop and rotate, 3) image grayscale enhancement, and 4) segmentation. The file output is a binary image ready to be quantitatively analyzed.

The LR data image processing workflow is detailed in Figure 29 and displays the exact techniques performed on the image. Figure 29a shows one slice of a reconstructed tomograph as provided by CIMP-3D. The image is originally in a 16-bit red, green, blue (RGB) format but is converted to 8-bit grayscale format, which is necessary to be later segmented. Figure 29b depicts the grayscale image that has been rotated and cropped to align the subject with the image frame coordinate system and eliminate unnecessary image data. Next, the image undergoes a duo of grayscale intensity manipulations. First, to accentuate the features of the subject (i.e. porosity), a sharpening technique called Unsharp Mask filter is applied, as shown in Figure 29c. According to ImageJ documentation, the Unsharp Mask filter "subtracts a blurred copy of the image and rescales the image to obtain the same contrast of large (low-frequency) structures as in the input image" [122]. The resulting effect of the filter is akin to applying a type of high-pass filter, resulting in a sharpening of the image. The second grayscale alteration is the use of an Edge-Preserving Smoothing filter, applied in Avizo. Figure 29d displays the effects of the filter which utilizes a diffusion algorithm that levels out the mismatch in energy levels (grayscale values) between pixels while limiting the effect at detected edges. Thus, the filter smooths noise in an image while preserving edges that could be indicative of porosity. Finally, Figure 29e shows the segmentation result of the tomograph utilizing a local Phansalkar

Method thresholding algorithm. The thresholding process and reasoning for the chosen algorithm will be explained in a later section.

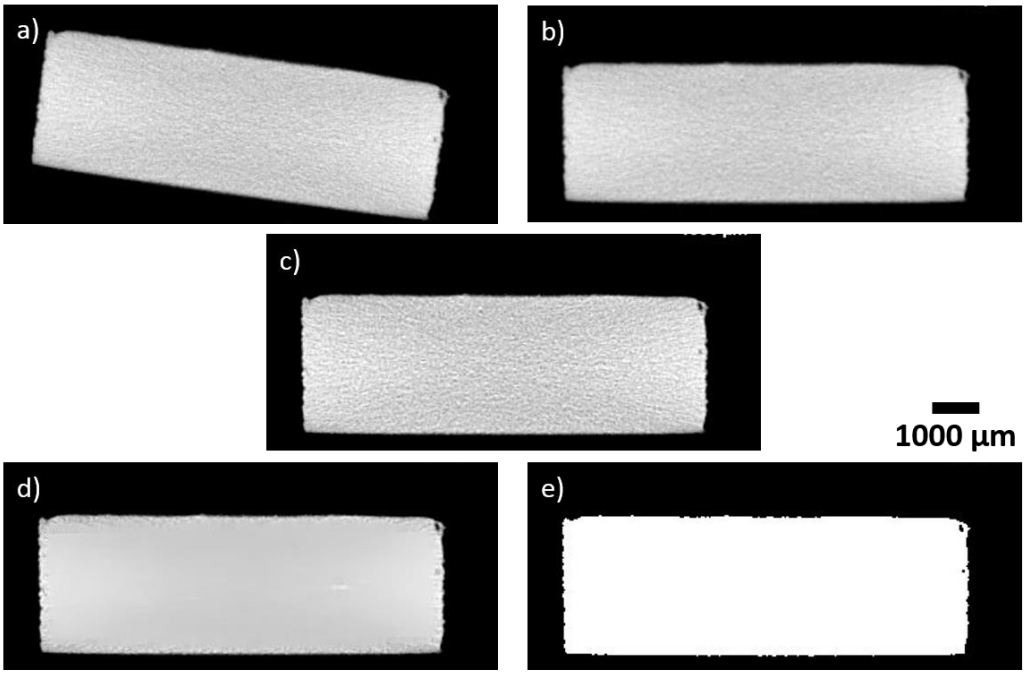

Figure 29: Process of image processing for PSU Ti64 tomograph data starting from the a) original reconstruction in 16-bit RGB to b) 8-bit grayscale, rotated, and cropped to c) unsharp mask filter to d) edge-preserving smoothing filter to e) local Phansalkar Method thresholding

A similar image processing workflow was followed for the HR data, with the omission of a sharpening filter prior to image smoothing. Figure 30a depicts the original HR reconstructed 16-bit RGB image. The image is then converted to 8-bit grayscale for eventual thresholding, rotated, and cropped to eliminate unnecessary information and reduce file size, as shown in Figure 30b. For the HR dataset overall, the reconstructed images were less noisy than the LR dataset and had less grayscale variations across the 2D tomograph as well as throughout the image stack. Furthermore, features of the image were more pronounced in many cases. As such, the sharpening filter was omitted in the

workflow, leaving the next step the application of the Edge-Preserving Smoothing, shown in Figure 30c in preparation for segmentation. Figure 30d displays the result of segmentation via the global Otsu Method thresholding algorithm, which the selection and details of will be explained in a later section of this thesis.

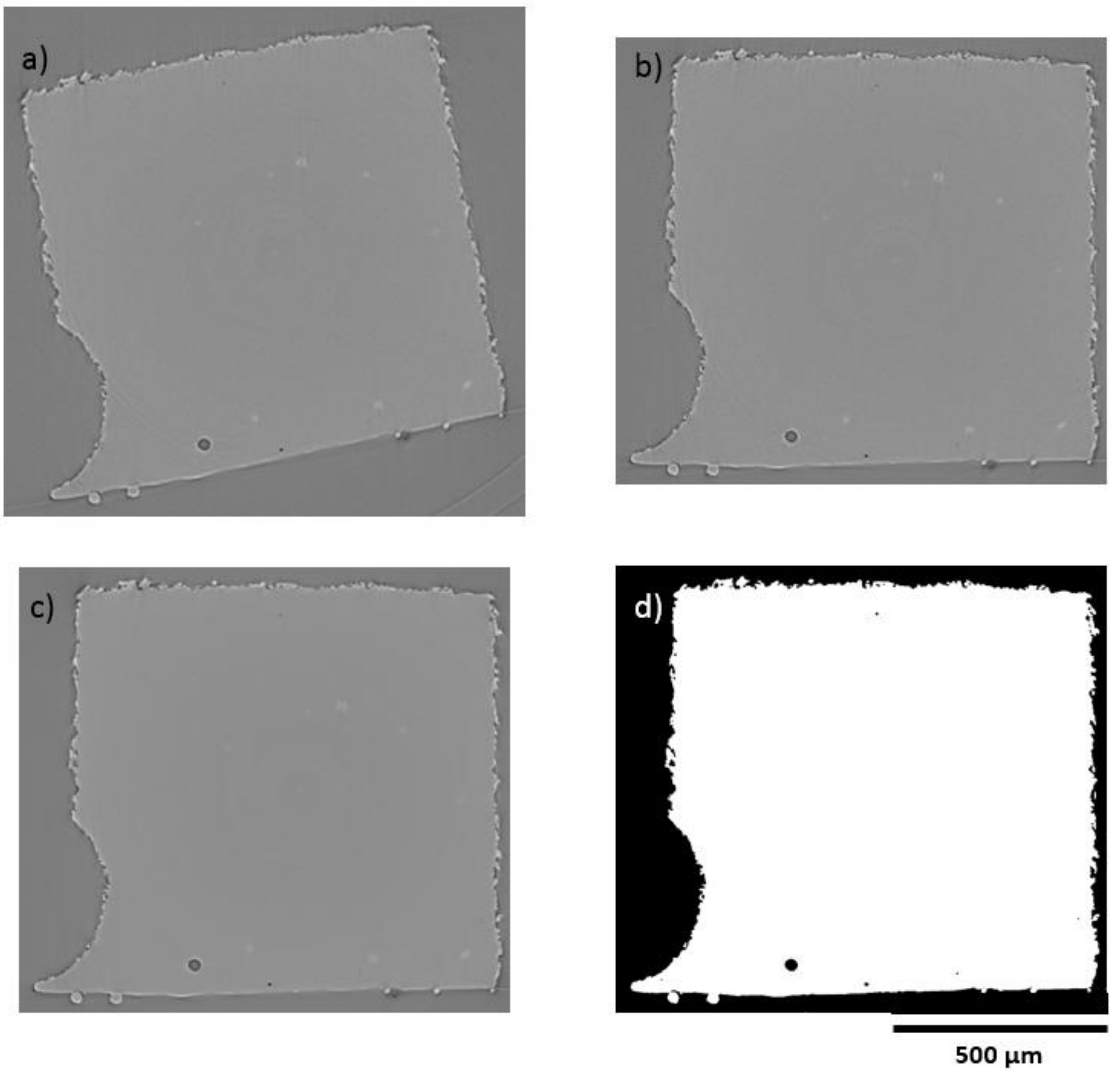

Figure 30: Process of image processing for APS IN718 tomograph data starting from a) original reconstruction in 16-bit RGB format to b) 8-bit grayscale format, rotated, and cropped to c) edge-preserving smoothing filter to d) Otsu Method thresholding

Image type conversion, cropping, and rotation are all part of many image processing workflows for tomographic analysis. Image type conversion is necessary to be able to apply image segmentation thresholding algorithms in ImageJ. Cropping and rotation are not always necessary to reach an accurate segmentation but are recommended to ease the application of future processing steps for the user. Rotation helps the user to align the subject for effective cropping. Additionally, cropping is important to remove unwanted image information that could alter segmentation results while also reducing file size to improve computation time.

The unsharp mask filter was chosen to be used because previous attempts at thresholding the unaltered 8-bit grayscale image was affected by noise and beam hardening grayscale variations, resulting in binarization that overstated existing porosity. After a smoothing filter was applied to mitigate these effects, the binarization showed contrasting results with the original attempt by not being able to capture clear existing porosity (identified by eye). As such, the Unsharp Mask filter was applied to enhance features to a level that would survive the smoothing effects of the latter filter.

According to the Avizo User's Guide, smoothing is the most important technique for preparing an image for eventual segmentation [123]. This is true because noise is one of the largest influencers on image segmentation [110]. Smoothing filters can effectively reduce noise but must be applied carefully so as not to alter information that is critical for quantification analysis (as described in the justification for using the Unsharp Mask filter). The Edge-Preserving Smoothing filter (available in Avizo) was applied, specifically, because it reduced noise in the image while leaving detected edges intact. Edges were important to leave unaltered in the image because they often represented the boundaries of

pores in the tomograph. As such, the edges represented a critical feature for accurate porosity quantitative characterization.

3.2.3 Segmentation and Thresholding

Image segmentation encompasses the methods and processes that are used to separate an image into multiple parts, with the purpose of making the image data more meaningful and easier to analyze [124]. Image segmentation can be performed using numerous methods including thresholding, clustering, compression-based, region-growing, watershed, multi-scale, and more [124]. Of those methods, thresholding is one of the simplest, especially for binarization (as opposed to multi-level segmentation), and was employed for this research. Past researchers in computed tomography for materials characterization have also widely used thresholding for segmentation [64][110][102][125]. This method is applied by picking a threshold value to convert a grayscale image into a binary image from the image gray level histogram, shown in Figure 31. All grayscale values below the threshold value will convert to white and all values above will convert to black, or vice versa as defined by the user. From then on, the binary image can be more easily analyzed and quantified by computer software for characterization of specific features.

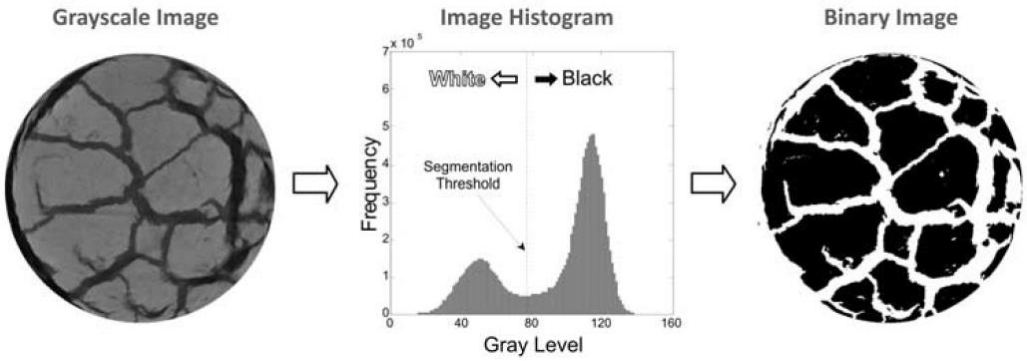

Figure 31: Illustration of histogram-based thresholding binarization of a tomographic image [125]

The process of thresholding a tomographic volume, while able to be done manually, is more efficiently and often more effectively performed by an automatic algorithm that can evaluate and convert stacks of 2D tomographic slices at a faster rate. Manual thresholding can also be inconsistent, with user bias and likely errors that can be difficult to correct for [125]. Automatic thresholding algorithms can be classified into global or local methods. Global methods will analyze an entire image slice histogram, when operating in 2D (as opposed to 3D which utilizes 3D images), to compare grayscale intensities and determine one optimal threshold value to set for the entire image [125]. On the other hand, local methods will compare only neighboring pixel grayscale values with each other and determine multiple threshold values to utilize for different sections of the image [125]. Local thresholding methods are often perceived as a refinement of global methods based on local image characteristics [125]. Within the global and local categories, there are different algorithms that have been developed for segmentation. To choose the correct algorithm to apply for LR and HR datasets, respectively, a comparison of the various options was performed.

Several global and local methods were applied to the processed images and compared by global vs. global, local vs. local, and global vs. local. For the purpose of this thesis, a description of each global and local thresholding algorithm available in ImageJ will be presented in Table 6 and Table 7 as well as a detailed comparison made of one LR specimen and one HR specimen with the algorithms applied. Finally, the determination of the appropriate thresholding algorithm for each data set will be discussed.

Table 6: Description of global thresholding algorithms available in ImageJ

Name	Description
Default	A ImageJ specific algorithm based off the IsoData method (see IsoData) [126].
Huang	Selects a threshold that minimizes the "fuzziness" of an image, measured by Shannon's function of entropy, which is determined using the membership function (the absolute difference between the gray level and the average gray level of a pixel's belonging region) [127].
Minimum	Assumes a bimodal histogram that is iteratively smoothed until only two local maxima remain. The threshold value is taken at the valley between the two peaks [128].
Moments	Based upon the moment-preserving principle of subpixel edge detection, this algorithm enacts a moment-preserving image transformation which recovers an ideal image from a blurred version by calculating the gray-level moments of the input image and selecting a threshold value that keeps them unchanged [129].
Li	The threshold value is computed by application of an iterative convergence of the minimum of the cross entropy of the image; the cross entropy is defined using the means of the zeroth and first moments of the foreground and background portions of the threshold histogram [130].
MaxEntropy	This algorithm chooses a threshold value such that the maximum image entropy is obtained, which allows for the maximum information between the object and the background distributions in the picture [131].
RenyiEntropy	This algorithm is similar to the MaxEntropy method but maximizes Renyi's entropy of the background and foreground images instead of Shannon's [132].
Shanbhag	A threshold is selected that minimizes the difference of average information obtained by categorizing two classes of gray levels (object and background) through use of a membership coefficient of their intensity probabilities [133].

Table 6 continued

Intermodes	Similar to the Minimum method, assuming a bimodal histogram, the threshold value is taken as the average of the max intensities of the remaining two peaks after iterative smoothing [128].
IsoData	This algorithm separates an image into foreground and background classes by choosing an initial threshold, averaging the pixels equal to or less than that value as well as those above, and iterating until the value is larger than the combined average of the two classes' averages [134].
Otsu	Calculates the threshold value that minimizes the inter-class variances of background and foreground, which are grouped using cumulative second order moments of the image pixels [135].
Percentile	This method assumes a background/foreground pixel split of 50/50 and calculates the median threshold [136].
Mean	Uses the mean gray value intensity as the threshold [137].
MinError(I)	Using a criterion function that reflects the amount of Gaussian model overlap between the background and foreground pixels, the threshold value is selected to minimize that overlap [138].
Triangle	The threshold is selected by normalizing the height and dynamic range of the intensity histogram, locating the inflection point of max intensity value, and then adding a fixed offset [139].
Yen	The threshold value is select by finding an intensity that can optimally maximize the image entropy while minimizing a cost function determined by the number of bits needed to represent the thresholded image [140].

Table 7: Description of local thresholding algorithms available in ImageJ

Name	Description
Bernsen	This method calculates the local contrast (max-min) gray level and if it is above or equal to a user-provided contrast threshold, then the threshold value is set at the local mid-grey value (the mean of the min and max grey values in the local survey area). If the local contrast is below the contrast threshold, then the local area is considered to be of one class and the pixels are set to be foreground or background dependent upon the value of the mid-grey [141].
Contrast	This algorithm sets the pixel value to background or foreground depending on whether the gray value is closest to the local maxima or minima [142]
Mean	The threshold value is set as the mean of the local grayscale distribution [143].
Median	The threshold value is set as the median of the local grayscale distribution [143].
MidGrey	The threshold value is set as the mid-grey of the local grayscale distribution [143].
Niblack	The threshold value is set as the local mean gray value plus the local standard deviation (scaled by a user defined constant), minus another user defined constant. The default standard deviation scaling factor is 0.2 for bright objects and -0.2 for dark objects [144].
Otsu	Otsu method, as defined previously, applied to a local survey area.
Phansalkar	Modified from Sauvola's method (see below), the algorithm adds an exponential term, based off the mean and user-defined constants, to the standard deviation term to deal with low contrast images [145].
Sauvola	Based off Niblack's method (see above), this algorithm instead uses a dynamic range of standard deviation, using a local mean-defined scaling term as well as a fixed, user-defined constant, to amplify the contribution of the standard deviation in an adaptive manner in order to deal with image imperfections such as illumination, noise, and resolution changes [146].

Thresholding within ImageJ was first performed for the LR dataset. Figure 32 shows the LR Ti64 tomograph slice, post image processing, that will be used for purposes of algorithm comparison. Note the clear pore visible in the slice, as this is the type of feature that is necessary to preserve through the thresholding, and will be used for comparison purposes between the various algorithm options.

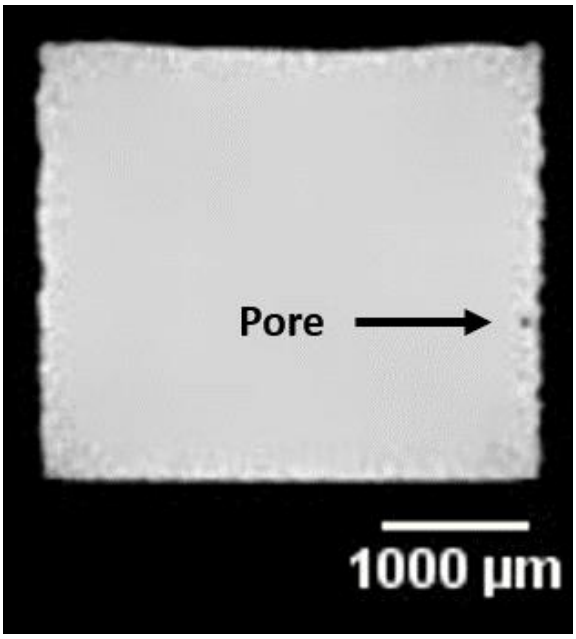

Figure 32: Ti64 LR 2D tomograph slice (post image processing)

First, global thresholding algorithms were applied to determine if they could accurately segment the LR sample. Figure 33 and Figure 34 display the global thresholding options in ImageJ applied to the slice and it is clear that only the Moments, Intermodes, and Huang algorithms come close to representing the features of Figure 32. These three algorithms are able to pick up the pore that is present, to varying degrees. The other algorithms are unable to accurately segment the image and thus are unusable.

Local methods were also explored, as shown in Figure 35. While some of the local algorithms appear more dramatic in their deviation from accuracy in segmenting the image of interest, it is important to keep in mind that the patterns displayed are a result of the local surveying process. Both the Sauvola and Phansalkar methods appear to accurately segment the image, with the latter being chosen for use on all LR data because of its consistency across different specimens. The Phansalkar method is actually a variation of Sauvola's

method, where the local threshold is determined using the mean and standard deviation of the pixel intensities, with changes made to deal with low contrast images [145].

Possible reasons for the accuracy, or lack thereof, of segmentation by the different global and local methods is varied. It seems that entropy-maximizing algorithms, as seen in Figure 33 for MaxEntropy, RenyiEntropy, and Figure 34 for the Yen method, are the worst of the global methods at creating an accurate segmentation. As seen in the segmentations from these methods applied to the LR Ti64 example image, it seems that the alterations of the example image from the edge-preserving smoothing filter are having a significant effect. As observed in Figure 32, the filter has smoothed gray value variations in the inner portion of the material while leaving a higher variation in a border near the edge of the material. Since the filter is "edge-preserving" in nature, it acts in this manner to not smooth and eliminate features defined by edges, such as the material border and possible pores. Thus, the entropy, the measure of "busy-ness" or information provided in an image (i.e. an image with lots of high contrast from one pixel to the next will have higher entropy than an image of one color), of the smoothed image is higher near the border [147]. The entropoy-maximizing algorithms, by nature, try to maximize the information provided in the image through binarization and thus, are capturing the contrast difference between the smoothed and un-smoothed sections of the input gray image. This action results in a binarization that does not capture the pore of interest. On the other hand, among the algorithms that were able to capture the pore feature through binarization (Huang, Moments, and Intermodes), there seems to be no general trend in the way the algorithms operate that leads to a better result. The Huang method operates by minimizing entropy in an image, opposite of the maximizing entropy methods, while the Moments method tries

to minimize any difference in the calculated intensity value moments between the gray and binarized image, and the Intermodes method is based upon analysis of the max intensities of the image histogram.

Of the local thresholding algorithms, only the Phansalkar and Sauvola methods proved to be usable for binarization. Fittingly, these methods are designed to deal with large contrast differences, illuminations, noise, or other image defects present in the tomographic input. Because of the effects of the edge-preserving smoothing filter, previously discussed, the other local thresholding options were ill-equipped to produce a threshold that was not thrown off by the highly varied intensity border on the grayscale input. However, the Phansalkar and Sauvola algorithms are able to incorporate a dynamic range of the local standard deviation that allows for a more accurate grouping of pixels that have large variations from one to the next.

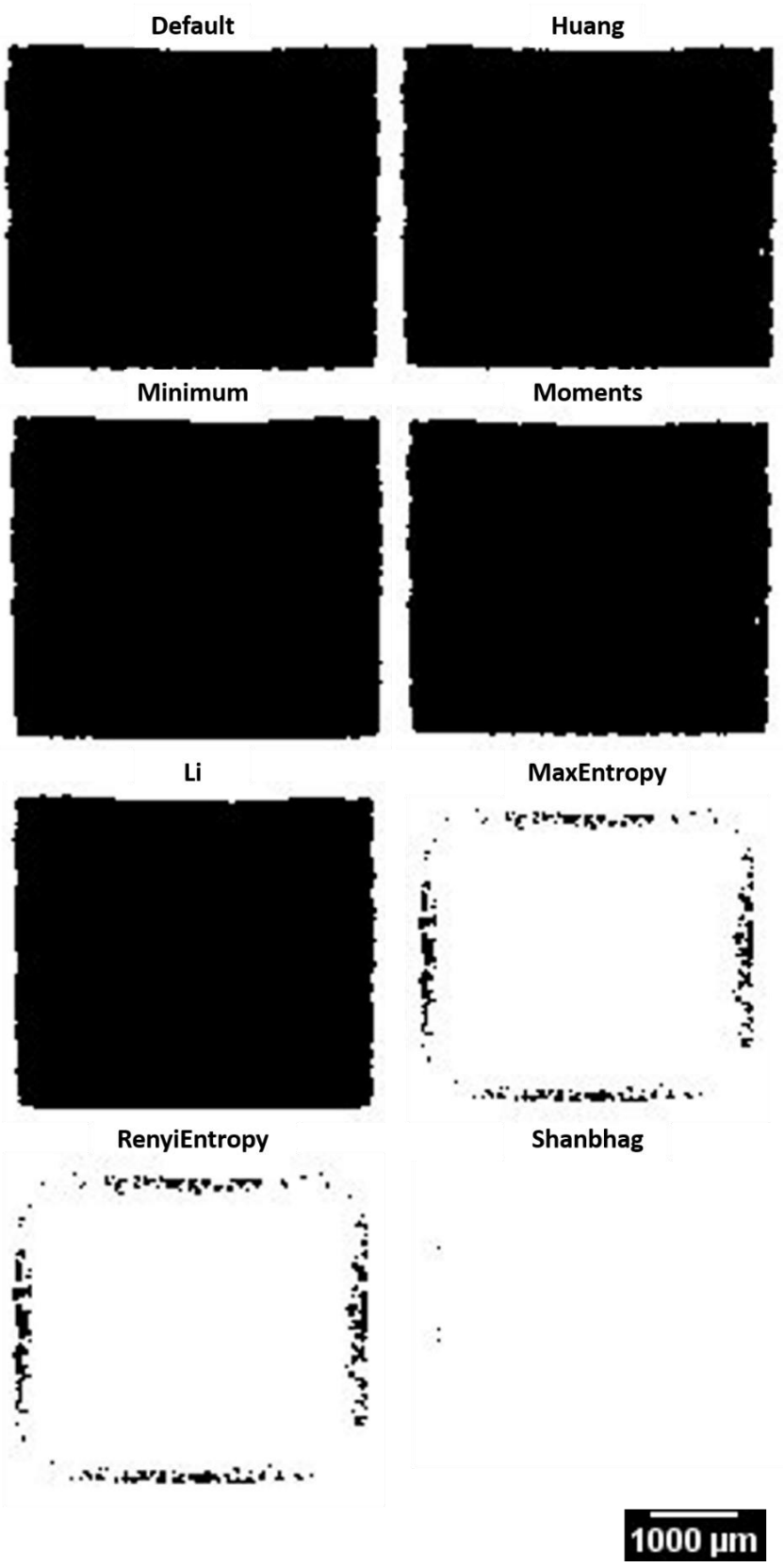

Figure 33: Global thresholding algorithms applied to LR Ti64 data (set 1 of 2)

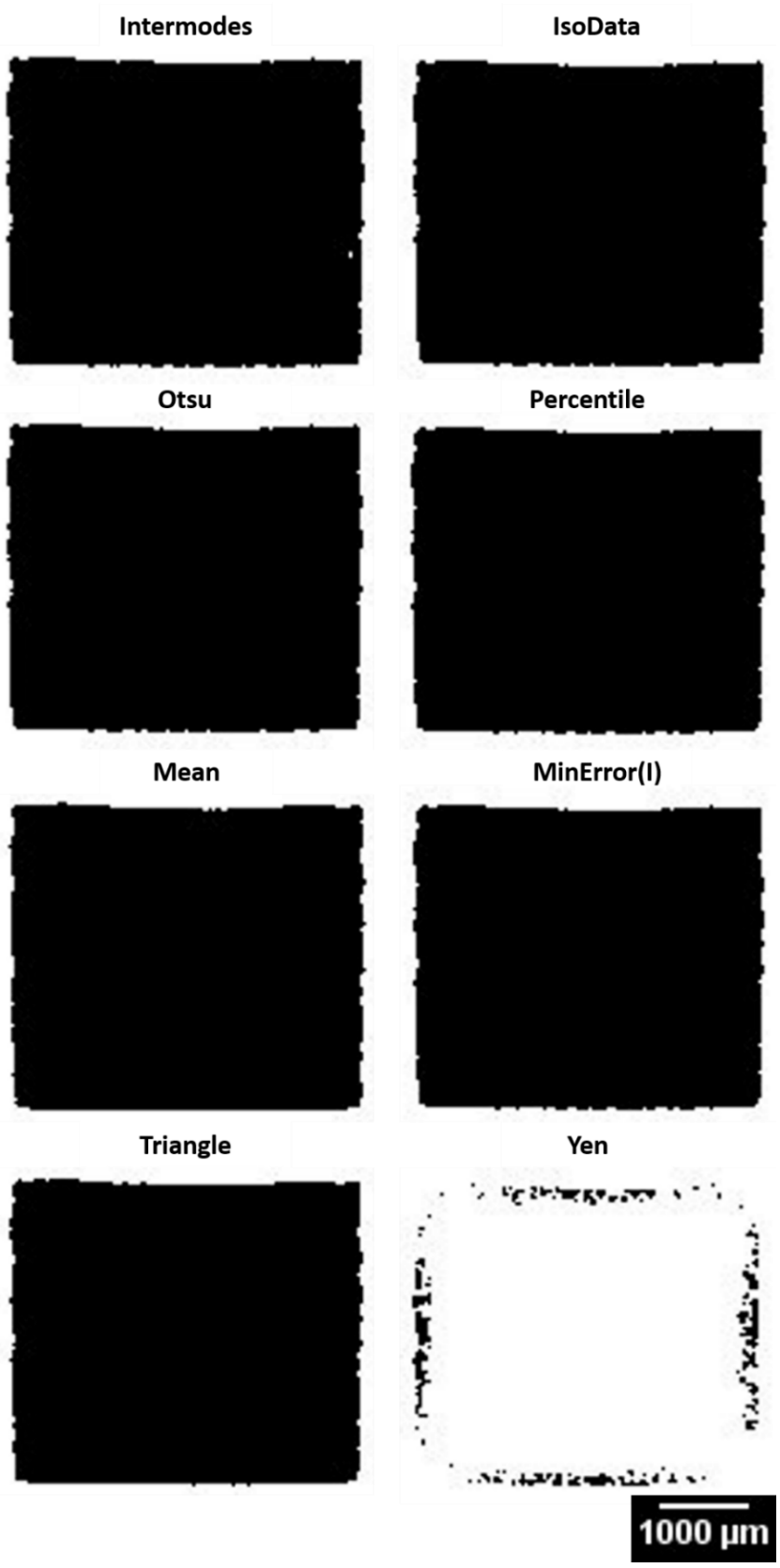

Figure 34: Global thresholding algorithms applied to LR Ti64 data (set 2 of 2)

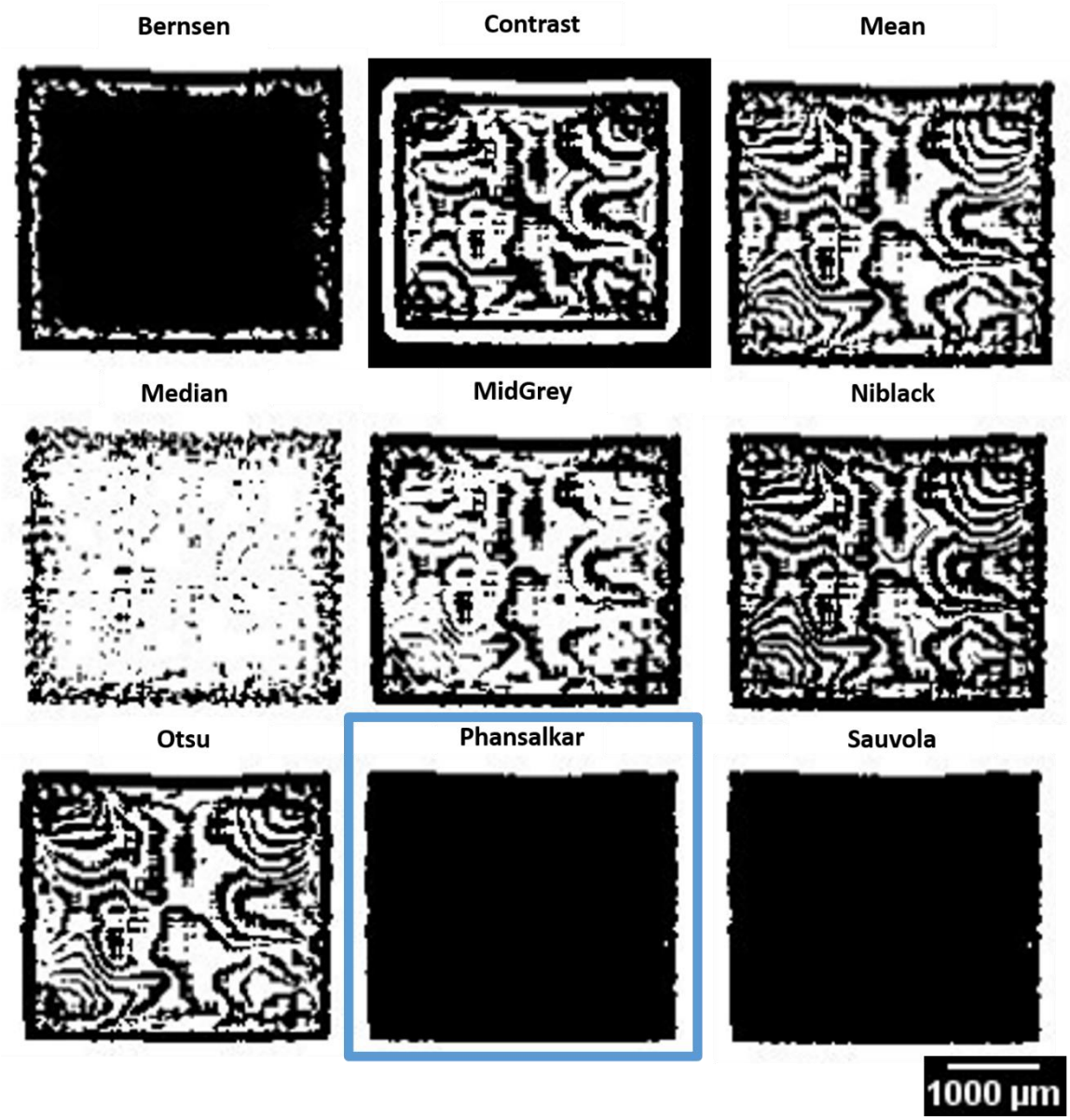

Figure 35: Local thresholding algorithm applied to LR Ti64 data (chosen algorithm outlined in blue)

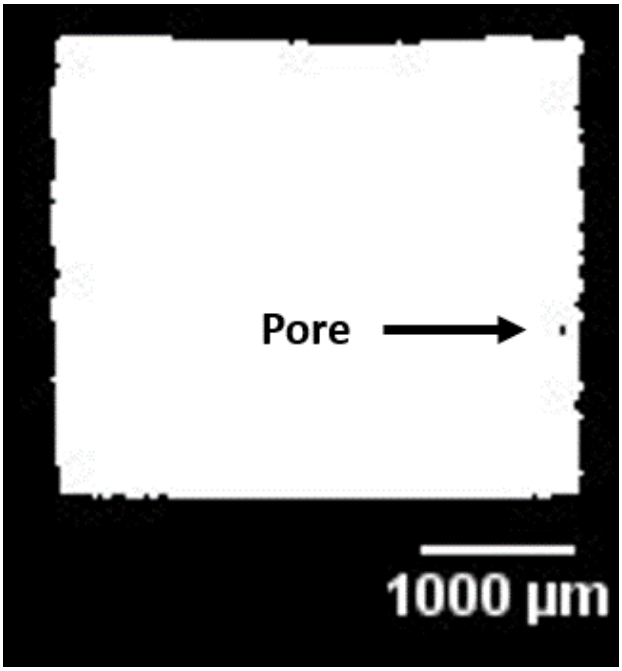

Figure 36: Local Phansalkar method threshold of LR Ti64 2D tomograph slice

Comparisons for the HR dataset was also done for global and local algorithms, yielding a different choice for segmentation of the images than with the LR data. Figure 37 displays the post image processing tomograph slice that will be used for comparison purposes. At least 5 possible voids are observed and marked within the interior of the sample. First, as shown in Figure 38, a comparison of local method algorithms was made. From Figure 38 it is clear that all available local methods had difficulty in segmenting the image with the Bernsen, Phansalkar, and Sauvola algorithms performing the best but not adequate enough. Figure 39 displays the comparison of global methods with several faring better than the local methods and able to reach a higher level of accuracy in segmentation. Of the global algorithms, the Otsu method was chosen both for its accuracy as well as for its popularity and success being utilized in several pieces of literature [97][125][82]. The

concept behind the Otsu method is to minimize within-class variances of background and foreground pixels, akin to maximizing the means of the two classes of pixels [135][125].

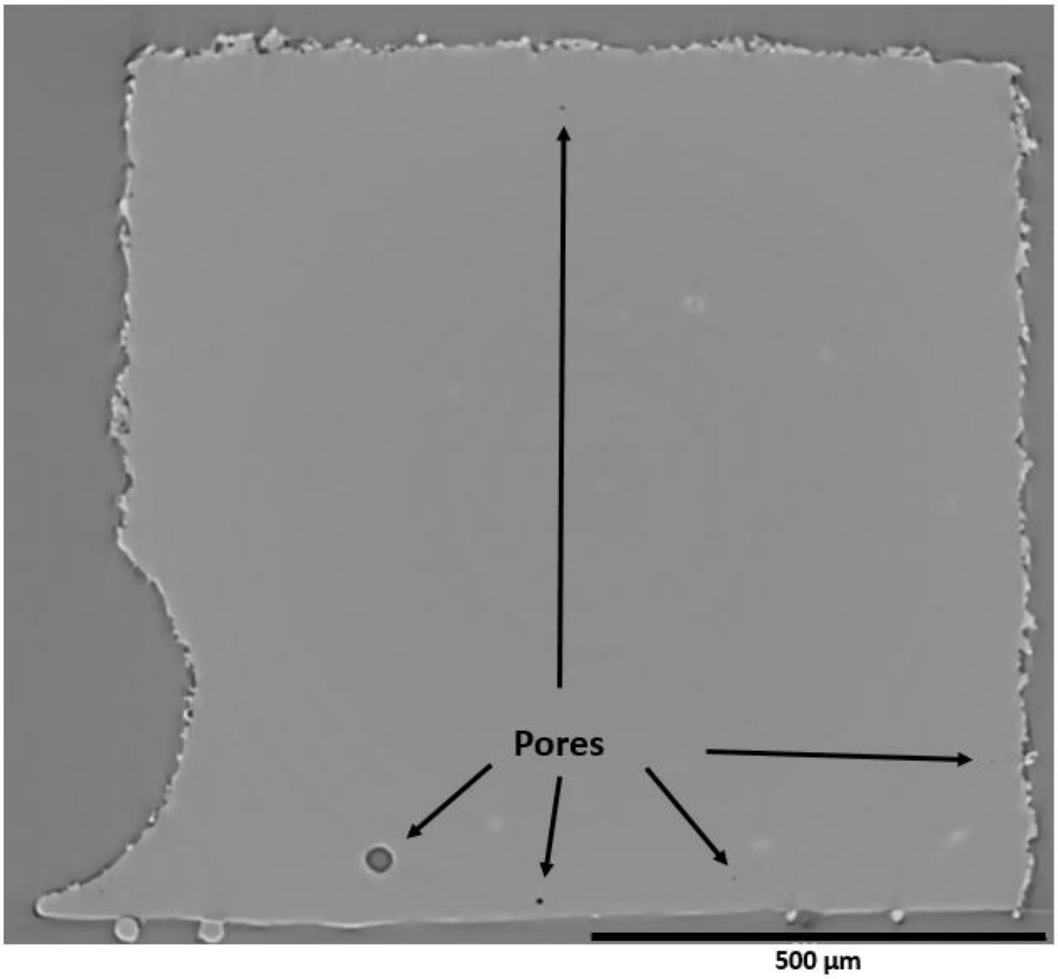

Figure 37: HR IN718 2D tomograph slice

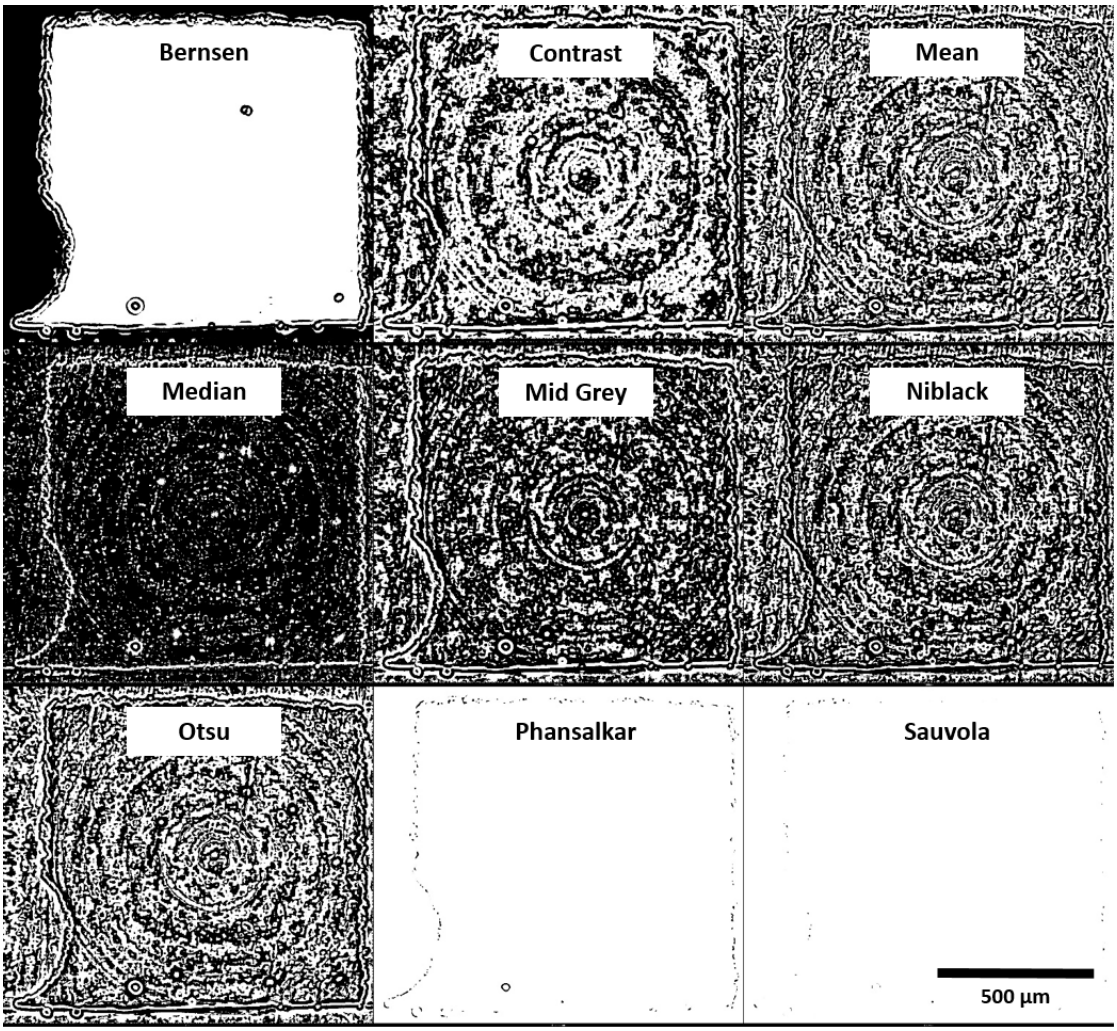

Figure 38: Local thresholding algorithm options for HR IN718 data

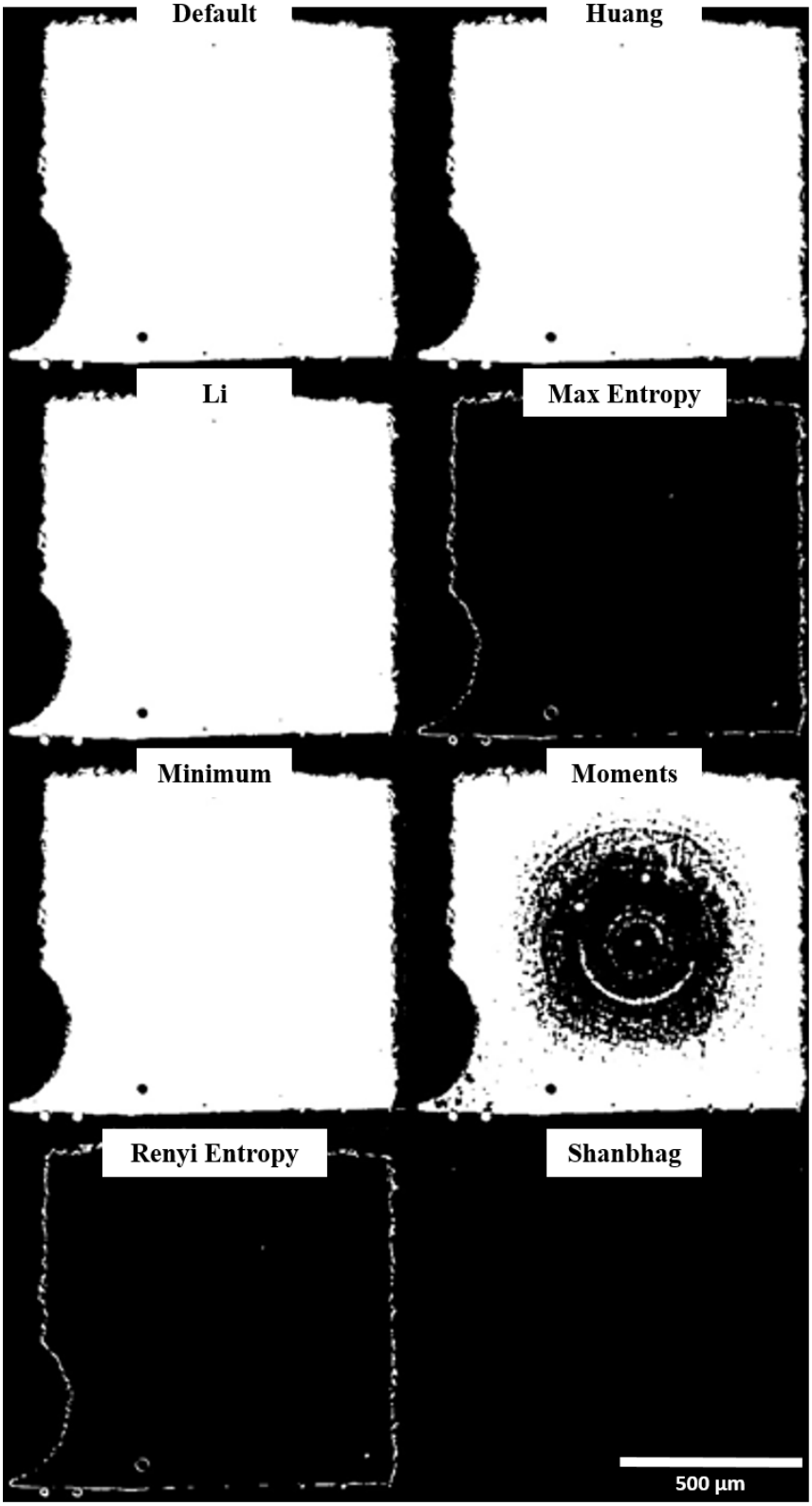

Figure 39: Global thresholding algorithm options for HR IN718 data (1 of 2)

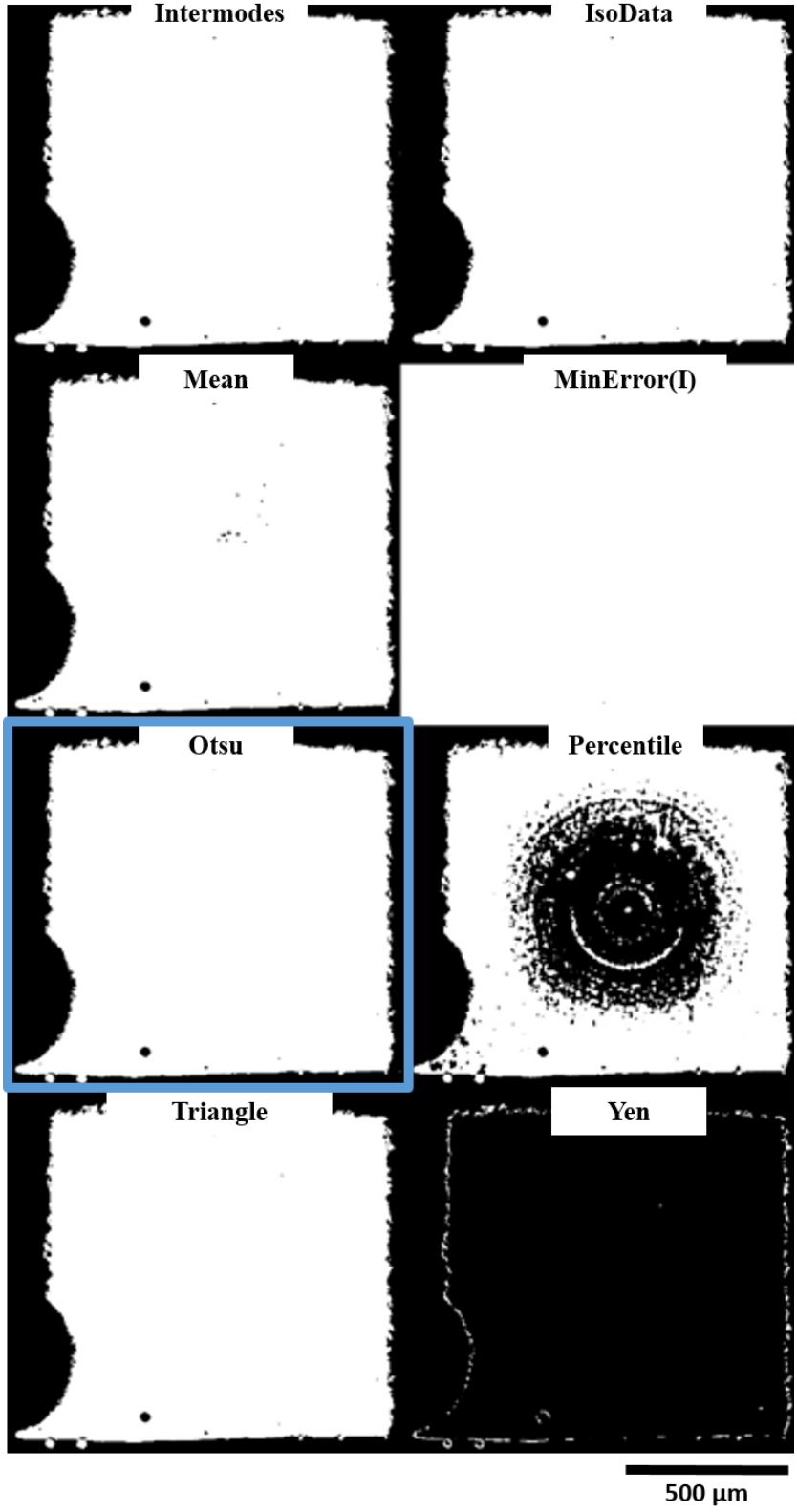

Figure 40: Global thresholding algorithm options for HR IN718 data (2 of 2 – chosen algorithm outlined in blue)

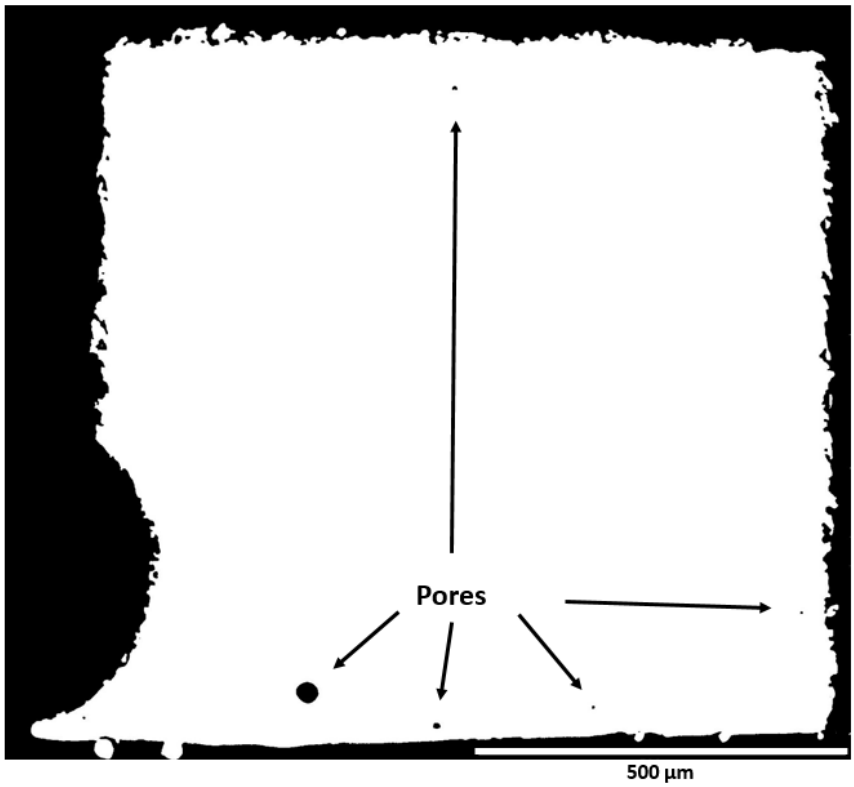

Figure 41: Global Otsu method threshold of HR IN718 2D tomograph slice

The choice of using global vs. local thresholding comes down to several governing factors. Local thresholding can usually produce more representative binarization of an image to its actual features; however, it is not always the best method to utilize. Local thresholding has a higher computational time as it must run its algorithm multiple times based upon how large or small the user determines the size of the local spatial areas to survey. Furthermore, based on the size of the survey area, noise can become a larger detriment to accurate binarization than with global methods as smaller variations in pixel intensities are more likely to end up on opposite ends of the binarization spectrum. However, overall, local thresholding seems to more accurate in depicting image features than global methods and a comparison of the two is suggested to be performed before

choosing a method to pursue. In the user's experience, images with less noise can be accurately thresholded with a global method and those with more noise may necessitate a local method so long as the survey area is accurately determined.

The local algorithm was chosen over global methods for the LR reconstructions because they were more affected by beam hardening and noise grayscale variations across specific images as well as throughout the entire volume of the image stack. While a global method might accurately segment one or several slices, it was more prone to inaccuracy throughout the entire slice. Since changing the global threshold per slice was impractical, the local Phansalkar method was chosen because of its ability to adapt to different slice grayscale variations as well as those within a slice. Furthermore, the Phansalkar method is uniquely created to deal with low contrast images, which was characteristic of the reconstructions in the LR data set. As such, the Phansalkar method was the highest performing algorithm out of all the available local methods, as observed in Figure 36, as well as across all LR specimens.

For the HR data, a global method, Otsu, was chosen over local methods, including its comparable local version, as well as other global algorithms. The local methods had a few algorithms approach accurate segmentations, but none was able to adequately threshold the image slice to capture the porosity features. Noticing the visible ring-like elements in the segmentations of Figure 38, it can be implied that ring artifacts present in the reconstruction image caused issues for several of the local algorithms, possibly due to the local contrast in those pixels compared to the surrounding "non-ring" pixels forcing them to be grouped together through local processes. Contrastingly, the global methods performed much better with several being able to provide accurate segmentations. The

Otsu method was chosen due to both its accuracy and its pedigree being used in many published CT investigations. A possible reason for the greater accuracy of the Otsu method, as compared to some of the other global methods, is that it utilizes second order moments in determining inter-class variances, while other methods use only zeroth and first order (i.e. Moments and Li). By using the second order moments, which are calculated by a scaling factor quadratic incorporating the local gray value mean, it can allow for moment variations to be less pronounced, leading to the ability to overcome influences of the ring pixels. The Moments and Percentile algorithms of the global methods, though different in calculation of the threshold value, were both affected by ring artifacts in the image, but overall, most of the global methods were able to withstand those image defects. The Moments algorithm aims to preserve the image moments from grayscale to binarization, providing a possible reason for the presence of ring features in the binarized output as the image moments would capture those features. The MaxEntropy, RenyiEntropy, Yen, and Shanbhag methods, based off maximizing entropy (or minimizing differences in entropy) contained in the input and output images, were again affected by high contrast in the border of the material making the algorithm inaccurate in determining the background and foreground of interest. Nevertheless, owing to the totality of the survey area of the threshold selection, the global algorithms are not as susceptible to localized grayscale variations. Furthermore, because the HR data was less noisy and had less beam hardening effects than the LR data, there was not as much grayscale variation overall, allowing for use of a global method and a faster computational time per pixel.

As previously stated, thresholding and satisfactory segmentation are the most important steps to being able to obtain accurate quantitative feature data from an image

[110][93]. As the segmented binary image is the only input for the visualization and quantification software, the utmost care and quality control must be taken to reach an adequate thresholded result. Maskery et al. discussed the large effects that inaccurate thresholding can have on final pore quantitative characterization [93]. According to Maskery et al., altering the threshold value for image segmentation by only ±5% was shown to alter the mean value of porosity for their full image stack by ±10% and the median pore area by -24% / +14% [93]. They attributed the fluctuations in results to the inclusion or exclusion of a large number of seemingly small pores that were present or not in the segmented image, based on the specific threshold value alteration [93]. Quality control in previous steps, from data acquisition to reconstruction to image processing, will allow for easier segmentation and more accurate final quantification results and should be completed with care.

A deeper analysis of the effectiveness of the different thresholding algorithms, with relation back to the characteristics of the input gray image and the variations in the algorithms themselves is recommended. While beyond the scope of the current research goals, a study of this nature may lead to a greater understanding of which methods are most effective, based upon the characteristics of the input image, as well as the possible creation of better performing algorithms that encompass a wide range of tomographic image inputs.

3.2.4 Visualization and Quantification

Visualization is the process of 3D computer model generation from 2D image stacks that allows for qualitative characterization of the subject that may be more difficult to observe in a 2D format. Quantification, for the purpose of this research, is the numerical

characterization of porosity within the samples. As previously mentioned, both visualization and quantification were performed in Avizo 9.2.0.

Avizo was previously described relative to its image processing tools; however, it is primarily a software designed for the visualization and quantification of 3D data sets [148]. Shown in Figure 42, users are able to inspect and manipulate data within a graphical user interface (GUI) or in a "Tree View" format where data can be connected together and controlled by various parameters creating a visual processing network that is eventually output and displayed as a 3D model [148]. Avizo is one of the most popular commercial visualization programs for scientific visualization and has been utilized for CT microstructural characterization by several authors previously [62][149][96][64][82].

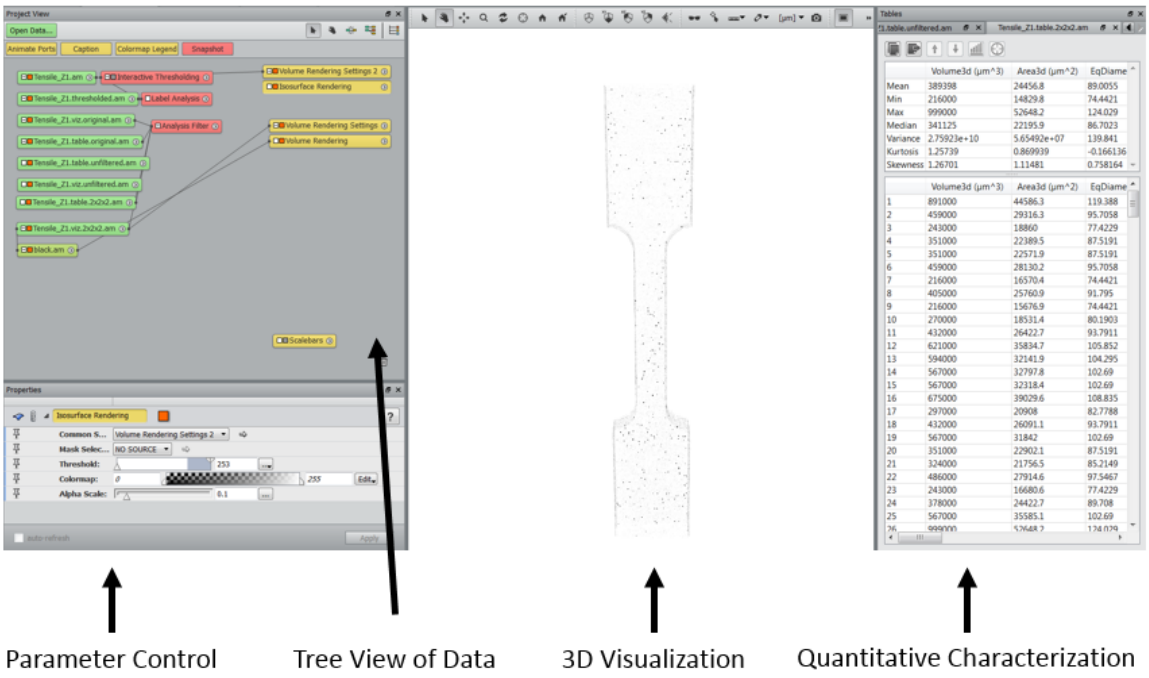

Figure 42: Avizo graphical user interface

The workflow for visualization and quantification employed for this thesis was built off workflows utilized for similar applications found in literature but was also uniquely adapted by the user for the specific datasets. Maire and Withers discussed a general framework for visualization and quantification, harping on the advantages of analyzing a full volume, either as a 3D image or as a stack of 2D images (as done in the current work), to reduce errors caused by a smaller sample size [119]. Chen discussed the specifics of exact workflows in Avizo to quantify characteristics such as porosity volume fraction for fuel cell electrodes [149]. While suggestions about an optimal workflow in Avizo gleamed from literature review were beneficial, overall, specific details were limited. As such, much trial-and-error discovery of the optimal process for an Avizo workflow was experienced in this research.

The process for visualization employed by the author is as follows. As discussed previously, it was decided best to utilize ImageJ for segmentation because of the intuitive GUI and plethora of thresholding options available. Shown in Figure 43a, the stack of thresholded images for a specific specimen was uploaded to Avizo's memory. Next, as shown in Figure 43b, the binary image was re-thresholded within Avizo to transform the image to an Avizo-specific format that is necessary for quantification. Since the image is binary but still has an intensity range of 0 to 255, a threshold of 0 to 1 was used for the segmentation of porosity, as shown in Figure 43b. Conversely, a threshold of 254 to 255 was used for the segmentation of the solid material, displayed in Figure 43c. Finally, the porosity was visualized in 3D by projecting its segmentation stack onto the original ImageJ-thresholded input stack. These processes were all performed in batch format for

the entire image stack. A 2D visualization slice is shown in Figure 43d for comparison purposes.

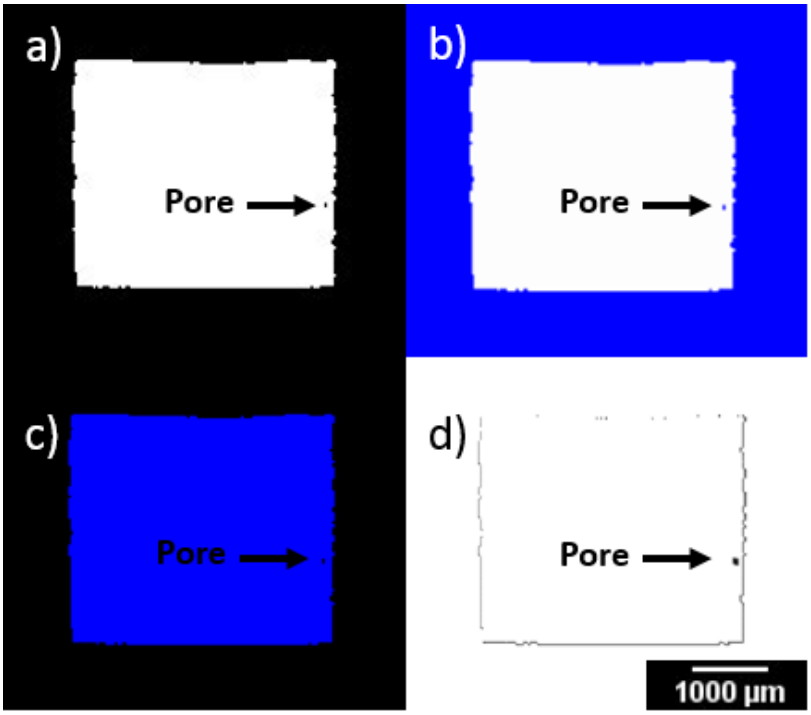

Figure 43: Process from initial segmented image to visualization starting from a) segmented binary LR Ti64 2D tomograph slice (ImageJ) to b) porosity threshold (Avizo) to c) material threshold (Avizo) to d) 2D slice visualization (Avizo)

Quantification was performed on the data after re-segmentation within Avizo. To quantify the porosity, Avizo has a tool called "Label Analysis" that can be applied to a segmented image to obtain different numerical data. A list of different characteristics are preloaded in Avizo to quantify data and there is also the ability to create new characteristics by defining an equation made up of the preloaded qualities. Characteristics chosen to be quantified were porosity volume, equivalent spherical diameter, Width3d, BaryCenter (for x, y, z axes) and BoundingBox (for x, y, z axes). Porosity volume was obtained in cubic micrometers (defined by the user by inputting 0.65 µm/voxel length scale), equivalent

spherical diameter calculates what the diameter of a given pore would be if its morphology was spherical, Width3d is a measurement of the smallest distance between two free surfaces of a pore (as if measuring with calipers), BaryCenter is the location of a pore's center of gravity, and BoundingBox is the measurement of the largest distance between free surfaces of a pore along a specified axis. Porosity volume and equivalent spherical diameter are characteristics to be reported for this thesis, BaryCenter was used for determining the proximity of pores to each other, and Width3d and BoundingBox were both used to filter the data by eliminating porosity within defined ranges of those two characteristics. Specifically, porosity was filtered by eliminating pores that were not at least 2 voxels in length in the x, y, and z axes. To see how population trends would change across different filters, the data was also filtered 1) at 5 voxels in length in all three dimensions, 2) at 5 voxels in length in x and y axes while only 3 voxels in length in the z axis, and 3) by requiring an equivalent spherical diameter of at least 10 μm. Reasoning for applying these filters is discussed in a later section of this thesis.

One of the most difficult parts of completing this research was dealing with the large datasets associated with synchrotron-based micro-tomography. With each specimen's raw CT file totaling about 16GB of data, choosing the most efficient methods to save on computational time was required. In Avizo, visualization of data requires 2-4 times as much system memory as the size of the file itself [123]. There are options in Avizo to process data from a hard drive directly, but computational time is greatly increased with this method. As such, it is recommended to upgrade system memory as required. However, in the user's experience, the most critical piece of hardware to a streamlined workflow is the GPU. When running visualizations of large datasets, Avizo

tends to crash if the GPU becomes overloaded. This occurrence happened many times in this research, compounding the time to process a dataset. Upgrading the GPU to required specifications is highly recommended.

Filtering porosity data by size, to improve confidence in results, has been suggested in relevant literature and employed in this research. Due to the uncertainty of analysis software in determining whether porosity-like features consisting of only a few voxels are actually pores, or caused by some other source (dust on detector, noise, etc.), filtering must be applied to remove that doubt [82]. The analysis software operates by quantifying images from a segmentation, and since noise, dust, or other non-porosity elements can also be segmented into looking like pores, it is difficult to determine the difference. For example, a single voxel pore should not be considered for quantification because it is impossible to overlook the potential that it is another feature being segmented [82]. This line of thinking implies that if a feature consists of several voxels (defined by a user-controlled cutoff) it is more likely to be an actual pore. As such, a 2x2x2 (8 face-connected) voxel cutoff was applied to the data for pore size distributions and volume fraction calculations. This filter equates to a 60 μm minimum dimension (x, y, z axes) for pores reported in the LR dataset and a 1.3 μm minimum dimension (x, y, z axes) for pores reported in the HR dataset. Furthermore, especially for morphological considerations, an even greater cutoff filter is recommended because if a pore is too small it is difficult to accurately represent its shape (i.e. a one voxel pore will always appear cubic) [82]. Thus, a 5x5x5 (125 face-connected) voxel cutoff was also applied to the data, as suggested by Tammas-Williams et al., and a sensitivity study was conducted to determine if the quantification of porosity content was significantly affected [82]. This filter was only

applied to the HR dataset, because the smaller pixel size is more susceptible to dust and non-porosity elements, and equates to a 3.25 μm minimum dimension (x, y, z axes) for reportable pores. Lastly, the filter of a 10 μm equivalent spherical diameter was used for purposes of visualization (on HR data only because of the larger amount of pores detected compared to LR data) to more clearly examine spatial trends and distributions of larger pores that have a larger influence on mechanical properties, as previously discussed.

Knowledge of the proximity of pores to one another is an important characteristic of the material to quantify for implications on mechanical performance, as previously discussed. Taking the spatial distribution output from the Avizo analysis, the distance from one pore to another was calculated and reported. To do this, pores were first idealized as spherical using the measurement of their equivalent spherical diameter. The distance from a pore to its nearest pore was then calculated from the edge of the sphere to the edge of its closest neighbor, as shown in Figure 44. No duplicate distances were reported, meaning only the nearest neighbor, in three dimensions, was selected. Probability distribution functions (PDFs) were then plotted to show the distribution of clustering of the porosity.

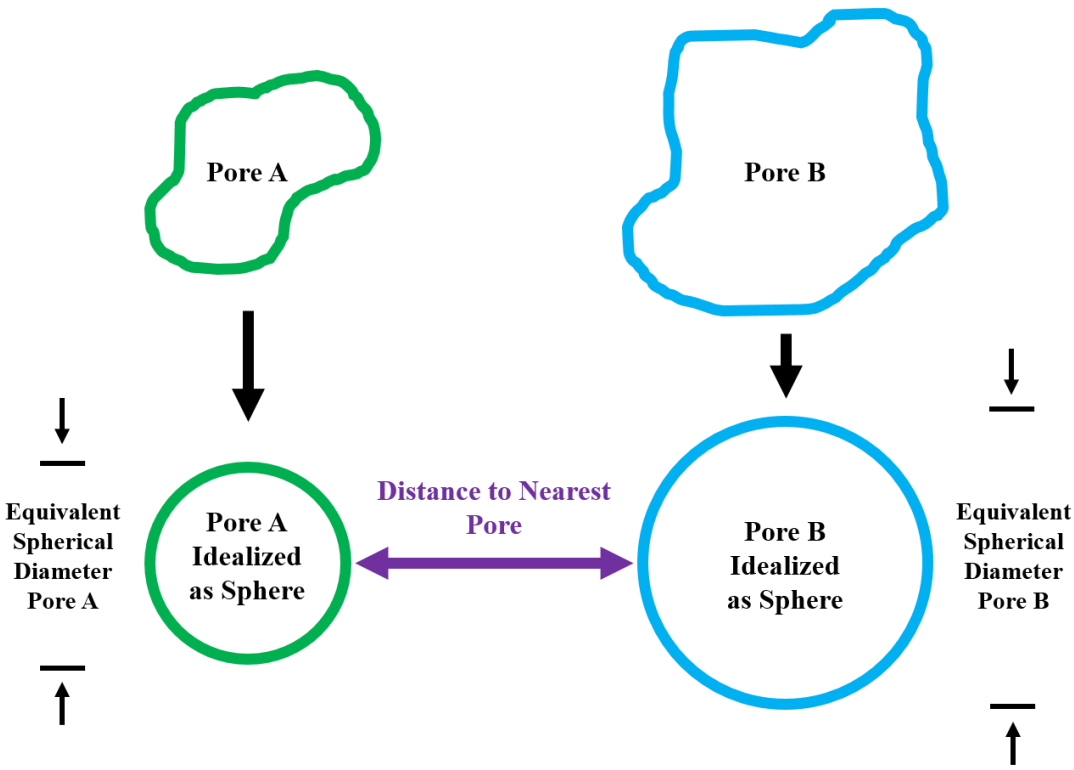

Figure 44: Diagram of pore proximity analysis

CHAPTER 4. RESULTS

This section covers the porosity characterization results for all specimens analyzed. Results will be reported for the LR dataset first and the HR dataset second. Quantitative data on pore count and volume fraction will be presented in tabular format and qualitative observations of pore spatial distribution will be presented through 3D model visualizations. Volume fraction was calculated by summing the total volume of pores identified in the specimen by the specimen material volume, as calculated in Avizo by taking the opposite binary intensity of the porosity and analyzing through the same process. Though having slight variations in material volume, due to variations in fabrication, in general the volume of the specimens were on the order of 1*10^12, 2*10^13, and 1*10^9 μm^3 for the LR dog-bone, LR bulk, and HR specimens, respectively. Porosity size distributions will be presented, in graphical format, for the HR dataset only since the LR dataset lacked the quantity of observable porosity necessary to show meaningful distributions. A pore proximity study for the HR dataset will also be presented to show the propensity for pores to be close to their neighbors. Characterization of the porosity will be presented in the current section with comparisons made between the datasets and trends identified. Comparisons of interest that will be discussed are between materials, dog-bone vs. bulk (LR data only), SR vs. PP, horizontal-built vs. vertical-built (LR data only), near-surface vs. in-bulk (HR data only), and LR vs. HR. A thorough discussion and analysis of the porosity, giving possible causes and broader implications of the results observed, will be covered in the next section.

4.1 LR Data

Table 8 displays the complete list of LR specimens characterized for this research, along with their differentiating qualities, and quantifies the amount of porosity within them. As a note, results are rounded to five decimal places arbitrarily. First looking at the results as a whole, porosity content in the specimens was low overall, with the lowest density for any of the LR specimens being $1.22*10^{-2}$ % in LR-T5. In contrast, the highest density was effectively 100% (rounded to five decimal places) in all of the bulk specimens.

Table 8: Low resolution (30 μm) porosity quantification results table using a 2x2x2 voxel minimum pore size filter

Specimen ID	Resolution [μm]	Specimen Type	Build Direction	Processing State	Pore Count	Porosity Volume Fraction [%]	Mean Spherical Equivalent Diameter [μm]
LR-I1	30	Dog-bone	Horizontal	SR	3	$7.00*10^{-5}$	84.5
LR-I2	30	Dog-bone	Vertical	SR	56	$1.27*10^{-3}$	81.3
LR-I3	30	Dog-bone	Vertical	PP	31	$6.10*10^{-4}$	78.1
LR-I4	30	Bulk	Horizontal	SR	0	$0.00*10^{0}$	N/A
LR-I5	30	Bulk	Vertical	SR*	1	$0.00*10^{0}$	77.4
LR-T1	30	Dog-bone	Horizontal	SR	28	$1.11*10^{-3}$	88.0
LR-T2	30	Dog-bone	Horizontal	SR	35	$1.11*10^{-3}$	83.9
LR-T3	30	Dog-bone	Horizontal	PP	30	$1.03*10^{-3}$	86.2
LR-T4	30	Dog-bone	Horizontal	PP	26	$8.30*10^{-4}$	83.9
LR-T5	30	Dog-bone	Vertical	SR	289	$1.22*10^{-2}$	87.2
LR-T6	30	Dog-bone	Vertical	SR	312	$1.13*10^{-2}$	85.5
LR-T7	30	Dog-bone	Vertical	PP	251	$9.71*10^{-3}$	87.1
LR-T8	30	Bulk	Horizontal	SR	11	$0.00*10^{0}$	92.0
LR-T9	30	Bulk	Horizontal	PP	2	$0.00*10^{0}$	83.1
LR-T10	30	Bulk	Vertical	PP	41	$0.00*10^{0}$	83.3
*uncertainty in data labelling – may be 3C/PP							

Focusing on the differences between materials, Table 8 shows that Ti64 had a higher level of porosity overall. The mean porosity volume fraction for Ti64 dog-bone specimens was $3.70*10^{-3}$ %, compared to $3.9*10^{-4}$ % for IN718 specimens. Specifically, it was not just the volume fraction of porosity that was higher in Ti64 (as that could be a result of larger pores forming in that material and not necessarily a larger number of pores), but there were also more individual pores that formed. The mean pore count for Ti64 dog-bone specimens was 139 as opposed to 30 for IN718. Observing the mean equivalent spherical diameter of porosity across the LR dataset also confirms that the pore size was in the same magnitude for all LR specimens.

Looking at comparisons amongst specimens of the same material there are clear trends. First off for both materials, as mentioned earlier, the dog-bone specimens clearly exhibit a higher level of porosity than the bulk specimens. In the IN718 bulk specimens porosity is virtually nonexistent, with one pore observed between two bulk specimens. Similarly for Ti64, some pores were observed, 11 and 2 for the two horizontal-built bulk specimens and up to 41 for the vertical-built specimen, respectively, but they constituted an insignificant volume of porosity. An interesting trend from the available data is that post-processed specimens show no clear difference in porosity levels than their solely stress-relieved counterparts. Though trends previously noted are observed in the characterization results, the most glaring finding is the apparent tendency for more pores to be present in vertical-built specimens than in horizontal-built ones. Strongly noticeable in the dog-bone specimens for both IN718 and Ti64, there is an order of magnitude higher quantity of pores in vertical-built specimens, resulting in a larger volume fraction for those samples overall. However, the size of the pores in the vertical-built specimens does not

seem to significantly increase compared to vertical-built specimens, as the mean spherical equivalent diameters are similar between the two datasets. Overall, quantification of porosity in the LR samples has exhibited interesting finds, but it is important to note that trends observed on the differences of dog-bone vs. bulk and SR vs. PP specimens are based off a limited sample size and more research is needed to fully conclude what has initially been observed in the current work.

Though quantification is necessary to generate an optimally useful evaluation of porosity in these materials, 3D visualizations are also desirable to be able to qualitatively observe spatial trends in the specimens. The analyzed LR IN718 dog-bone samples are shown in Figure 45. The horizontal-built sample, LR-I1, with its negligible porosity is contrasted with the vertical-built samples, LR-I2 and LR-I3, which have much higher porosity content. Figure 45a provides a look at the overall porosity in the specimen while Figure 45b shows the spatial distribution of the porosity between the horizontal-built (LR-I1) and vertical-built (LR-I2, I3) specimens. As previously noted, samples LR-I2 and LR-I3 exhibit a higher level of porosity but in Figure 45b it is seen that their pores are congregated closer to the free surfaces of the specimen, a strong trend seen throughout all specimens in this research.

Figure 46 depicts the porosity content in the bulk LR IN718 specimens. As seen, there is virtually no observable porosity above the 60 μm filter threshold with only one pore detected in specimen LR-I5.

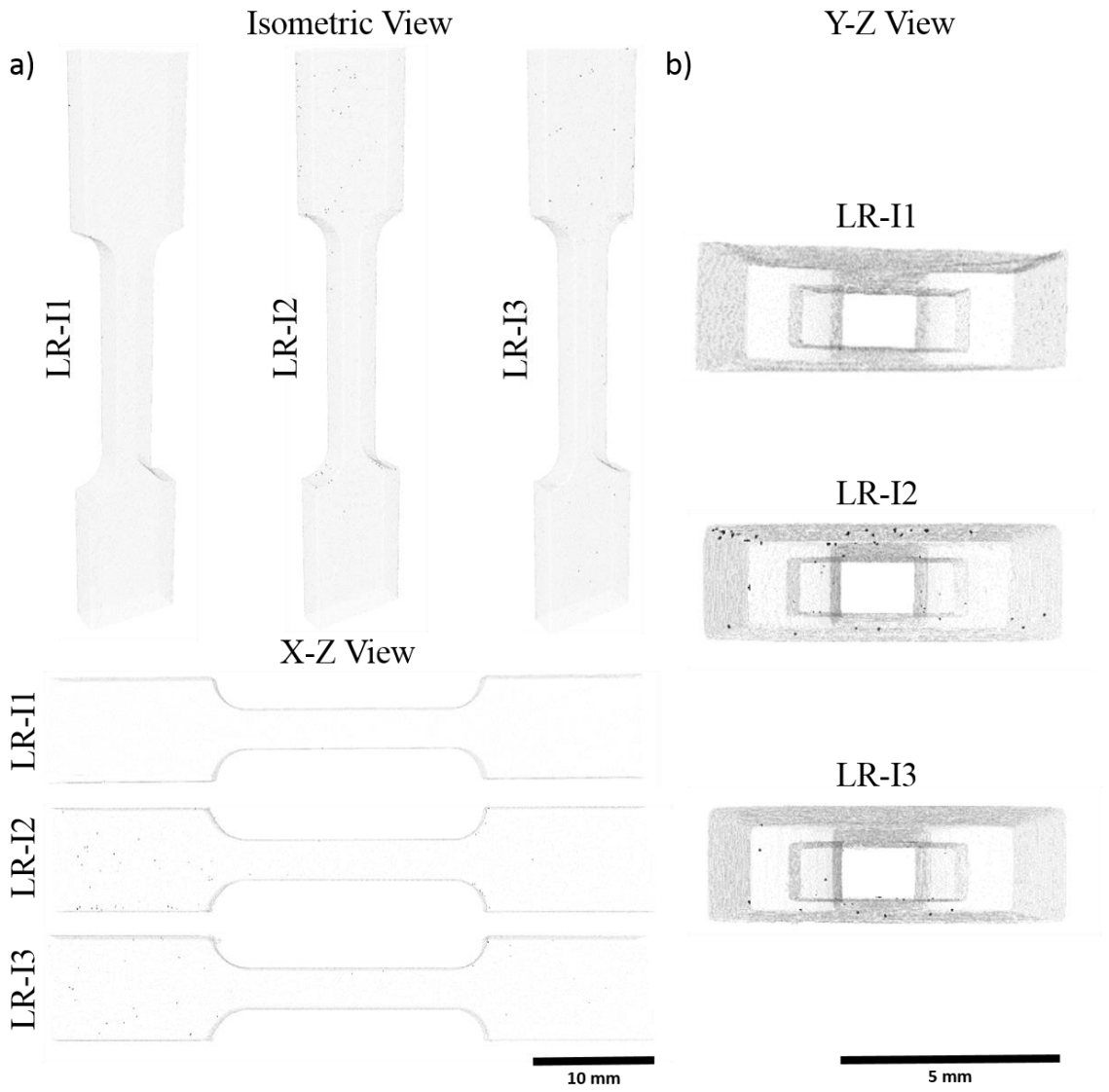

Figure 45: Porosity visualizations of LR IN718 dog-bone specimens in a) isometric, x-z views and b) y-z views

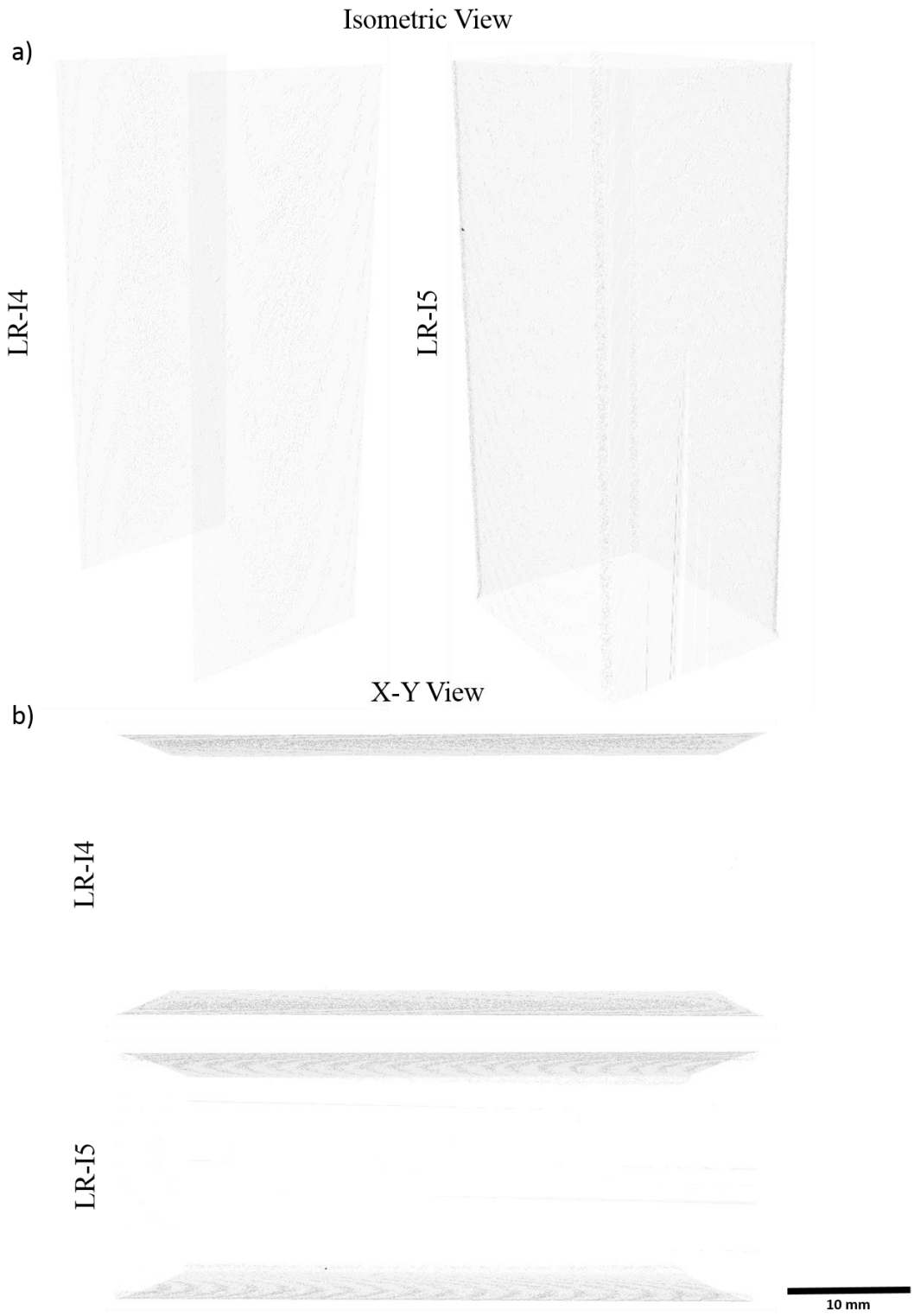

Figure 46: Porosity visualizations of LR IN718 bulk specimens in a) isometric and b) x-y views

As discussed earlier, the LR Ti64 specimens were found to have more porosity than their IN718 counterparts overall, which provides for an even clearer depiction of the spatial trends of the pores. Figure 47, Figure 48, and Figure 49 provide visualizations of the LR Ti64 porosity content. Again, it is clear to see the increase in porosity from horizontal to vertical-built dog-bones. Furthermore, porosity again seems to be located towards the free surfaces in all LR Ti64 specimens, with the trend most pronounced in the vertical-built dog-bones (Figure 48b) because of the larger porosity content. However, porosity trending toward the free surfaces is also observable in the horizontal-built dog-bones (X-Z view of Figure 47) and the bulk specimens as well (Figure 49).

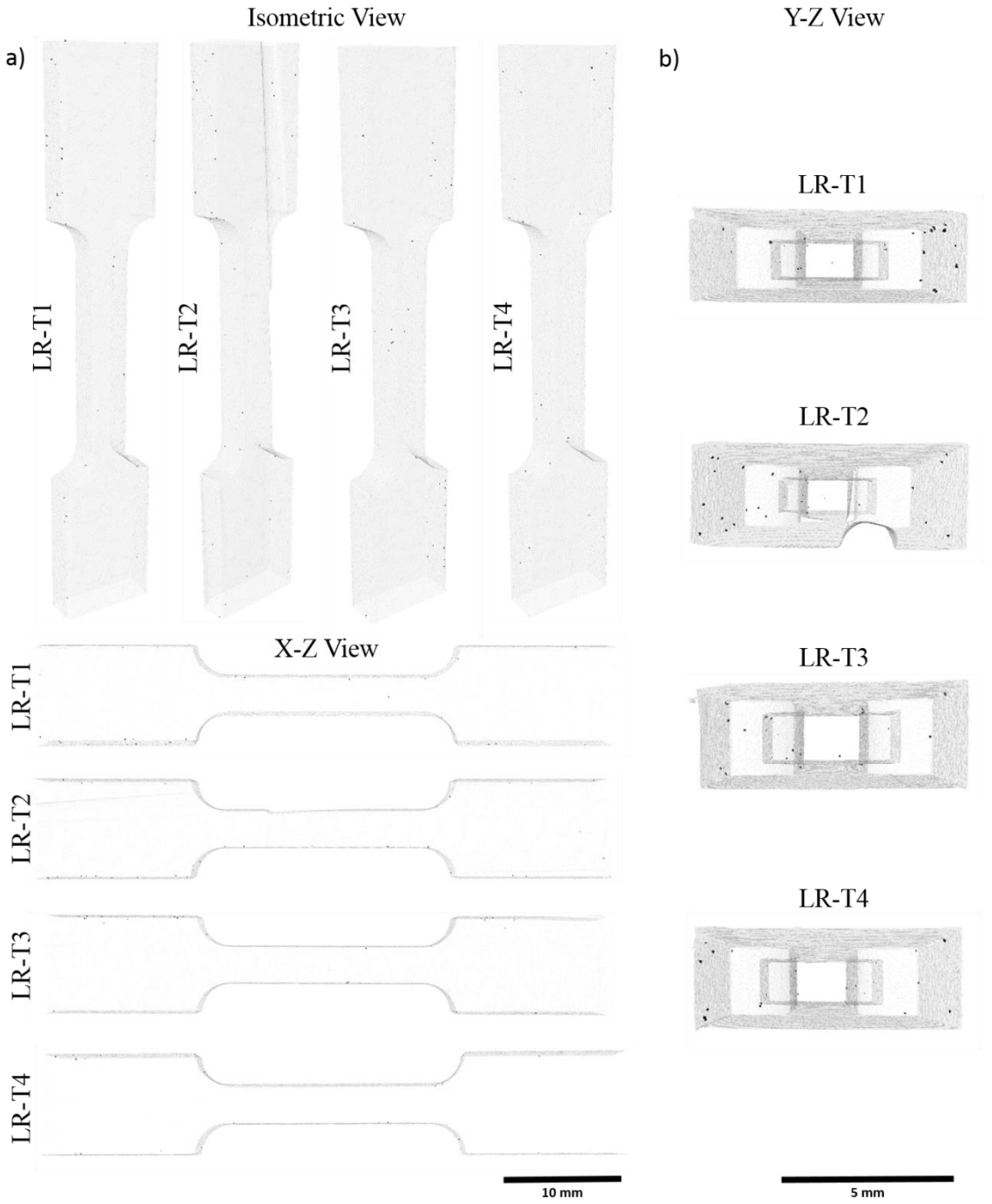

Figure 47: Porosity visualizations of LR Ti64 horizontal-built dog-bone specimens in a) isometric, x-z views and b) y-z views

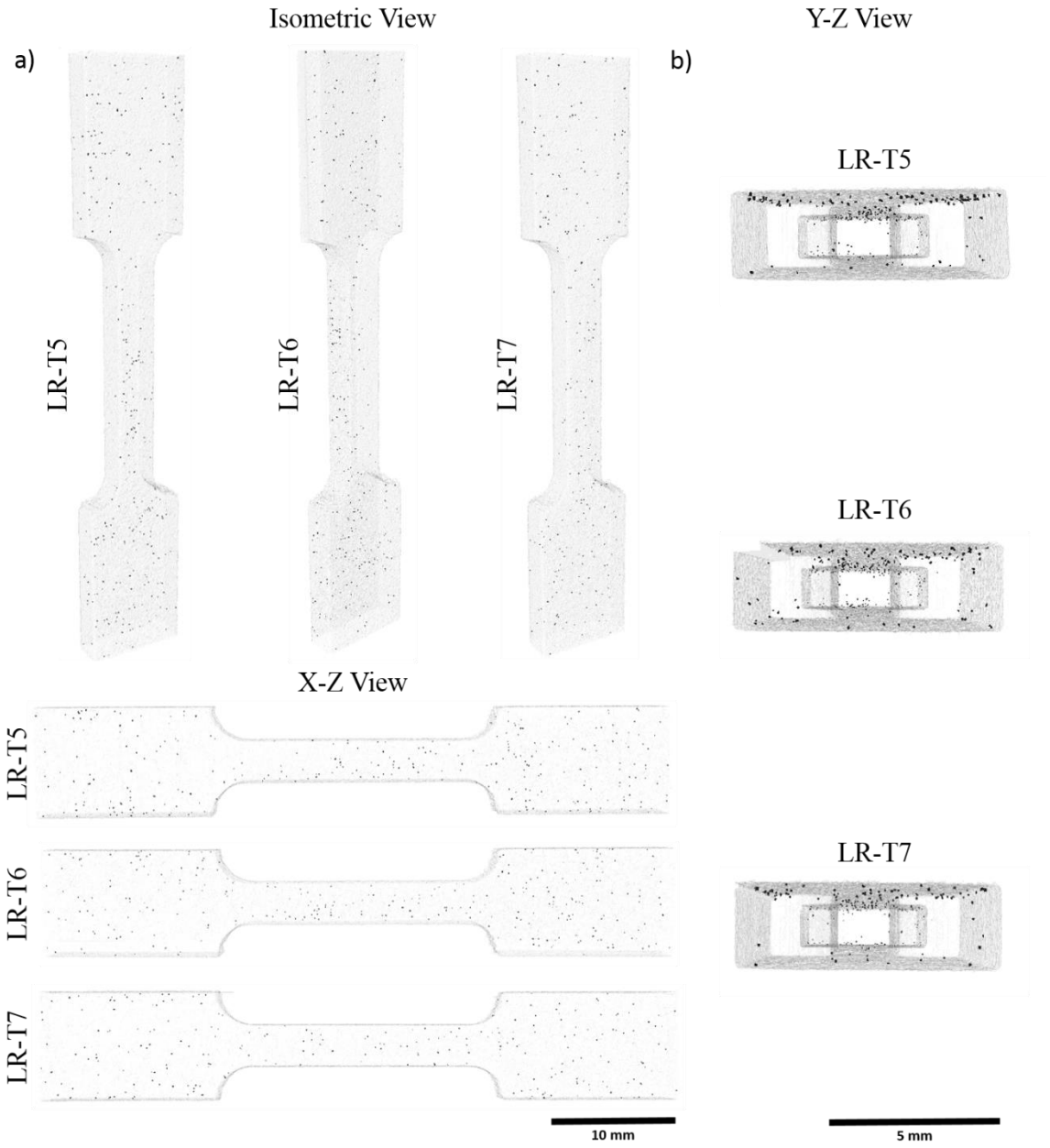

Figure 48: Porosity visualizations of LR Ti64 vertical-built dog-bone specimens in a) isometric, x-z views and b) y-z views

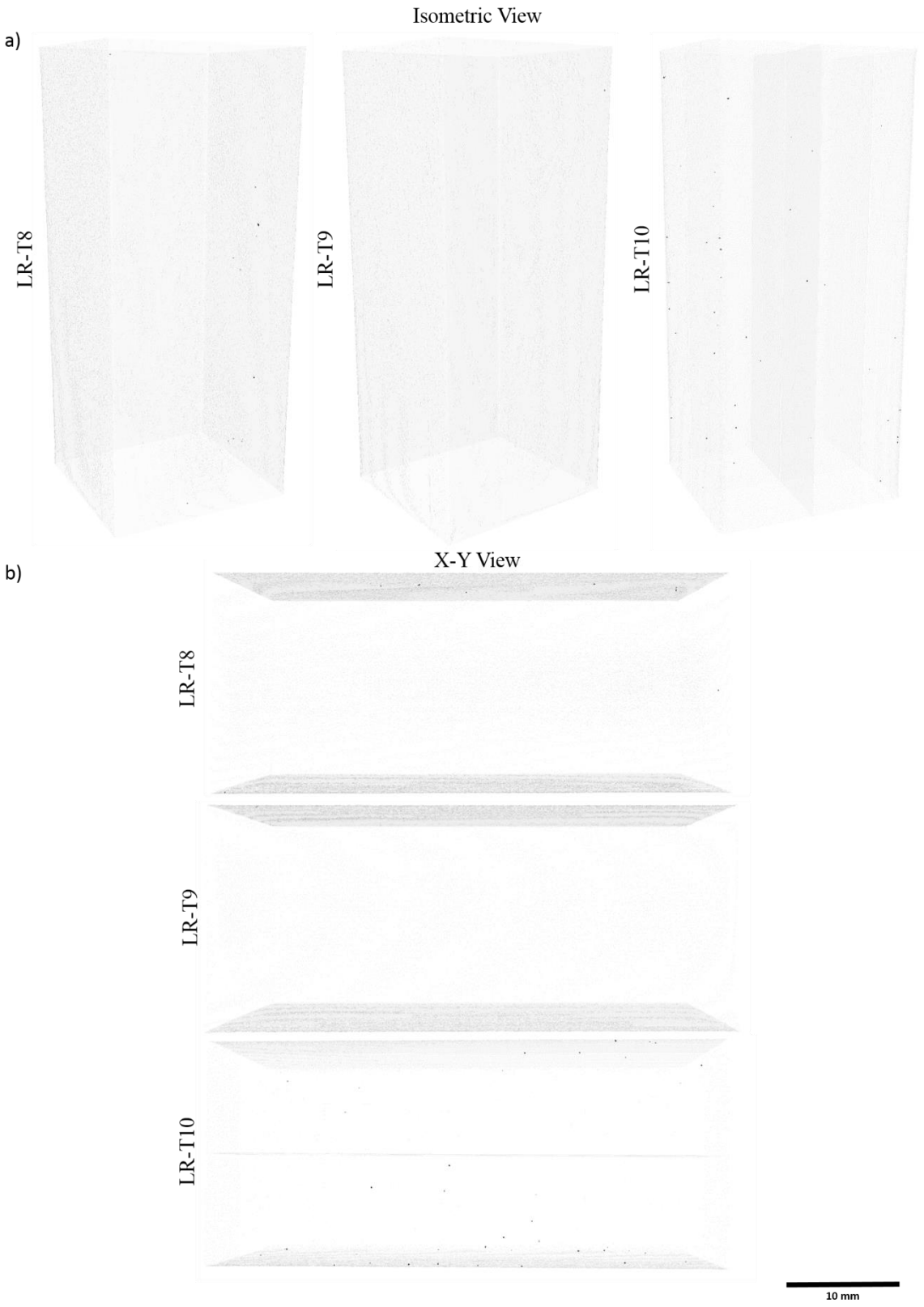

Figure 49: Porosity visualizations of LR Ti64 bulk specimens in a) isometric and b) x-y views

4.2 HR Data

HR data porosity results were able to offer clear trends observed between the different specimen types and spatially, within a specimen, as well. It is important to note again that HR data was only taken from samples cut out of bulk LR specimens, not dog-bones. Table 9 displays the quantified porosity content data for each HR sample. First, following the results of the LR data, porosity levels still remain relatively low in the HR dataset with the highest measured volume fraction totaling $1.25*10^{-1}$ % and $6.38*10^{-2}$ % for IN718 and Ti64, respectively. However, one of the most glaring observations is that there is a much larger amount of porosity detected in the HR data than in the LR data, as the pore counts are orders of magnitude higher. Though the increase in detected pores is large, when the HR porosity data for each specimen is filtered to only include pores that are 60 μm across or larger (the filter cut off for LR data), no such pores were able to be detected. This sanity check helps give more evidence to the accuracy of the results as the LR data only showed a few pores of this size and the HR specimens may not have been cut from the location of those pores. A further discussion of the observed increase in porosity content between resolutions utilized, sampling size, and sampling location is provided in the next chapter using a 3D porosity spatial simulation for reference. Furthermore, an interesting switch from the LR data is that the average pore count is higher for IN718 than Ti64, at 5544 and 3147, respectively. Similarly, the mean porosity volume fraction is also higher for IN718 at $7.30*10^{-2}$ % compared to $3.65*10^{-2}$ % for Ti64. Comparisons of the average mean spherical equivalent diameter between the materials also seems to favor IN718 samples.

Looking more specifically at differences in results within the two materials shows a strong and clear identification of higher porosity volume fraction for specimens sampled near the part surface rather than in-bulk. This trend holds true for near-surface vs. in-bulk comparisons within the same processing state as well as for each material. In fact, for each material, even near-surface post-processed specimens exhibit a higher volume of porosity than in-bulk stress-relieved ones. Specifically, however, the mean spherical equivalent diameter does decrease from stress-relieved to post-processed specimens that have the same proximity to the free surface.

Table 9: High resolution (0.65 μm) porosity quantification results using a 2x2x2 voxel minimum pore size filter

Specimen ID	Material	Resolution [μm]	Specimen Location	Build Direction	Processing State	Pore Count	Porosity Volume Fraction [%]	Mean Spherical Equivalent Diameter [μm]
HR-I1	IN718	0.65	Near-surface	Horizontal	SR	3929	$8.20*10^{-2}$	5.3
HR-I2	IN718	0.65	Near-surface	Horizontal	SR	4698	$1.25*10^{-1}$	5.2
HR-I3	IN718	0.65	In-bulk	Horizontal	SR	6073	$5.07*10^{-2}$	4.6
HR-I4	IN718	0.65	In-bulk	Horizontal	SR	5530	$4.40*10^{-2}$	4.5
HR-I5	IN718	0.65	Near-surface	Horizontal	PP	8933	$7.55*10^{-2}$	4.1
HR-I6	IN718	0.65	Near-surface	Horizontal	PP	5722	$7.89*10^{-2}$	4.3
HR-I7	IN718	0.65	In-bulk	Horizontal	PP	4645	$1.16*10^{-2}$	3.9
HR-I8	IN718	0.65	In-bulk	Horizontal	PP	4821	$1.25*10^{-2}$	3.9
HR-T1	Ti64	0.65	Near-surface	Horizontal	SR	2280	$4.84*10^{-2}$	4.5
HR-T2	Ti64	0.65	Near-surface	Horizontal	SR	2043	$3.64*10^{-2}$	4.7
HR-T3	Ti64	0.65	In-bulk	Horizontal	SR	3548	$2.25*10^{-2}$	4.2
HR-T4	Ti64	0.65	In-bulk	Horizontal	SR	3212	$2.31*10^{-2}$	4.2
HR-T5	Ti64	0.65	Near-surface	Horizontal	PP	2730	$6.38*10^{-2}$	4.5
HR-T6	Ti64	0.65	Near-surface	Horizontal	PP	2284	$3.90*10^{-2}$	4.6
HR-T7	Ti64	0.65	In-bulk	Horizontal	PP	4844	$3.39*10^{-2}$	3.8
HR-T8	Ti64	0.65	In-bulk	Horizontal	PP	4231	$2.48*10^{-2}$	3.9

As previously mentioned, a sensitivity study was conducted on the different minimum pore size filters applied to the data to help determine how many of the individual pores are only made up of a few voxels; and thus, more likely to be caused by process error than actual porosity when compared with pores made up of many voxels. Figure 50 displays the results of the study, which was conducted on combined porosity from HR-I1 and HR-I2 for IN718, and HR-T1 and HR-T2 for Ti64. The samples from each material

were combined for the study because they represent scan volumes taken at two different locations in the same sample, as depicted in Figure 22. Overall pore volume fraction does not decrease greatly through the different applied size filters (minimum 2x2x2, 3x3x3, 4x4x4, or 5x5x5 voxels) with a decrease of less than $1.00*10^{-2}$ % for IN718 and less than $3.00*10^{-2}$ % for Ti64. Contrastingly, pore count greatly decreases as filter size increases with a decrease of about half for IN718 and greater than half for Ti64. The large decrease in pore count without the corresponding significant decrease in porosity volume indicates a large portion of small pores (64 face-connected voxels or less) present in the results.

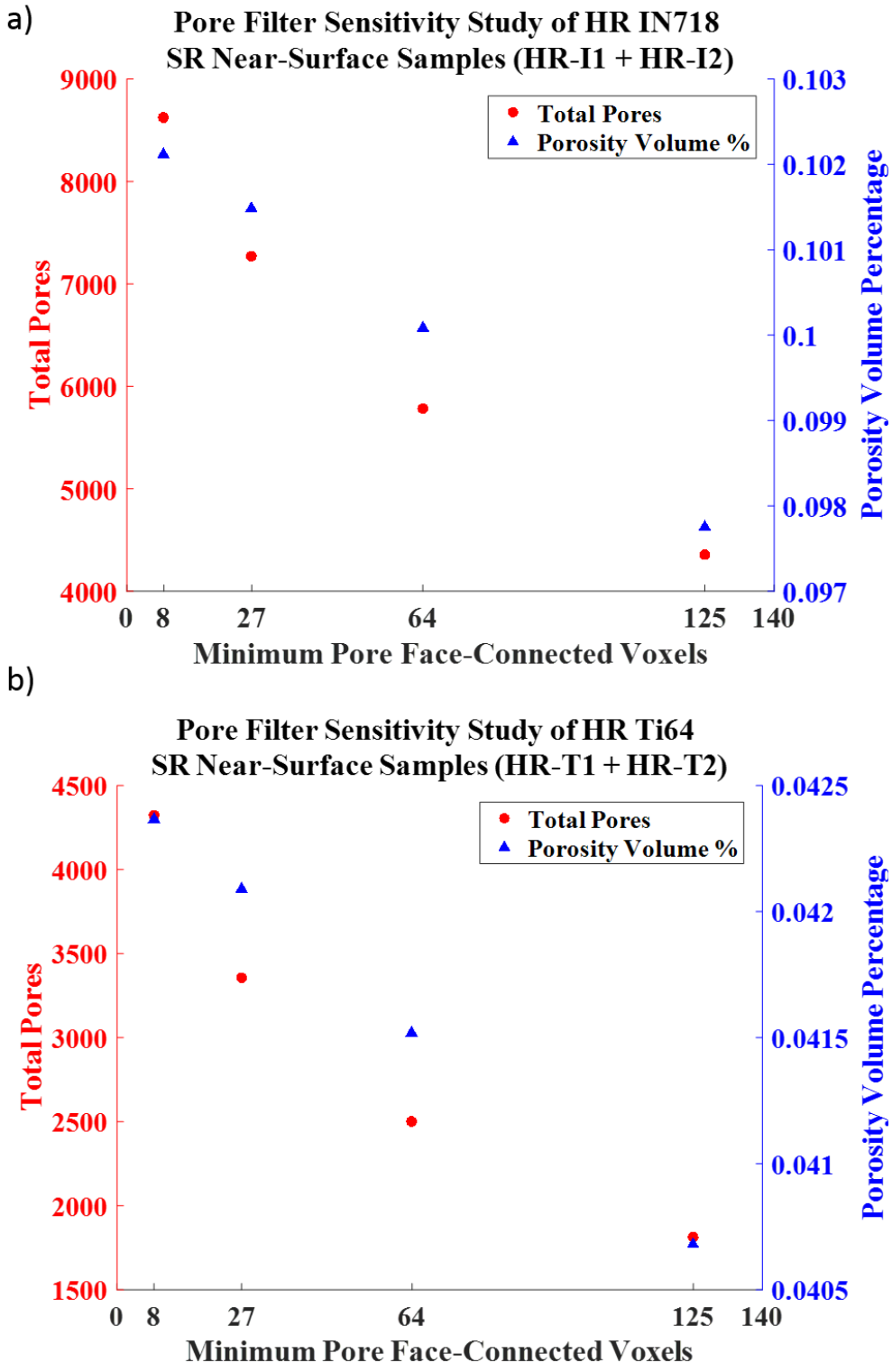

Figure 50: Sensitivity study of the decrease in porosity content as a function of an applied minimum pore size filter for all stress-relieved near-surface samples in both a) IN718 and b) Ti64

Supporting the results of the filter sensitivity study are observations made from comparing the cumulative distribution functions (CDFs) of equivalent spherical diameter for porosity of each specimen processing state for both materials. Figure 51 and Figure 52 display the CDF results for IN718 and Ti64, respectively. Amongst all specimen types in both materials the trailing tails of distributions decrease as filter size is increased. These tails represent the likelihood, and thus the presence, of smaller pores as a portion of overall porosity in the materials and confirm the findings of the sensitivity study.

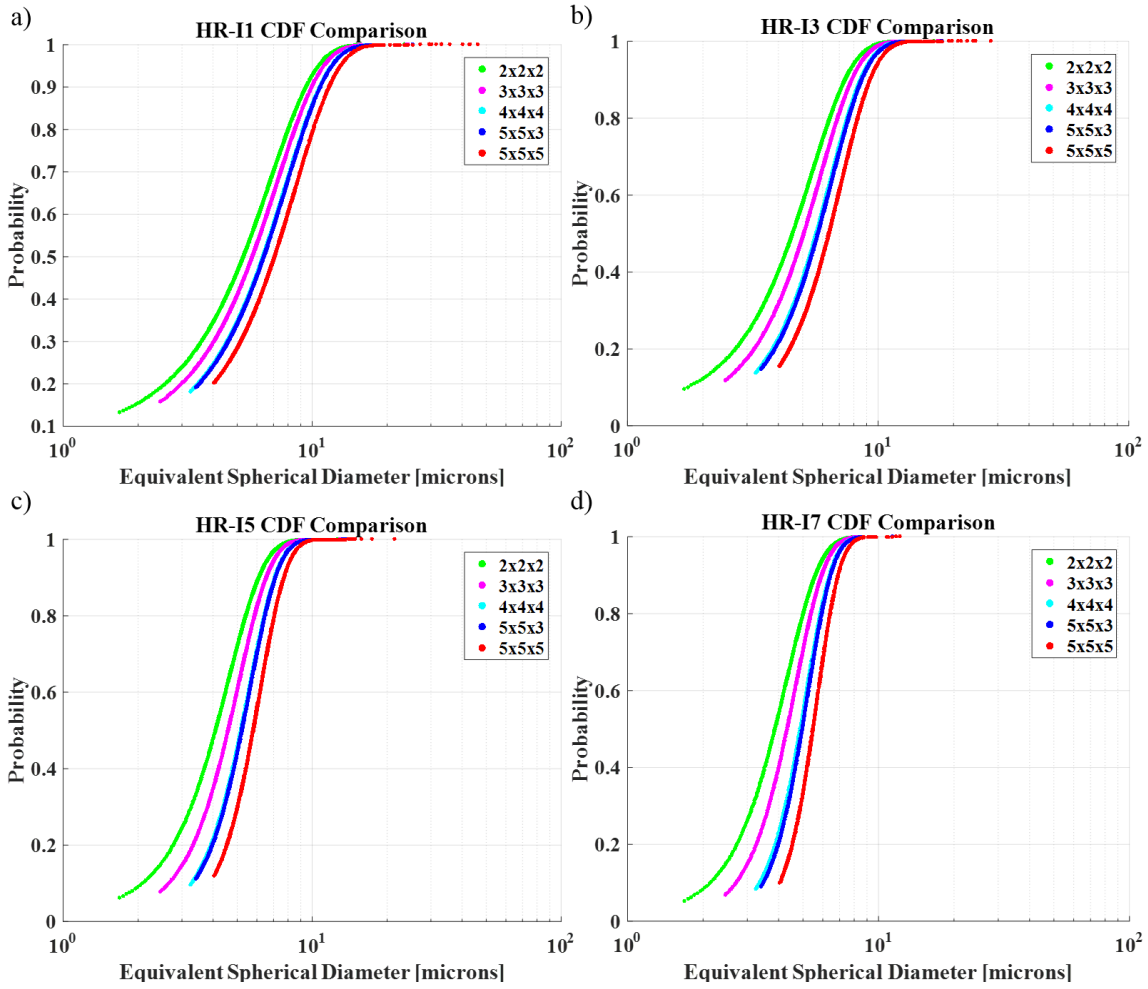

Figure 51: CDF of porosity size distribution comparing minimum pore size filters for IN718 a) near-surface, stress-relieved b) in-bulk, stress-relieved c) near-surface, post-processed and d) in-bulk, post-processed specimens

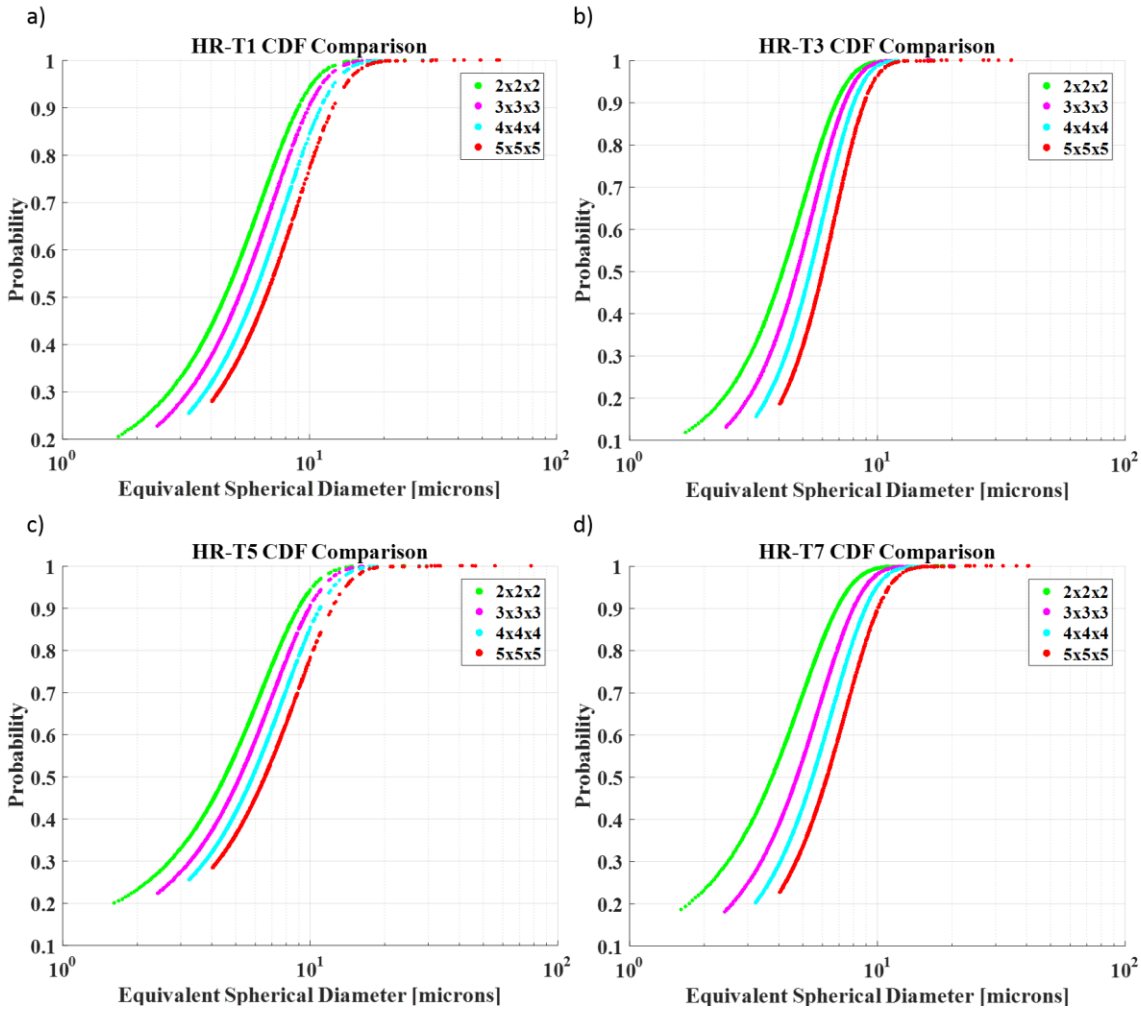

Figure 52: CDF of porosity size distribution comparing minimum pore size filters for Ti64 a) near-surface, stress-relieved b) in-bulk, stress-relieved c) near-surface, post-processed and d) in-bulk, post-processed specimens

Visualizations to accompany the sensitivity study and CDF comparisons are shown in Figure 53 and Figure 54 for both materials. Visualizations were developed for the detected porosity and show one example specimen for each material with no filter, a minimum 8 face-connected voxels filter, a minimum 125 face-connected voxels filter, and a minimum 10 μm equivalent spherical diameter filter. The unfiltered visualizations provide a good look at the total amount of porosity that can initially be detected and

progressing through the filters shows the existence of smaller pores that are removed as filter size increases. From these comparisons, it should also be noted that while many pores exist in the specimen, the porosity volume fraction is dominated by the presence of a smaller number of large pores in the specimens.

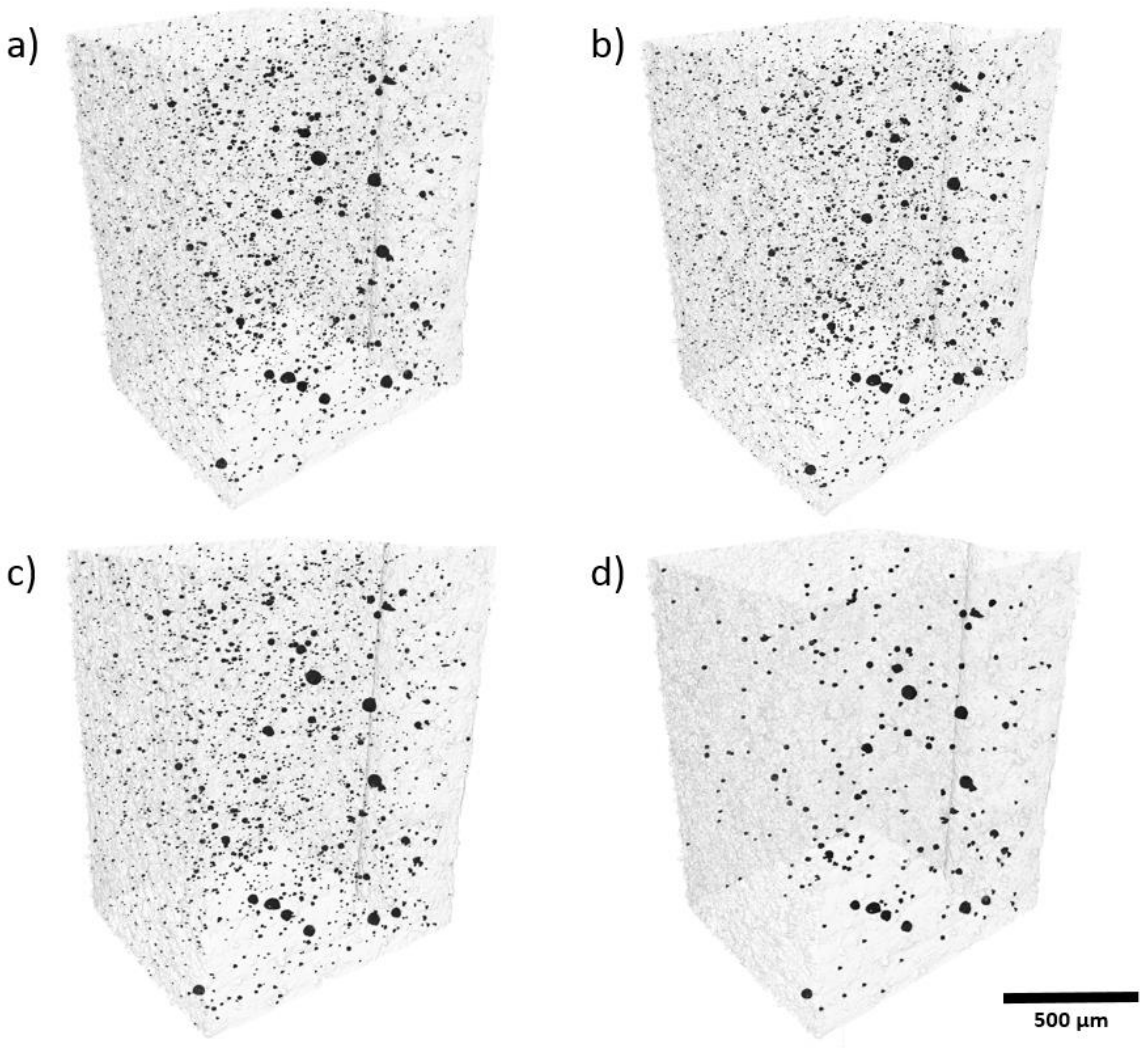

Figure 53: Visualizations of HR-I1 specimen with a) no filter b) 8 face-connected voxels c) 125 face-connected voxels and d) equivalent spherical diameter of 10 µm filter

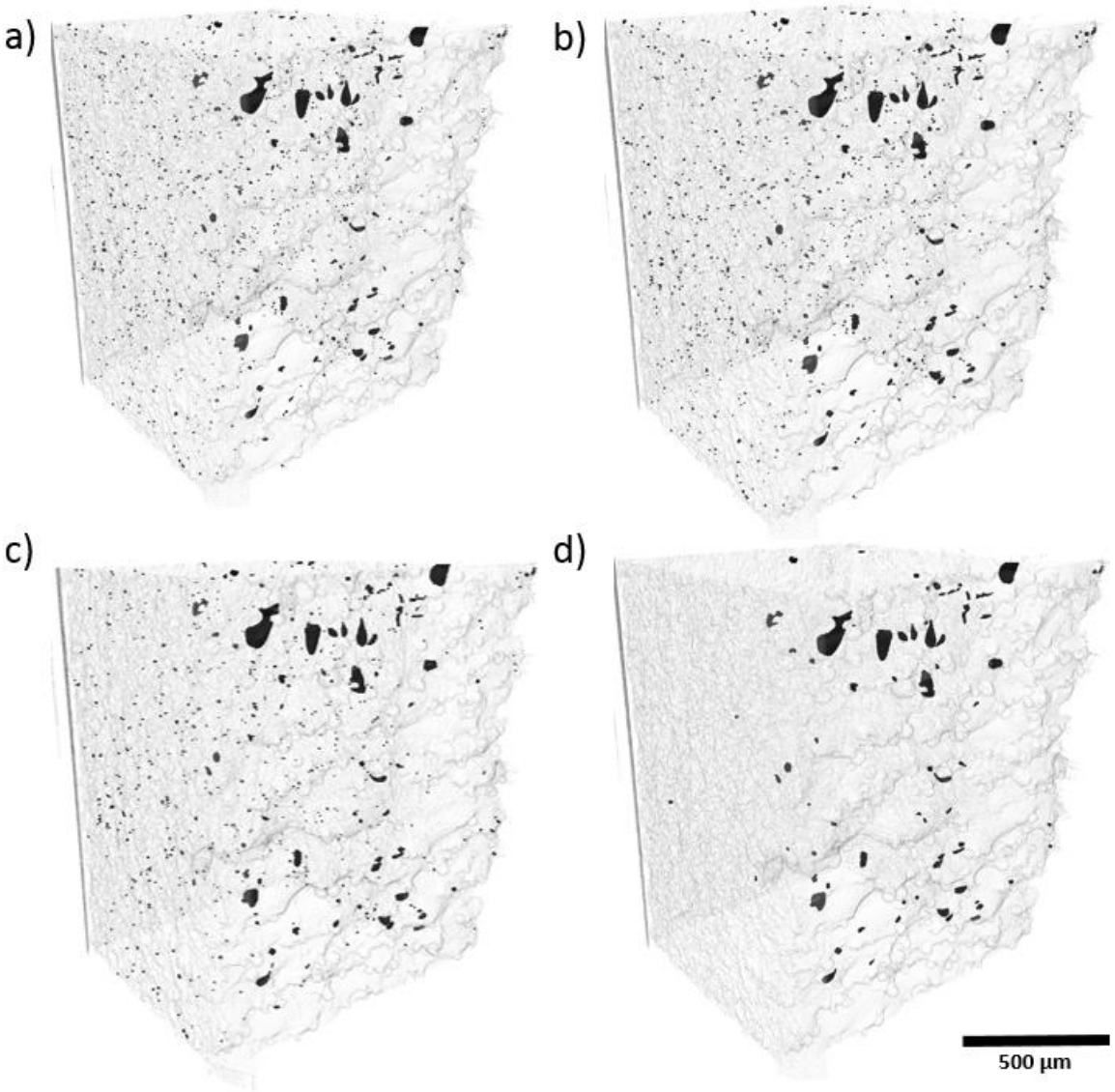

Figure 54: Visualizations of HR-T1 specimen with a) no filter b) 8 face-connected voxels c) 125 face-connected voxels and d) equivalent spherical diameter of 10 µm filter

Visualizations for each HR sample were developed and are provided in Figure 55 and Figure 56 for IN718 and Figure 57 and Figure 58 for Ti64. As mentioned, visualizations are shown with an applied filter on the data of a minimum equivalent spherical diameter of 10 µm or greater to be able to more easily identify trends amongst larger porosity. Figure 55 and Figure 57 compare near-surface vs. in-bulk stress-relieved

specimens for IN718 and Ti64. Similarly, Figure 56 and Figure 58 compare near-surface vs. in-bulk post-processed specimens for IN718 and Ti64. Already noted in observations of the quantified data is the higher level of porosity present in the near-surface specimens compared to their in-bulk counterparts. From the visualizations, it can be further shown that not only are there more pores present in the near-surface samples, an important observation for fatigue life considerations, but there are more large pores (at the filter size or larger) present. Furthermore, observing Figure 55a, Figure 56a, Figure 57a, and Figure 58a, not only are there more large pores available in the near-surface specimens, but of those pores, the most sizable ones are present closest to the free-surface of that sample. Thus, the largest pores present in all of the data are congregated at the free surfaces of the near-surface samples. Visualizations also confirm earlier observations of the quantified data that the mean equivalent spherical diameter decreases from stress-relieved to post-processed specimens, when controlling for the near-surface vs. in-bulk characteristic.

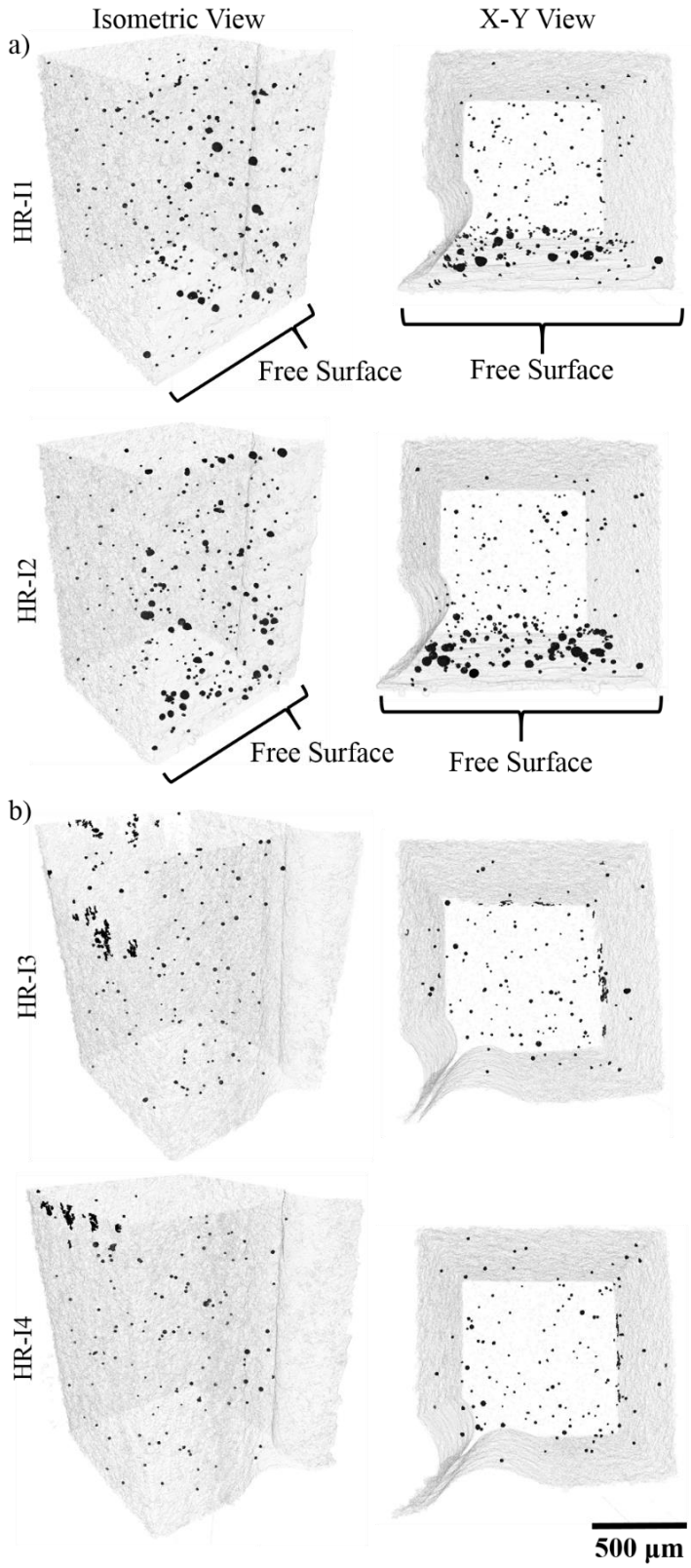

Figure 55: Porosity visualizations of HR IN718 a) near-surface, stress-relieved and b) in-bulk, stress-relieved specimens

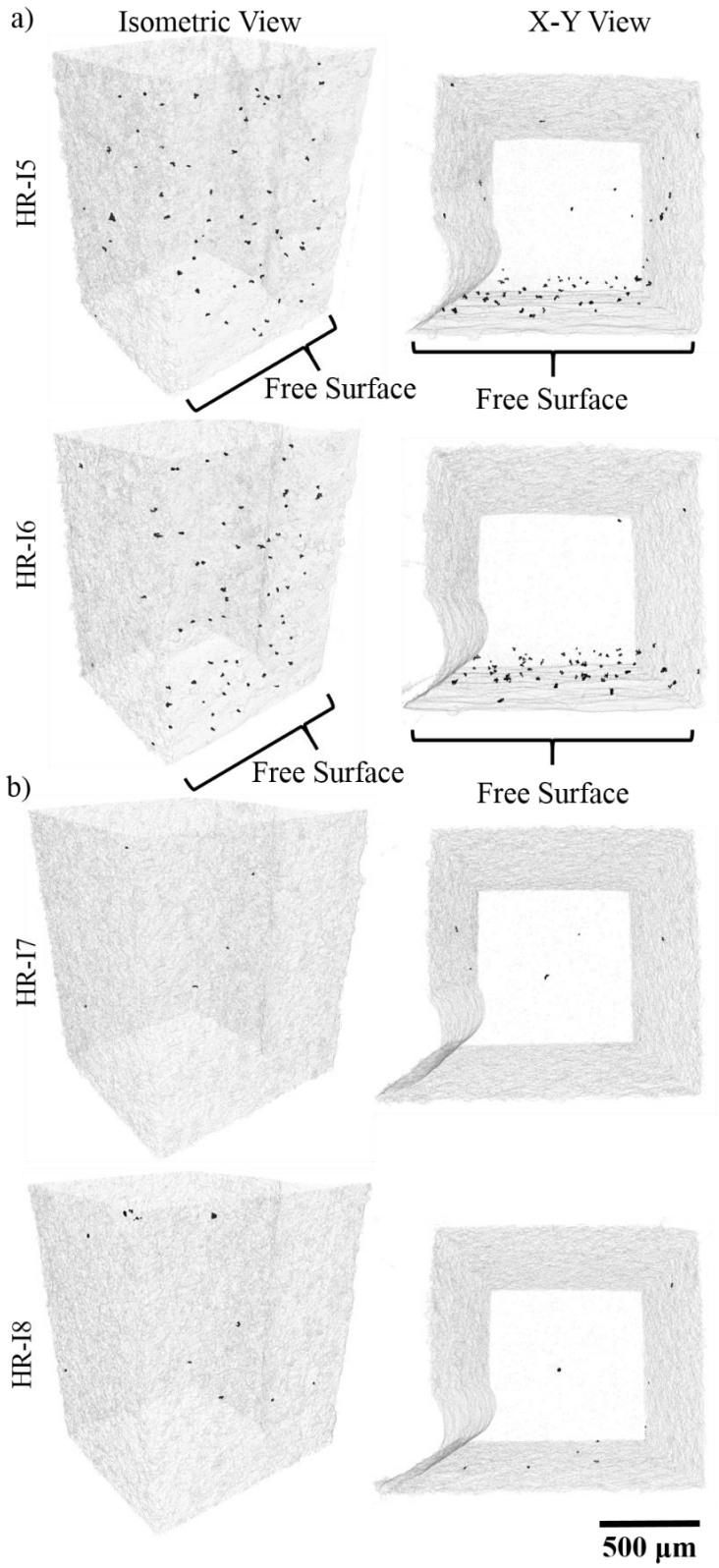

Figure 56: Porosity visualizations of HR IN718 a) near-surface, post-processed and b) in-bulk, post-processed specimens

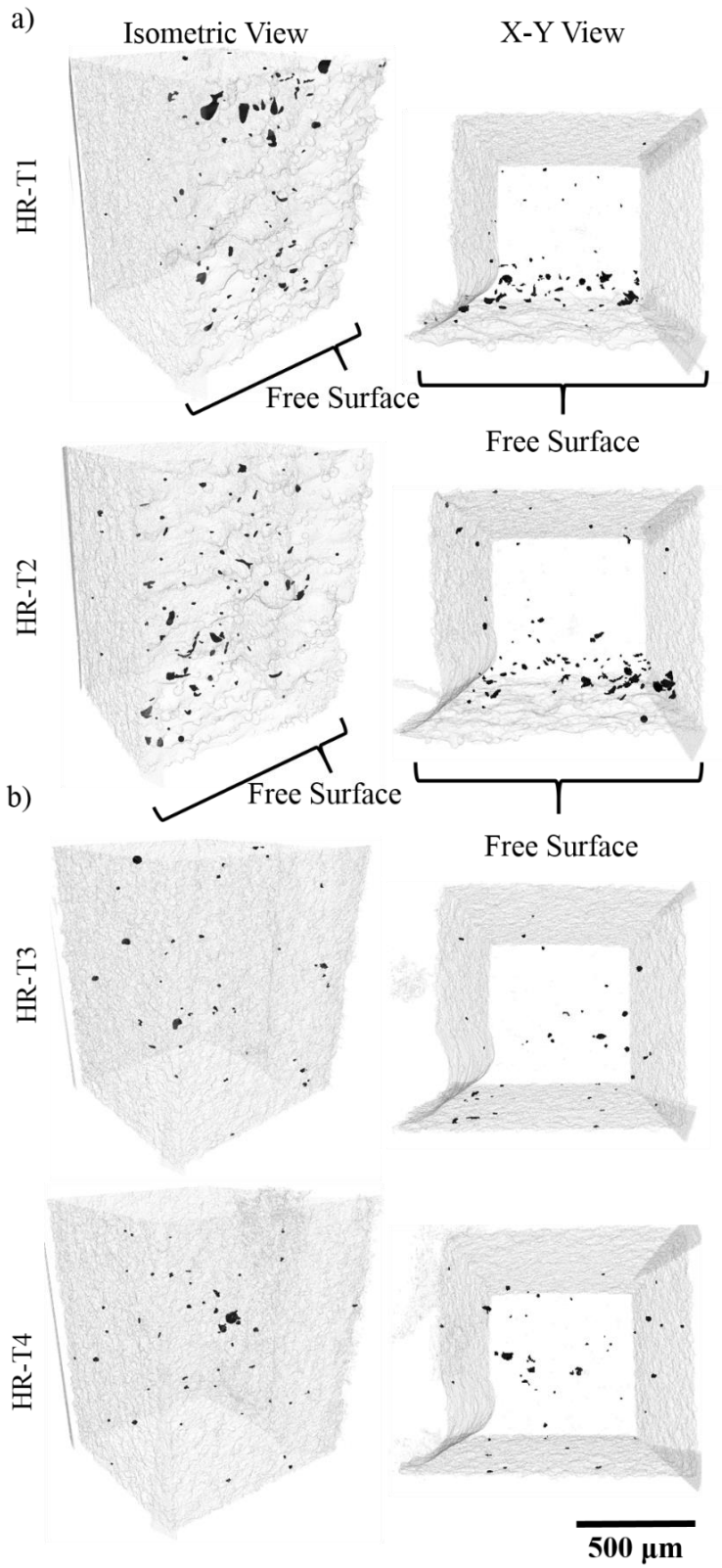

Figure 57: Porosity visualizations of HR Ti64 a) near-surface, stress-relieved and b) in-bulk, stress-relieved specimens

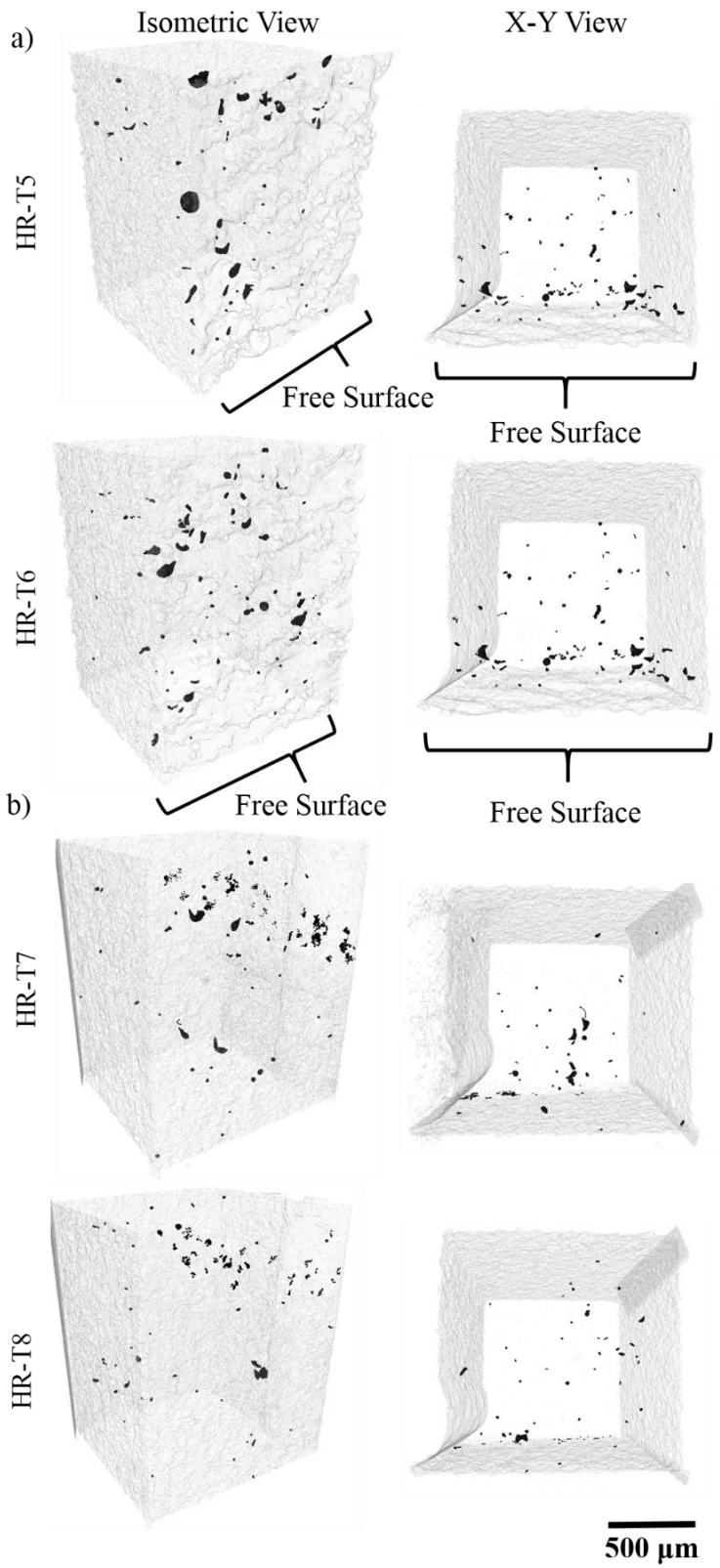

Figure 58: Porosity visualizations of HR Ti64 a) near-surface, post-processed and b) in-bulk, post-processed specimens

4.2.1 Pore Proximity Study

The effect of pore proximity, as previously discussed, could have implications on the mechanical behavior of the material. From the Avizo porosity spatial distribution data, the defects in each specimen were analyzed to determine the distance from one pore to its closest neighboring pore. PDFs were developed for each specimen and presented in Figure 59 and Figure 60 for IN718 and Ti64, respectively. From the PDFs, it can be observed that there is a higher probability for pores to be within 10 μm to their nearest neighbor for post-processed material as compared to purely stress-relieved for both near-surface and in-bulk specimens. This observation holds true for both IN718 and Ti64. Furthermore, the Ti64 samples have a higher probability of pores within a 10 μm proximity to each other than their IN718 counterparts. Furthermore, in all cases, the majority of pores are within 50 μm to their closest neighbors.

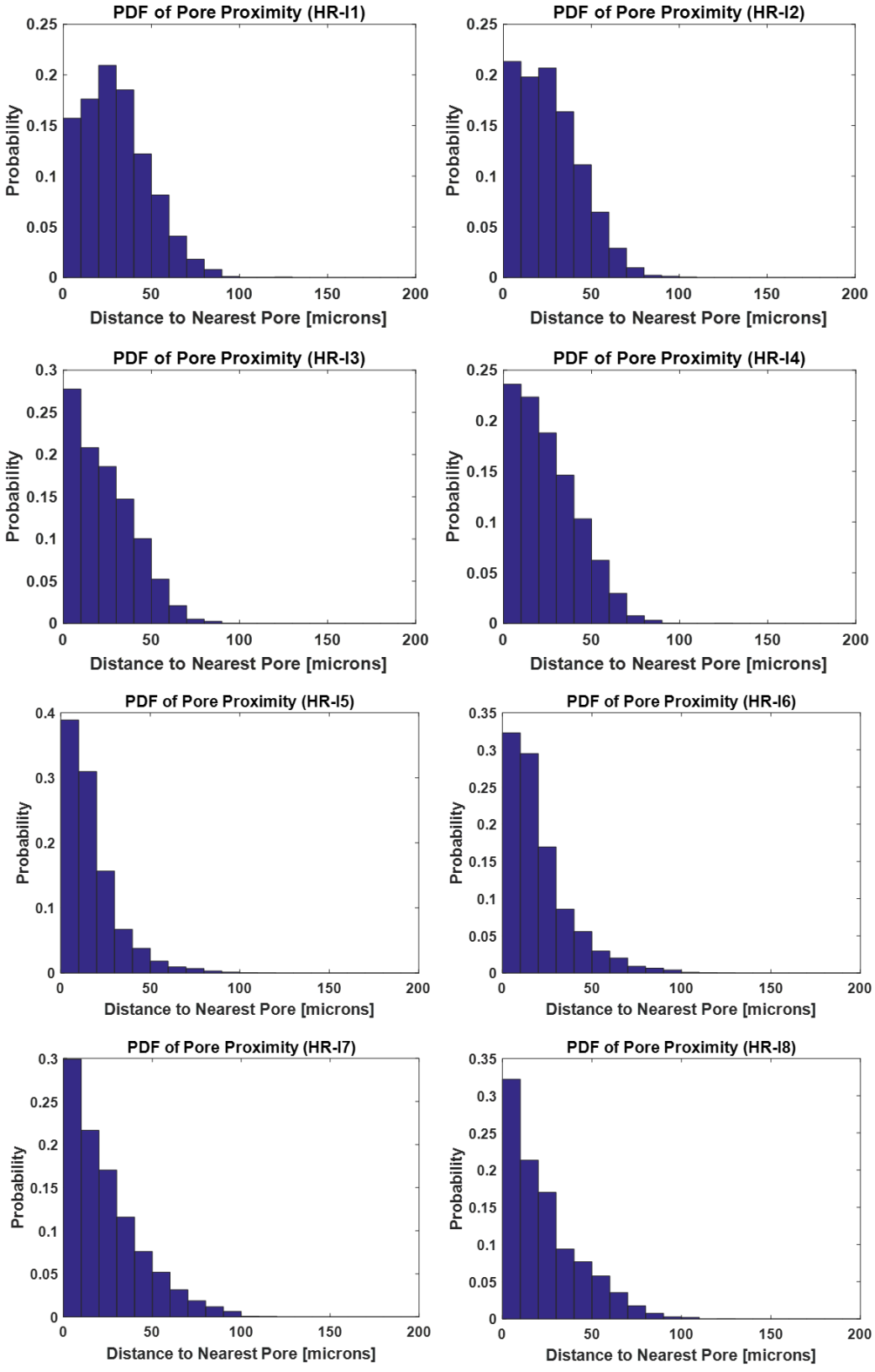

Figure 59: Probability distribution functions of the proximity of pores for IN718 high resolution specimens

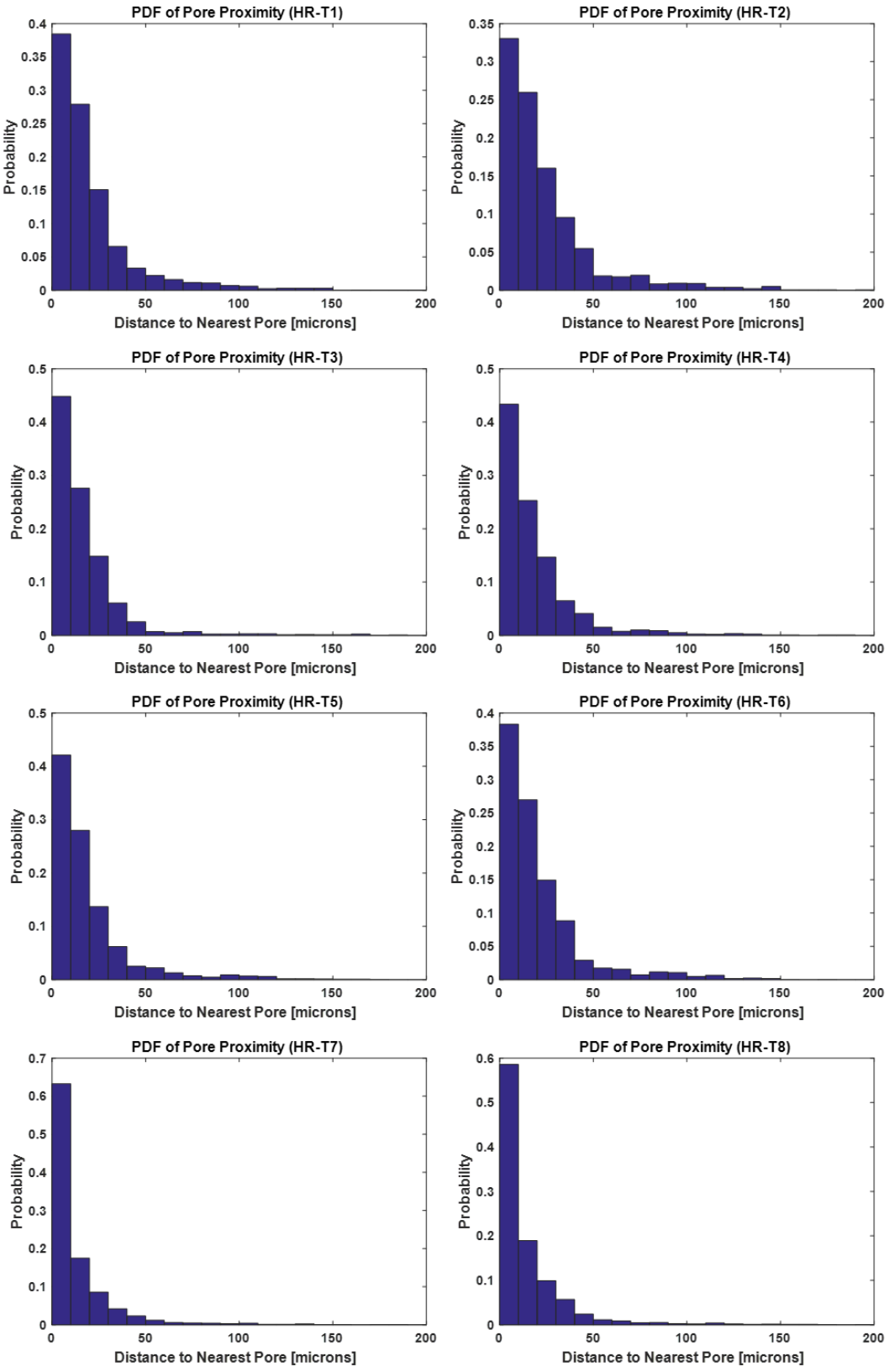

Figure 60: Probability distribution functions of the proximity of pores for Ti64 high resolution specimens

CHAPTER 5. DISCUSSION

5.1 Porosity Quantification and Visualization

In the LR dataset, Ti64 appeared to have a higher porosity volume fraction than IN718 overall, however, the trend switched amongst the HR data. The lack of analyzed samples in both LR and HR data (lowest with LR IN718 but true for all) most likely renders trends derived from characteristics of the individual specimen (i.e. porosity volume fraction), rather than to pores within that specimen (large sample size), statistically insignificant. As such, identified trends of this nature should be taken as initial observations, with implications for future work, and not as definitive findings of this research.

On the other hand, one of the important findings of this research is that the porosity significantly increases in the comparable specimens between LR and HR data, indicating that a large amount of porosity can go undetected with inspection methods that are constrained by lower resolutions. It is important again to note that because HR specimens were cut from specific LR bulk samples that were analyzed, direct comparisons between porosity content of the LR and HR results can be made for all HR specimens – except HR-I5, HR-I6, HR-I7, and HR-I8 – for which no LR CT scan was provided for analysis. This finding seems to confirm suggestions in literature that porosity inspection and analysis via CT should always be taken as a lower limit for material porosity content as increasing CT resolution will further increase detection capabilities [150]. With this in mind, the need to characterize the critical pore size for significance in material performance (fatigue life, strength, etc.) becomes an increasingly heightened priority.

In conjunction, another key takeaway from this thesis is that of the additional pores detected in the HR data, a large number of them were small pores (below 10 μm equivalent spherical diameter filter threshold). As a note, it should be commented that in CT visualizations, the amount of porosity in the specimen often seems exaggerated as pores are shown as projections when viewed in 2D [82]. However, analysis of the pore size filter sensitivity study (Figure 50) and pore size CDFs across different filters (Figure 51 and Figure 52) along with the visual inspection of the filter progression (Figure 53 and Figure 54), the sizable presence of small pores was made clear. The increased presence of individual pores, even small ones, can increase the potential of a crack to form as individual pores serve as crack initiation sites. However, the increased structural vulnerability of the material due to the high presence of small pores will depend heavily on the application of the part, especially for fatigue considerations. As such and as previously noted, more work needs to be done to characterize the critical pore size for crack initiation.

In addition to quantified data, visual data provides the basis for meaningful takeaways from this work. Visual data not only allows for the confirmation of quantified porosity, but also allows for the easier identification of spatial distribution trends. One of the most impactful and definitive findings of this work is the presence of porosity to trend toward the free surfaces of a part.

This finding was observed in both LR and HR data, but also was manifested in the higher presence of porosity found in vertical-built LR dog-bones compared to horizontal-built ones. As discussed in the literature review section, one of the leading theories of porosity formation, especially for those near surfaces, is due to the hatching scan strategy [82][83][84][85]. It was reported that porosity was more likely to form at the turn of the

hatch and where the hatch met the contour [82]. With this in mind, vertical-built specimens would be expected to undergo more hatch turns throughout the entire build, as hatching is performed for each layer along the build axis compared to horizontal-built specimens. Further evidence of this theory can be observed in the X-Z view of Figure 47a, where the concentration of porosity is along the top and bottom edges of the horizontal-built specimens, where the hatch turns would be expected to occur. Similarly, Figure 48b shows a higher concentration of porosity at the top and bottom edges of the Y-Z view of the vertical-built specimens, where the hatch turns are also expected to be. This trend of increasing porosity from horizontal-built to vertical-built specimens is important to note to relate back to the fabrication of parts and how care should be taken during build setup to reduce porosity by minimizing the amount of hatch turns in the specimen or mitigating the formation of porosity in those sections through other means. Knowledge of the exact scan strategy utilized on the build of the LR specimens is needed to confirm the hypotheses.

Additionally, evidence of a higher presence of surface than in-bulk porosity was most clearly exhibited in the comparisons of HR near-surface specimens with their in-bulk counterparts. Not only was higher porosity content observed in the near-surface specimens than in-bulk ones, but the pores were also larger on average. Beyond that, within the near-surface specimens, the quantity of pores and larger pores were further concentrated close to the free-surface than away from it. Large pores are of generally more concern than smaller ones because they are more likely to contribute to crack initiation, due to a higher stress concentration at those pores. Thus, the higher number of all pores and especially large pores present in the near-surface specimens and at the free surfaces of those specimens may provide reasoning for findings in literature that propose that surface

porosity is a bigger detriment to fatigue life than in-bulk porosity [151][41]. These findings may increase the desire to build in mitigation techniques, either in-situ or post-build, to remove surface porosity.

Furthermore, statistical significance tests were performed on the data to determine confidence in the variation of average pore size between the different specimen types. Table 10 displays the results of the tests. As expected, for the most part, LR data does not have a high enough sample size to make conclusions within the 95% confidence interval, except for stress-relieved having larger mean porosity than post-processed IN718. In contrast, all pore size comparisons had statistical significance for HR data, with observed trends being statistically confirmed.

Table 10: Statistical significance comparison of mean equivalent spherical diameter with 95% confidence interval

Statistical Significance		
LR Data	**IN718**	**Ti64**
PP vs. SR	Yes, SR is greater	No
H vs. V	No	No
HR Data	**IN718**	**Ti64**
PP vs. SR	Yes, SR is greater	Yes, SR is greater
FS vs. IB	Yes, NS is greater	Yes, NS is greater

PP = post-processed
SR = stress-relieved
H = horizontal-built
V = vertical-built
FS = near-surface
IB = in-bulk

5.2 Comparison of Porosity with Existing Literature

Porosity values in both materials, even for the as-built specimens, was relatively low overall, which is a good sign for the future prospects of SLM metals being utilized in structurally critical hardware. Porosity volume fractions observed in this research are in line with previously reported levels for SLM IN718 (Table 11), especially with the closest matched work of Smith et al., which analyzes porosity at a resolution of 5.3 μm [55][56][57][58][59][60][61][62]. Similar comparisons for SLM Ti64 (Table 12) yield varied results. Reported porosity levels for Ti64 have a large variation and while volume fraction levels in this research are in line with some findings, others are an order of magnitude lower in porosity volume percentage [23][64][53]. Specifically, the most closely matched research, based on resolution of CT, had minimum levels that were lower than those reported in this research [64][53]. However, those same reports also had porosity levels, based on the processing conditions of the specimens analyzed, in line with those found in this research. There are a number of possibilities why the porosity levels could be different (i.e. different SLM processing conditions, different post-processing treatments, experimental error, etc.), but one consideration further explored in this work is the effect of sampling size, location and resolution on the porosity able to be observed.

Table 11 and Table 12 represent existing reported porosity volume fractions available in literature for baseline samples of SLM IN718 and Ti64, respectively. The tables are ordered first in terms of observation method, and then by observation resolution to be able to see if there were any trends in how porosity volume fraction may change based on sample size and resolution limit. In general, porosity was quantified for the entire part volume using Archimedes' Method and CT scanning and for a limited part volume using

Microscopy. Furthermore, in most references exact resolution limits were not reported, and so microscopy resolutions were calculated based on the assumption that the images provided in the reference were 256 pixels long in their max dimension. What can be seen in both materials is that no clear trends presented themselves when porosity observation was varied by size and resolution. As mentioned, there are many other possible reasons why the porosity is varied across the available literature, including the processing parameters and build quality of the part. However, intuitively we can hypothesize that observed porosity volume content should increase as sample size and observation resolution is increased as more of the porosity is able to be identified. The desire to explore this hypothesis, as well as rationalize the large increase in porosity volume content observed between LR and HR samples from the same specimen, led to the development of a porosity observation study utilizing a statistical simulation of pores in an arbitrary volume to provide further analysis.

Table 11: Survey of reported porosity content in SLM IN718 studies

Reference	Machine	Condition	Observation Method	Resolution [µm/pixel]	Porosity Volume Fraction [%]
Sadowski et al.	M280	as-built	Archimedes	N/A	$2.00*10^{0}$
Tillman et al.	SLM 250 HL	as-built	Microscopy	27.76	$1.30*10^{-1}$
Tillman et al.	SLM 250 HL	as-built	Microscopy	27.76	$9.00*10^{-2}$
Choi et al.	Concept Laser Mlab Cusing	as-built	Microscopy	4.73	$3.50*10^{-1}$
Marchese et al.	M270	as-built	Microscopy	3.91	$3.00*10^{-1}$
Parimi et al.	Quantum DLF	as-built	Microscopy	3.09	$2.00*10^{-1}$
Parimi et al.	Quantum DLF	as-built	Microscopy	3.09	$2.00*10^{-1}$
Parimi et al.	Quantum DLF	as-built	Microscopy	3.09	$8.00*10^{-1}$
Strobner et al.	Not reported	SR, Anneal, Aging	Microscopy	2.85	$2.00*10^{-2}$
Sanz et al.	Not reported	as-built	Microscopy	0.69	$2.00*10^{-2}$
Sanz et al.	Unknown	HT & Shot Peened	Microscopy	0.69	$1.70*10^{-1}$
Trosch et al.	Not reported	HT & Aging	Microscopy	N/A	$2.00*10^{-2}$
Tillman et al.	SLM 250 HL	as-built	CT	8.00	$6.90*10^{-2}$
Smith et al.	M280	as-built	CT	5.30	$4.00*10^{-2}$

Table 12: Survey of reported porosity content in SLM Ti64 studies

Reference	Machine	Condition	Observation Method	Resolution [um/pixel]	Porosity Volume Fraction [%]
Gong et al.	M270	as-built	Archimedes	N/A	$<1.00*10^{0}$
Do et al.	SLM 250HL	as-built	Archimedes	N/A	$8.00*10^{-1}$
Do et al.	SLM 250HL	as-built	Archimedes	N/A	$1.00*10^{0}$
Thijs et al.	LM-Q	as-built	Archimedes	N/A	$4.00*10^{-1}$
Vilaro et al.	Trumpf LF250	SR	Archimedes	N/A	$<1.00*10^{-1}$
Kasperovich et al.	M2	as-built	Microscopy	8.19	$5.01*10^{-1}$
Kasperovich et al.	M2	as-built	Microscopy	8.19	$1.33*10^{-1}$
Mertens et al.	SLM 250HL	HT	Microscopy	5.62	$5.00*10^{-1}$
Qiu et al.	M2	as-built	Microscopy	5.32	$1.00*10^{-1}$
Yang et al.	LSNF-2	as-built	Microscopy	3.91	$5.00*10^{-1}$
Antonysamy et al.	M270	SR	Microscopy	3.78	$2.90*10^{-1}$
Antonysamy et al.	M270	SR	Microscopy	3.78	$1.67*10^{0}$
Facchini et al.	M270	as-built	Microscopy	2.93	$3.00*10^{-1}$
Leuders 2013 et al.	SLM 250HL	as-built	CT	20.00	$2.30*10^{-1}$
Krakhmalev et al.	M280	as-built	CT	10.00	$1.80*10^{-3}$
Krakhmalev et al.	M280	SR	CT	10.00	$2.20*10^{-3}$
Kasperovich et al.	M2	as-built	CT	1.20	$4.15*10^{-1}$
Cunningham et al.	M290	as-built	CT	0.65	$6.37*10^{-3}$

5.3 Porosity Observation Study

The study of simulated porosity in a specimen was conducted to test different cases of resolution and sample size. The goal of the simulation was to observe what changes in

porosity volume fraction should be expected when sampling a fixed volume of material with changing sample size, location and resolution. This was done in order to rationalize the lack of large increase in porosity volume fraction seen in literature, as observation resolution increased, which differed from the results of this thesis. The model was developed with parameters based off of the actual LR and HR specimens in the experimentation of this research. The methodology for the model is described further. First, a cubic specimen measuring $27*10^3$ μm on each dimension was populated with pores, as shown in Figure 61. Pores are assumed to be spherical in morphology. The distribution of porosity size was of the form of a truncated Gaussian-like scatter with normal distribution parameters (mean = 5 μm; standard deviation = 3 μm) chosen to approximate those calculated from the HR-I1 sample. The distribution was truncated with limits imposed at 0.2 μm and 60 μm representing the minimum observable defect size with a 0.1 μm resolution limit and the minimum observable defect size for the LR specimens, respectively (Figure 61). Porosity was uniformly spatially distributed throughout the sample. The total number of pores chosen to distribute using the truncated size distribution was chosen to have the same pore count density as observed in the HR-I1 specimen. This count was rounded to $7.4*10^7$ pores throughout the full specimen volume. Since bigger pores are more impactful to mechanical behavior and of larger concern, 25 random large pores (RLPs) were inserted into the specimen at random locations, ranging from 20 μm to 100 μm in equivalent spherical diameter, as shown in the magnified pore distribution histogram in Figure 61. The total porosity volume percentage of the full volume specimen equaled $5.42*10^{-2}$ %.

The study was conducted by simulating different test cases of the model, shown in Table 13. The test cases consist of determining an average volume fraction of 10 different samples of the specimen that have the same observation resolution and dimensions but are randomly sampling the specimen in different locations. Essentially, Table 13 depicts the different resolutions and sample sizes used, and for each test case 10 different randomly located samples are taken. The random sampling of the specimen for different sample observation parameters (test cases) is shown schematically in Figure 62 Figure 63. It is important to note that the minimum observable pore size (largest pore dimension) is 2x the resolution limit as it is impossible to rule out the possibility that perceived pores smaller than that could in reality be anything more than noise.

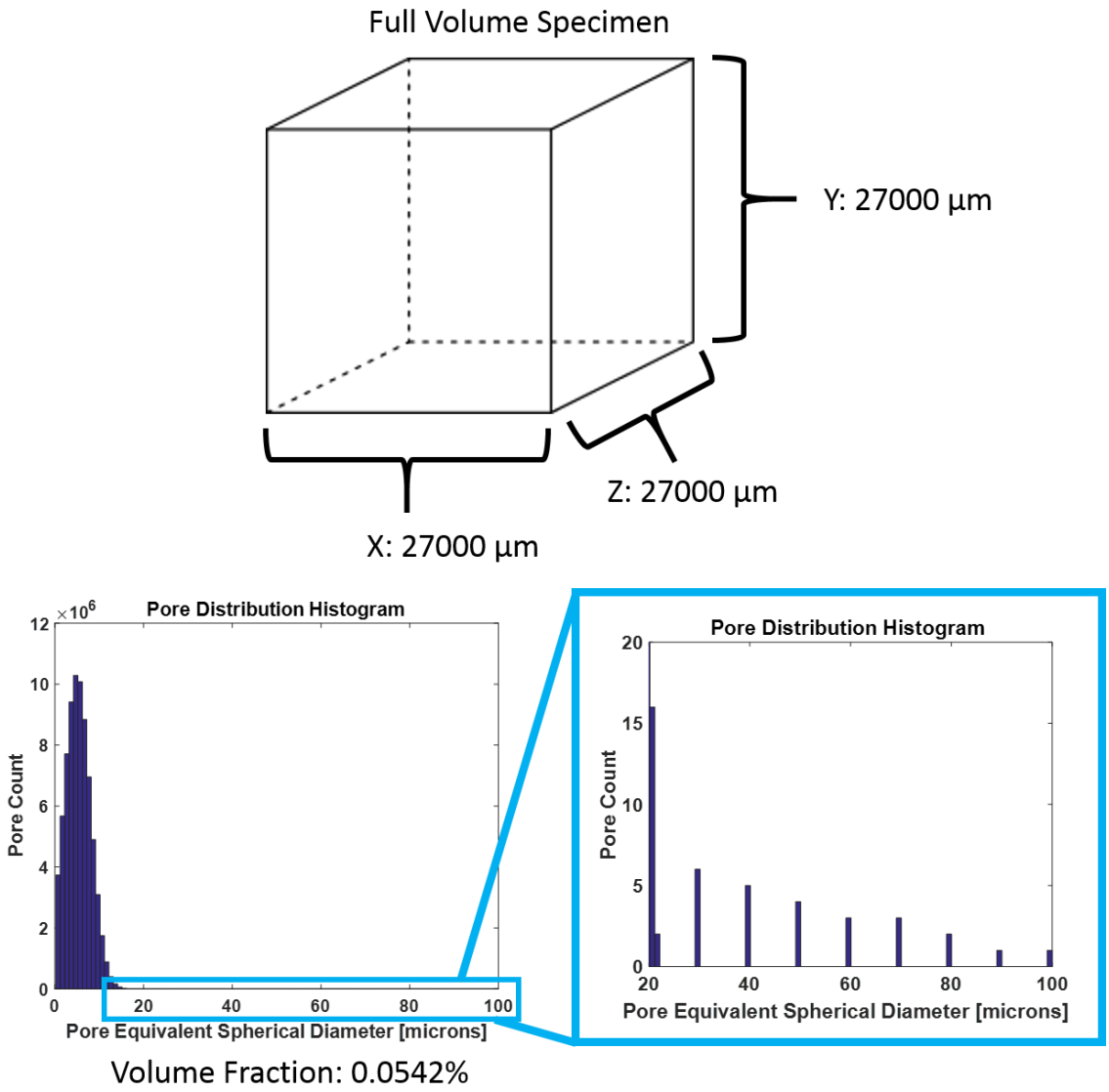

Figure 61: Specimen dimensions and size distribution of simulated specimen porosity

Table 13: Sample sizes and resolutions used to observe porosity within specimen

Sample Test Cases								
	Resolution [µm]							
	0.65	***2***	***5***	***10***	***20***	***30***	***40***	***50***
Sample Size Volume (*10³) [µm³]	1	1	1	1	1	1	1	1
	1.5	1.5	1.5	1.5	1.5	1.5	1.5	1.5
	3	3	3	3	3	3	3	3
	5	5	5	5	5	5	5	5
	7.5	7.5	7.5	7.5	7.5	7.5	7.5	7.5
	10	10	10	10	10	10	10	10
	15	15	15	15	15	15	15	15
	20	20	20	20	20	20	20	20
	25	25	25	25	25	25	25	25
	27	27	27	27	27	27	27	27

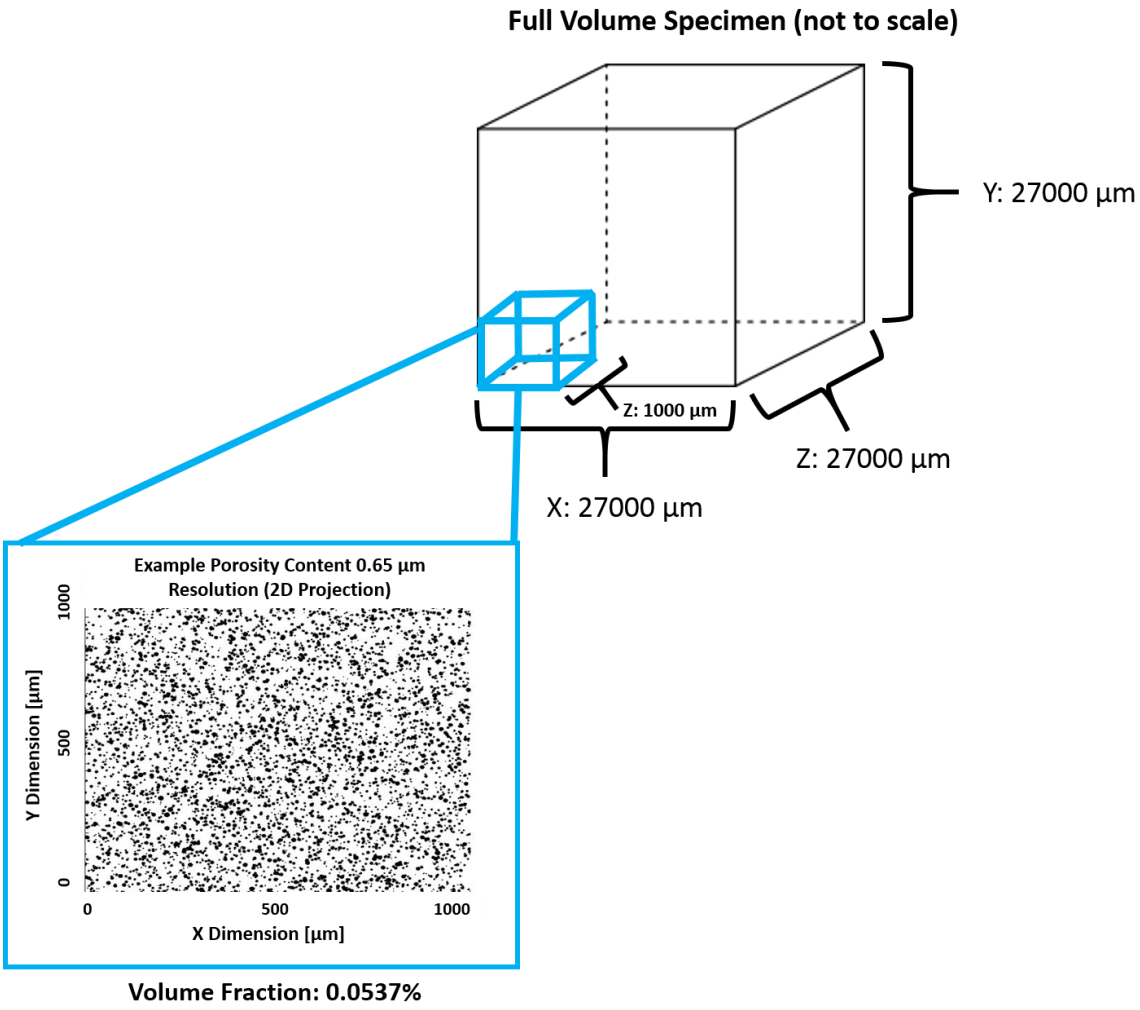

Figure 62: Schematic visualization of porosity in a 1000 µm^3, 0.65 µm sample

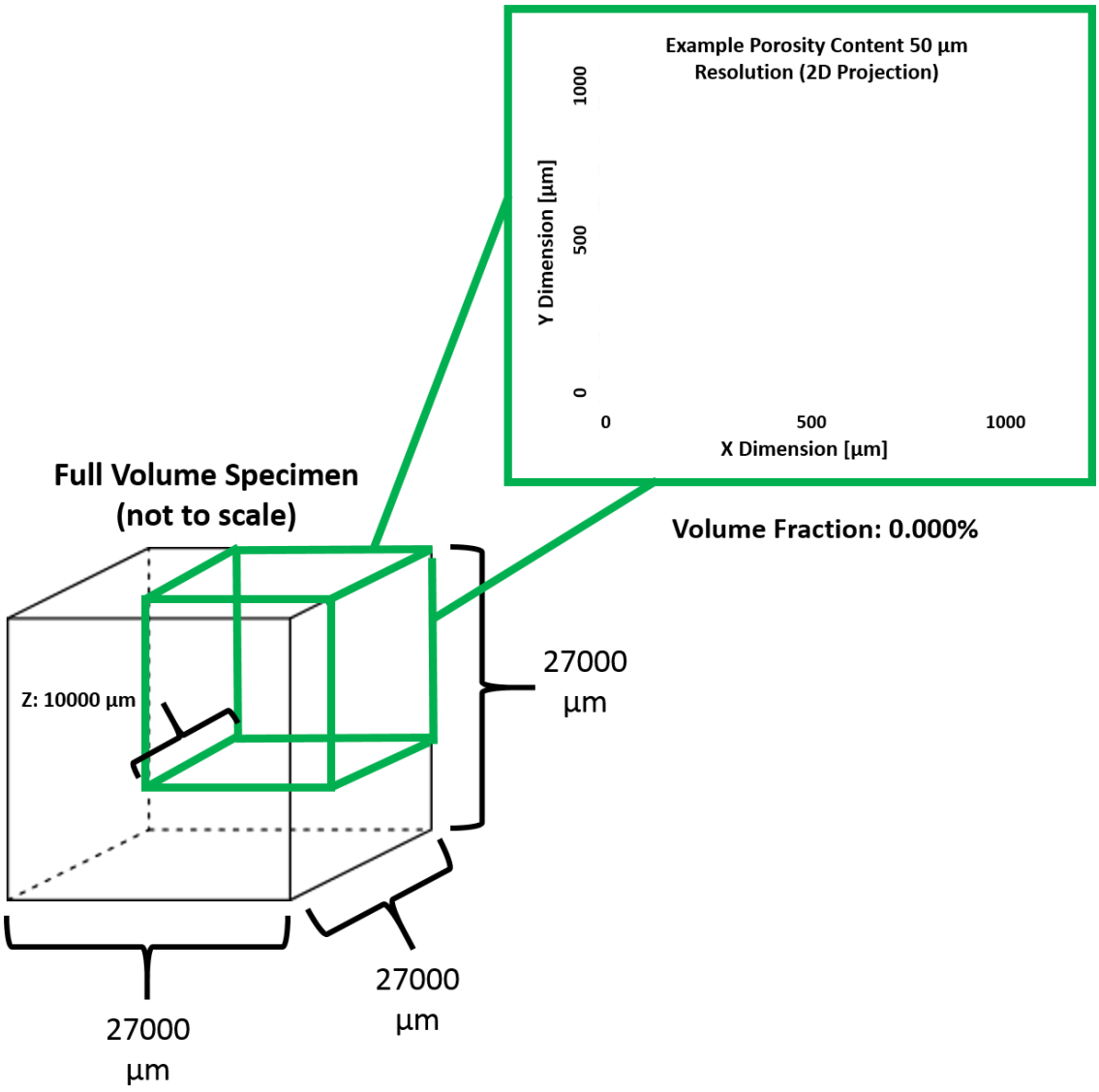

Figure 63: Schematic visualization of porosity in a 10000 μm^3, 50 µm sample

Results of the study are displayed graphically in Figure 64 and Figure 65, with exact values reported in Table 14. The study provides evidence in support of the hypothesis that material porosity volume content should be significantly larger as observation resolution increases, which was experienced in the results of this thesis. For porosity distributions observed in the SLM IN718 material, of which this simulation is based, it is clear that there

is a several order of magnitude drop in observable porosity content for sample resolution limits higher than 5 μm and a greater than 70% drop in observable porosity content for resolution limits higher than 2 μm. Furthermore, there seems to be no large difference in observable porosity content when varying sample size of the same resolutions. The results of this study also provide more confidence that the porosity volume content discrepancy seen between the LR and HR specimens are accurate and that observation resolution may be more important than sample volume size when attempting to determine the true porosity content of the part.

Additionally, one of the biggest takeaways from this porosity study is best understood when analyzing the information in conjunction with the pore proximity study. This pore observation study confirms results seen in experimental data that there is a large amount of individual pores present in SLM material that is only observable with very high resolutions. The general consensus is that only a resolution that is able to capture the critical defect size of the material is necessary when checking for porosity because using higher resolution systems is often more cost and time intensive while not providing information important to the life cycle management of the part. However, previous research has shown that clusters of subcritical pores can have a magnifying effect on the stress concentration in their localized volume and can actually become supercritical crack initiation sites in some cases. The pore proximity study has shown that in both the SLM IN718 and Ti64 there are a majority of pores within 10 μm to their closest neighbor and could imply that some of these subcritical pores are close enough to each other to act as supercritical. The results of these studies, when taken together, provide at least enough evidence to justify further work into determining the exact critical defect size of SLM

IN718 and Ti64, in the case of a singular defect, as well as that of a defect with others in close proximity.

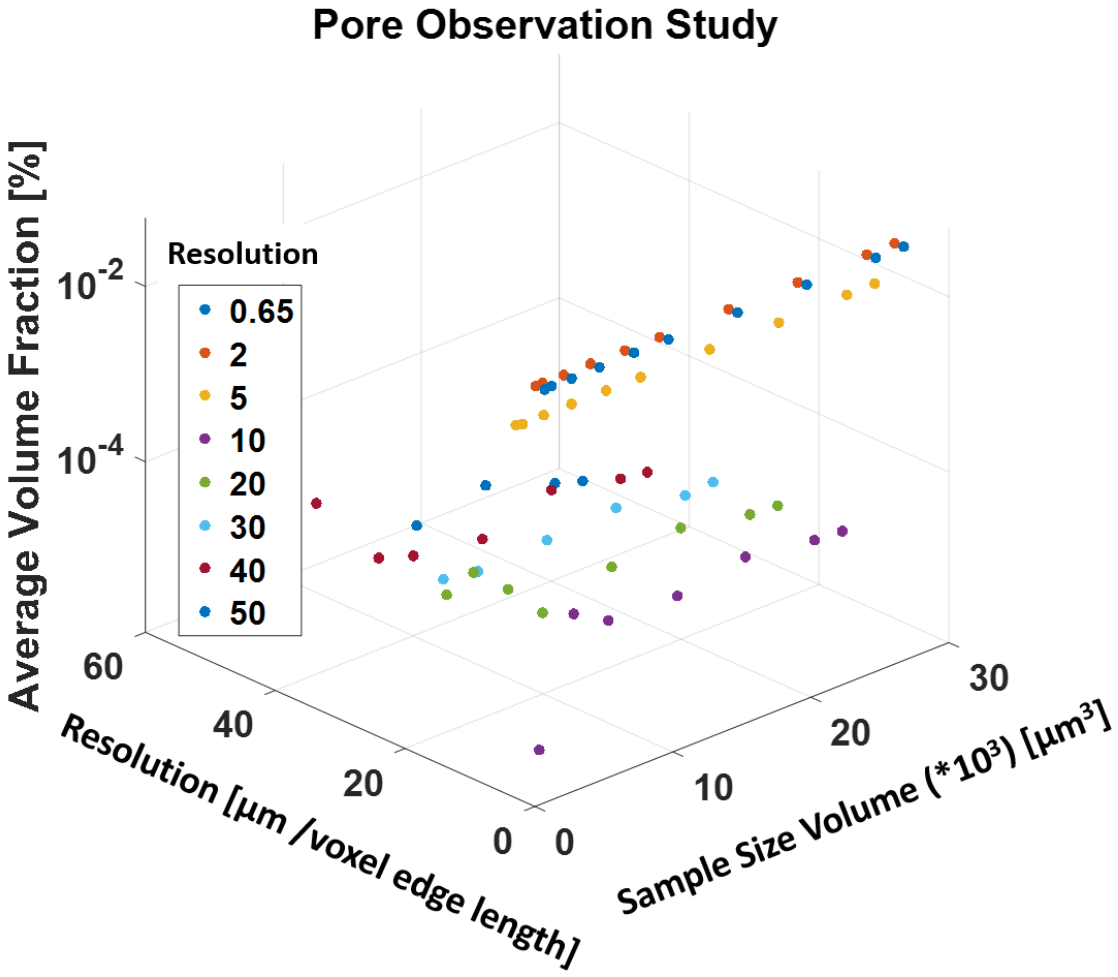

Figure 64: Average volume fraction of samples with varying size and resolution

Table 14: Average volume fraction of samples with varying size and resolution

Avg. Volume Fraction [%]		Resolution [µm]							
		0.65	2	5	10	20	30	40	50
Sample Size Volume (*10³) [µm³]	1	5.37E-02	5.23E-02	1.48E-02	0.00E+00	0.00E+00	0.00E+00	0.00E+00	0.00E+00
	1.5	5.43E-02	5.24E-02	1.43E-02	0.00E+00	0.00E+00	0.00E+00	0.00E+00	0.00E+00
	3	5.40E-02	5.28E-02	1.47E-02	0.00E+00	4.19E-05	0.00E+00	9.93E-05	0.00E+00
	5	5.42E-02	5.28E-02	1.46E-02	1.13E-06	5.63E-05	0.00E+00	0.00E+00	0.00E+00
	7.5	5.43E-02	5.28E-02	1.46E-02	2.86E-05	2.53E-05	1.51E-05	1.24E-05	0.00E+00
	10	5.42E-02	5.28E-02	1.46E-02	1.64E-05	9.38E-06	1.31E-05	9.18E-06	0.00E+00
	15	5.43E-02	5.28E-02	1.46E-02	1.54E-05	1.56E-05	1.44E-05	6.95E-06	4.65E-06
	20	5.43E-02	5.28E-02	1.46E-02	2.07E-05	2.07E-05	1.65E-05	1.22E-05	6.55E-06
	25	5.43E-02	5.28E-02	1.46E-02	1.60E-05	1.45E-05	1.13E-05	8.02E-06	3.35E-06
	27	5.42E-02	5.28E-02	1.46E-02	1.49E-05	1.40E-05	1.18E-05	7.32E-06	2.66E-06

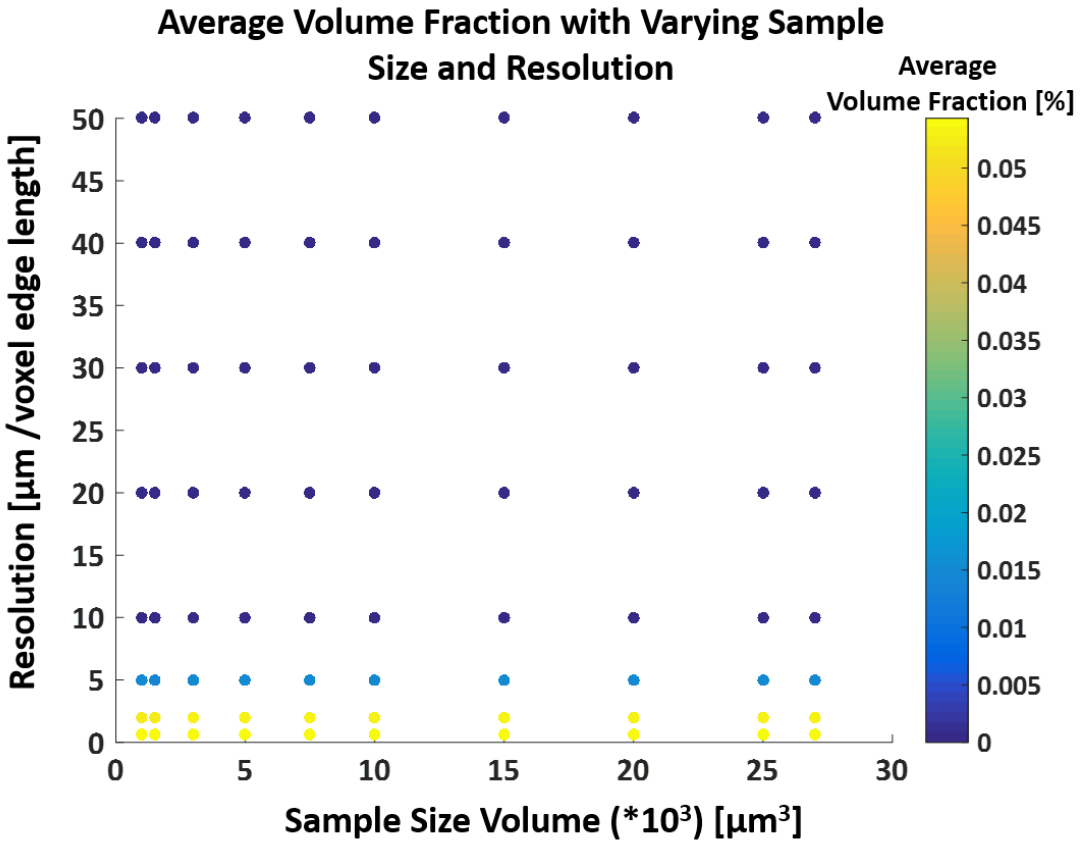

Figure 65: Color map of average volume fraction of samples with varying size and resolution

CHAPTER 6. CONCLUSIONS AND FUTURE WORK

6.1 Conclusions

This thesis has built off previous work in the field and also laid further foundation for continued research into porosity observation via synchrotron-based microscale computed tomography, specifically in selectively laser melted Inconel 718 and Ti-6Al-4V with different build orientations and processing conditions. Tomographic images were reconstructed from detector data of CT scans conducted at Penn State University's CIMP-3D and Argonne National Laboratory's Advanced Photon Source, resulting in a 30 μm (LR) and 0.65 μm (HR) voxel edge length, respectively. The tomographs were then processed and thresholded using both ImageJ and Avizo software. Finally, thresholded image stacks were analyzed in Avizo to quantify porosity characteristics including amount, size and spatial distribution. Analysis of the quantified data, along with accompanying simulations, allowed for comparisons and conclusions to be drawn about the material defects.

The first conclusion of this work is that there is a large amount of porosity with a minimum width below 60 μm (2 times the LR pixel edge size) present within the material. Thus, this porosity is undetectable in the 30 μm resolution scans. This finding was revealed by analysis of the HR specimens, which showed thousands of small pores and a higher porosity volume percentage than the larger LR specimens that they were sampled from. This trend is also confirmed qualitatively with comparison of the LR and HR specimen visualizations. The pore observation study supported this conclusion and also showed that

there are large expected reductions in observable porosity with a resolution limit higher than 2 μm.

Secondly, it was found that post-processing of SLM material via heat treatment reduces the average size of pores compared to those that are purely stress relieved while on the build plate. For IN718 near-surface samples, the mean spherical equivalent diameter of the pores reduced from 5.2 μm to 4.2 μm when processed. Similarly for IN718 in-bulk samples, the mean diameter reduced from 4.6 μm to 3.9 μm. In Ti64, the reductions were less pronounced than IN718 at 4.6 μm to 4.5 μm and 4.2 μm to 3.8 μm for near-surface and in-bulk samples, respectively. A test of statistical significance with a 95 % confidence interval confirmed these findings.

One of the major findings of this work is that porosity volume was larger near the surface of the specimens and that those pores were larger on average than those observed in the bulk of the material. Visualizations of the LR data show the propensity of the detectable pores, which are larger than 60 μm minimum width, to be congregated near the surfaces. Further investigation of the HR data shows that there is a higher volume percentage in the near-surface samples than in the in-bulk ones. However, it is not necessarily true that there are more individual pores in the near-surface samples as many of the comparable in-bulk samples had a higher pore count. Thus, it is appropriate to conclude that the surfaces of a specimen also have a higher likelihood for large pores. This finding was confirmed by a statistical significance test with a confidence interval of 95% conducted on the mean spherical equivalent diameter of near-surface samples compared to in-bulk ones in the HR dataset.

Lastly, the pore proximity study showed that both the SLM IN718 and Ti64 material had a plurality of pores within 10 μm of each other. This is an important observation for implications on future work, which may need to investigate the roll of small pore clusters on mechanical performance for SLM IN718 and Ti64.

6.2 Future Work

Though the presence of porosity in SLM IN718 and Ti64 has been demonstrated as well as commentary given about the spatial distribution, quantity, and size of the observed pores, investigation of this topic could benefit from future research.

The acceptability of computed tomography as an effective, reliable and low-error method for inspection of porosity in structurally critical components could benefit from a more in depth of analysis of grayscale thresholding for tomographic imagery. Specifically, being able to match which algorithms are best suited for thresholding of tomographic images depending on their grayscale image defects (i.e. scatter, beam-hardening, noise, etc.) and observing the quality of the resultant thresholded output would be beneficial. Filling in this knowledge gap will help analyzers of CT data to choose the optimum algorithm based on the characteristic defects present in a given grayscale tomograph. Development in this area should aim at creating an autonomous method for analyzing tomographs to reduce time required for large datasets with relatively large variations amongst the grayscale images.

Another area in need of extended research is in the relation of pore characteristics and locations back to the exact processing conditions of the build through post-build CT and in-situ monitoring. CT enables knowledge of the exact 3D location of a defect and its

morphology, which can be related back to when a defect occurred during a build and its final shape. In-situ monitoring can confirm when the defect occurred as well as allow observation of the direct formation of a pore. This work can extend the knowledge base of how and why pores form, providing direct evidence to previous work that has hypothesized how a pore formed based upon morphology, location, or modeling but not direct monitoring of the process.

Further potential work could aim towards determining what is the ratio of total randomly sampled volume to total specimen volume that is adequate to reach an acceptable difference in the observable porosity content and the actual porosity content. The pore observation study showed little to no change in total sampled volume for constant sample resolutions, implying that there was not a meaningful difference in using larger sample sizes. However, it should be explored how the observable porosity changes for total sampled volumes that are both small and large compared to the total specimen volume.

Additionally, research into determining the critical defect size for these materials, both for singular pores and pore clusters is necessary in determining whether the current porosity inspection methods are adequate to identify all voids that potentially have a significant effect on the mechanical performance of the part.

Finally, this research would also benefit from a larger batch size of specimens tested to generate a larger statistical basis for the results shown.

REFERENCES

[1] S. H. Huang, P. Liu, A. Mokasdar, and L. Hou, "Additive manufacturing and its societal impact: a literature review," *Int. J. Adv. Manuf. Technol.*, vol. 67, no. 5–8, pp. 1191–1203, Jul. 2013.

[2] N. Guo and M. C. Leu, "Additive manufacturing: technology, applications and research needs," *Front. Mech. Eng.*, 2013.

[3] G. N. Levy, R. Schindel, and J. P. Kruth, "Rapid Manufacturing and Rapid Tooling With Layer Manufacturing (Lm) Technologies, State of the Art and Future Perspectives," *CIRP Ann. - Manuf. Technol.*, vol. 52, no. 2, pp. 589–609, 2003.

[4] J. P. Kruth, "Material Incress Manufacturing by Rapid Prototyping Techniques," *CIRP Ann. - Manuf. Technol.*, vol. 40, no. 2, pp. 603–614, 1991.

[5] C. R. Deckard, "Method and Apparatus for Producing Parts by Selective Sintering," 4863538, 1989.

[6] W. Meiners, K. Wissenbach, and A. Gasser, "Selective Laser Sintering at Melting Temperature," 6215093, 2001.

[7] J. P. Kruth, L. Froyen, J. Van Vaerenbergh, P. Mercelis, M. Rombouts, and B. Lauwers, "Selective laser melting of iron-based powder," *J. Mater. Process. Technol.*, vol. 149, no. 1–3, pp. 616–622, 2004.

[8] W. Meiners, K. Wissenbach, and R. Poprawe, "Direct selective laser sintering of steel powder," *Proc. LANE*, 1997.

[9] C. Over, W. Meiners, K. Wissenbach, M. Lindemann, and J. Hutfless, "Laser melting: a new approach for the direct manufacuring of metal parts and tools," *Proc. Euro-uRapid Int. User's Conf.*, 2002.

[10] N. Yamamoto and K. Sakai, "Electron Beam Melting Method for Metallic Material," 2005.

[11] W. E. Frazier, "Metal additive manufacturing: A review," *Journal of Materials Engineering and Performance*. 2014.

[12] A. H. Nickel, D. M. Barnett, and F. B. Prinz, "Thermal stresses and deposition patterns in layered manufacturing," *Mater. Sci. Eng. A*, vol. 317, no. 1–2, pp. 59–64, 2001.

[13] D. T. Pham and S. S. Dimov, "Rapid prototyping and rapid tooling - the key enablers for rapid manufacturing."

[14] "Additive manufacturing: opportunities and constraints," London, 2013.

[15] “SpaceX Launches 3D-Printed Part to Space, Creates Printed Engine Chamber | SpaceX.” [Online]. Available: http://www.spacex.com/news/2014/07/31/spacex-launches-3d-printed-part-space-creates-printed-engine-chamber-crewed. [Accessed: 17-Jul-2017].

[16] M. Gnam, R. Plourde, and T. McDonald, “Laser Engineered Net Shaping (LENS),” in *JTAG Business Meeting*, 2000.

[17] E. Musk, “SpaceX SuperDraco inconel rocket chamber w regen cooling jacket emerges from EOS 3D metal printer.” Twitter, Inc., 2013.

[18] D. Zhang, W. Niu, X. Cao, and Z. Liu, “Effect of standard heat treatment on the microstructure and mechanical properties of selective laser melting manufactured Inconel 718 superalloy,” *Mater. Sci. Eng. A*, no. 644, pp. 32–40, 2015.

[19] T. Book, “Structural Integrity of Additive Materials: Microstructure, Fatigue Behavior, and Surface Processing,” Purdue University, 2016.

[20] S. Leuders *et al.*, “On the mechanical behaviour of titanium alloy TiAl6V4 manufactured by selective laser melting: Fatigue resistance and crack growth performance,” *Int. J. Fatigue*, 2013.

[21] M. Peters, J. Hemptenmacher, J. Kumpfert, and C. Leyens, *Structure and Properties of Titanium and Titanium Alloys*. 2003.

[22] L. Thijs, F. Verhaeghe, T. Craeghs, J. Van Humbeeck, and J.-P. Kruth, “A study of the microstructural evolution during selective laser melting of Ti–6Al–4V,” *Acta Mater.*, vol. 58, pp. 3303–3312, 2010.

[23] C. Qiu, N. J. E. Adkins, and M. M. Atallah, “Microstructure and tensile properties of selectively laser-melted and of HIPed laser-melted Ti-6Al-4V,” *Mater. Sci. Eng.*, pp. 230–239, 2013.

[24] “Porosity,” *Merriam-Webster.com*. [Online]. Available: https://www.merriam-webster.com/dictionary/porosity. [Accessed: 04-May-2017].

[25] “Cast vs Wrought - Rolled Alloys, Inc.” [Online]. Available: https://www.rolledalloys.com/technical-resources/fabrication-information/cast-vs-wrought/. [Accessed: 08-May-2017].

[26] M. J. Couper, A. E. Neeson, and J. R. Griffiths, “Casting Defects and the Fatigue Behaviour of an Aluminium Casting Alloy,” *Fatigue Fract. Eng. Mater. Struct.*, vol. 13, no. 3, pp. 213–227, 1990.

[27] Q. G. Wang, D. Apelian, and D. A. Lados, “Fatigue behavior of A356-T6 aluminum cast alloys. Part I. Effect of casting defects,” *J. Light Met.*, vol. 1, no. 1, pp. 73–84, 2001.

[28] J. D. Harrison, M. G. Dawes, G. L. Archer, and M. S. Kamath, “the Cod Approach and Its Application To Welded Structures,” *Astm Stp 668*, pp. 606–631, 1979.

[29] H. Danninger and B. Weiss, “The influence of defects on high cycle fatigue of metallic materials,” *J. Mater. Process. Technol.*, vol. 143–144, no. 1, pp. 179–184, 2003.

[30] N. Chawla, T. F. Murphy, K. S. Narasimhan, M. Koopman, and K. K. Chawla, “Axial fatique behavior of binder-treated versus diffusion alloyed powder metallurgy steels,” *Mater. Sci. Eng. A*, vol. 308, no. 1–2, pp. 180–188, 2001.

[31] E. Pessard, F. Morel, and A. Morel, “The anisotropic fatigue behavior of forged steel,” *Adv. Eng. Mater.*, vol. 11, no. 9, pp. 732–735, 2009.

[32] J. K. Mackenzie, “The Elastic Constants of a Solid containing Spherical Holes,” *Proc. Phys. Soc. Sect. B*, vol. 63, no. 1, pp. 2–11, 1949.

[33] R. M. Spriggs, “Expression for Effect of Porosity on Elastic Modulus of Polycrystalline Refractory Materials, Particularly Aluminum Oxide.,” *Sci. Sinter.*, vol. 18, no. 1, pp. 68–70, 1986.

[34] N. E. Promisel, *Evaluation of Non-Ferrous Materials*. Metals Park, OH: ASM International, 1956.

[35] W. D. K. R. L. Coble, “Effect of porosity on physical properties of sintered alumina,” *J. Am. Ceram. Soc.*, vol. 39, no. 11, p. 377, 1956.

[36] D. A. Lados and D. Apelian, “Fatigue crack growth characteristics in cast Al-Si-Mg alloys Part I. Effect of processing conditions and microstructure,” *Mater. Sci. Eng. A*, vol. 385, no. 1–2, pp. 200–211, 2004.

[37] M. Lamm and R. F. Singer, “The effect of casting conditions on the high-cycle fatigue properties of the single-crystal nickel-base superalloy PWA 1483,” *Metall. Mater. Trans. A Phys. Metall. Mater. Sci.*, vol. 38, no. 6, pp. 1177–1183, 2007.

[38] S. Usami and S. Shida, “Elastic-Plastic Analysis of the Fatigue Limit for a Material With Small Flaws,” *Fatigue Fract. Eng. Mater. Struct.*, vol. 1, no. 4, pp. 471–481, 1979.

[39] E. Pessard, F. Morel, A. Morel, and D. Bellett, “Anisotropic High Cycle Fatigue Behavior and Related Crack Initiation Mechanisms in Forged Steel,” *Icf12*, pp. 1–10, 2009.

[40] E. Wycisk, A. Solbach, S. Siddique, D. Herzog, F. Walther, and C. Emmelmann, “Effects of defects in laser additive manufactured Ti-6Al-4V on fatigue properties,” *Phys. Procedia*, vol. 56, no. C, pp. 371–378, 2014.

[41] E. Brandl, U. Heckenberger, V. Holzinger, and D. Buchbinder, “Additive manufactured AlSi10Mg samples using Selective Laser Melting (SLM): Microstructure, high cycle fatigue, and fracture behavior,” *Mater. Des.*, vol. 34, pp. 159–169, 2012.

[42] W. Tillmann, C. Schaak, J. Nellesen, M. Schaper, M. E. Aydinöz, and K.-P. Hoyer, “Hot isostatic pressing of IN718 components manufactured by selective laser melting,” *Addit. Manuf.*, vol. 13, pp. 93–102, 2017.

[43] M. Xia, D. Gu, G. Yu, D. Dai, H. Chen, and Q. Shi, “Porosity evolution and its thermodynamic mechanism of randomly packed powder-bed during selective laser melting of Inconel 718 alloy,” *Int. J. Mach. Tools Manuf.*, 2017.

[44] T. M. Pollock and S. Tin, “Nickel-Based Superalloys for Advanced Turbine Engines: Chemistry, Microstructure and Properties,” *J. Propuls. Power*, vol. 22, no. 2, pp. 361–374, 2006.

[45] E. G. Kirsch, “Die Theorie der Elastizitat und die Bedurfnisse der Festigkeitslehre,” *Zeitschrift des Vereines Dtsch. Ingenieure*, vol. 42, pp. 797–807, 1898.

[46] B. McGinty, “Stress Concentrations at Holes,” *FractureMechanics.org*. [Online]. Available: http://www.fracturemechanics.org/hole.html. [Accessed: 21-Jul-2017].

[47] S. Gribbin, J. Bicknell, L. Jorgensen, I. Tsukrov, and M. Knezevic, “Low cycle fatigue behavior of direct metal laser sintered Inconel alloy 718,” *Int. J. Fatigue*, vol. 93, pp. 156–167, 2016.

[48] O. Scott-Emuakpor *et al.*, “Material Property Determination of Vibration Fatigued DMLS and Cold-Rolled Nickel Alloys,” in *Volume 7A: Structures and Dynamics*, 2014, p. V07AT28A008.

[49] P. F. Kelley, A. Saigal, J. K. Vlahakis, and A. Carter, “Tensile and Fatigue Behavior of Direct Metal Laser Sintered (DMLS) Inconel 718,” in *Volume 2A: Advanced Manufacturing*, 2015, p. V02AT02A001.

[50] O. Scott-Emuakpor, C. Holycross, T. George, K. Knapp, and J. Beck, “Fatigue and Strength Studies of Titanium 6Al–4V Fabricated by Direct Metal Laser Sintering,” *J. Eng. Gas Turbines Power*, vol. 138, no. 2, p. 22101, Sep. 2015.

[51] D. Eylon and B. Strope, “Fatigue crack initiation in Ti-6wt % AI -4 wt % V castings,” *J. Mater. Sci.*, vol. 14, pp. 345–353, 1979.

[52] D. L. (University of V. Chen, “No Title,” University of Vienna, 1993.

[53] P. Krakhmalev, G. Fredriksson, I. Yadroitsava, N. Kazantseva, A. Du Plessis, and I. Yadroitsev, “Deformation behavior and microstructure of Ti6Al4V manufactured by SLM,” *Phys. Procedia*, vol. 83, pp. 778–788, 2016.

[54] P. Li, D. H. Warner, A. Fatemi, and N. Phan, “Critical assessment of the fatigue performance of additively manufactured Ti-6Al-4V and perspective for future research,” *Int. J. Fatigue*, vol. 85, 2016.

[55] M. E. Aydinöz *et al.*, “On the microstructural and mechanical properties of post-treated additively manufactured Inconel 718 superalloy under quasi-static and cyclic loading,” *Mater. Sci. Eng. A*, vol. 669, pp. 246–258, 2016.

[56] M. Sadowski, L. Ladani, W. Brindley, and J. Romano, “Optimizing quality of additively manufactured Inconel 718 using powder bed laser melting process,” *Addit. Manuf.*, vol. 11, pp. 60–70, 2016.

[57] J.-P. Choi *et al.*, “Densification and microstructural investigation of Inconel 718 parts fabricated by selective laser melting,” *Powder Technol.*, vol. 310, pp. 60–66, 2017.

[58] G. Marchese *et al.*, “Microstructural investigation of as-fabricated and heat-treated Inconel 625 and Inconel 718 fabricated by direct metal laser sintering: contribution of Politecnico di Torino and Istituto Italiano di Tecnologia (IIT) di Torino,” *Met. Powder Rep.*, vol. 71, no. 4, pp. 273–278, 2016.

[59] C. Sanz and V. García Navas, “Structural integrity of direct metal laser sintered parts subjected to thermal and finishing treatments,” *J. Mater. Process. Technol.*, vol. 213, no. 12, pp. 2126–2136, 2013.

[60] T. Trosch, J. Strößner, R. Völkl, and U. Glatzel, “Microstructure and mechanical properties of selective laser melted Inconel 718 compared to forging and casting,” *Mater. Lett.*, vol. 164, pp. 428–431, 2016.

[61] J. Strößner, M. Terock, and U. Glatzel, “Mechanical and Microstructural Investigation of Nickel-Based Superalloy IN718 Manufactured by Selective Laser Melting (SLM),” *Adv. Eng. Mater.*, vol. 17, no. 8, pp. 1099–1105, 2015.

[62] D. H. Smith *et al.*, “Microstructure and mechanical behavior of direct metal laser sintered Inconel alloy 718,” *Mater. Charact.*, 2016.

[63] L. L. Parimi, G. Ravi, D. Clark, and M. M. Attallah, “Microstructural and texture development in direct laser fabricated IN718,” *Mater. Charact.*, vol. 89, 2014.

[64] R. Cunningham, S. P. Narra, C. Montgomery, J. Beuth, and A. D. Rollett, “Synchrotron-Based X-Ray Microtomography Characterization of the Effect of Processing Variables on Porosity Formation in Laser Power-Bed Additive Manufacturing of Ti-6Al-4V,” *Jom*, vol. 69, no. 3, pp. 2–7, 2016.

[65] T. Vilaro, C. Colin, and J. D. Bartout, “As-fabricated and heat-treated microstructures of the Ti-6Al-4V alloy processed by selective laser melting,” *Metall. Mater. Trans. A Phys. Metall. Mater. Sci.*, vol. 42, no. 10, pp. 3190–3199, 2011.

[66] G. Kasperovich and J. Hausmann, “Improvement of fatigue resistance and ductility of TiAl6V4 processed by selective laser melting,” *J. Mater. Process. Technol.*, vol. 220, pp. 202–214, 2015.

[67] A. Mertens *et al.*, “Mechanical properties of alloy Ti–6Al–4V and of stainless steel 316L processed by selective laser melting: influence of out-of-equilibrium microstructures This paper is part of a special issue on Euromat 2013: Emerging technologies in powder metallurgy.”

[68] J. Yang *et al.*, “Role of molten pool mode on formability, microstructure and mechanical properties of selective laser melted Ti-6Al-4V alloy,” *Mater. Des.*, vol. 110, pp. 558–570, 2016.

[69] A. A. Antonysamy, “Microstructure, Texture and Mechanical Property Evolution during Additive Manufacturing of Ti6Al4V Alloy for Aerospace Applications,” 2012.

[70] L. Facchini *et al.*, “Ductility of a Ti-6Al-4V alloy produced by selective laser melting of prealloyed powders,” *Rapid Prototyp. J. Rapid Prototyp. J. Rapid Prototyp. J.*, vol. 1613552541, no. 14, pp. 450–45942, 1108.

[71] X. Zhao, J. Chen, X. Lin, and W. Huang, “Study on microstructure and mechanical properties of laser rapid forming Inconel 718,” *Mater. Sci. Eng. A*, vol. 478, no. 1–2, pp. 119–124, 2008.

[72] D. K. Do and P. Li, “The effect of laser energy input on the microstructure, physical and mechanical properties of Ti-6Al-4V alloys by selective laser melting,” *Virtual Phys. Prototyp.*, vol. 11, no. 1, pp. 41–47, Jan. 2016.

[73] S. L. Campanelli, N. Contuzzi, A. Angelastro, and A. D. Ludovico, “Capabilities and Performances of the Selective Laser Melting Process,” *ew Trends Technol. Devices, Comput. Commun. Ind. Syst.*, p. Chapter 13, 2010.

[74] J. Kruth, M. Badrossamay, E. Yasa, J. Deckers, L. Thijs, and J. Van Humbeeck, “Part and material properties in selective laser melting of metals,” *16th Int. Symp. Electromachining*, pp. 1–12, 2010.

[75] W. J. Sames *et al.*, “Feasibility of in situ controlled heat treatment (ISHT) of Inconel 718 during electron beam melting additive manufacturing,” *Addit. Manuf.*, vol. 13, pp. 1–10, 2016.

[76] W. E. King *et al.*, “Observation of keyhole-mode laser melting in laser powder-bed fusion additive manufacturing,” *J. Mater. Process. Technol.*, vol. 214, no. 12, pp. 2915–2925, 2014.

[77] Y. Kawahito, M. Mizutani, and S. Katayama, “High quality welding of stainless steel with 10 kW high power fibre laser,” *Sci. Technol. Weld. Join.*, vol. 14, no. 4, pp. 288–294, 2009.

[78] J. Eastman, “Conduction Mode vs. Keyhole Mode Laser Welding | News from EWI - Materials Joining, Forming, Testing, Modeling, and Engineering Consulting Services,” *EWI*, 2015. [Online]. Available: https://ewi.org/conduction-mode-vs-keyhole-mode-laser-welding/. [Accessed: 18-Jun-2017].

[79] F. Lu, X. Li, Z. Li, X. Tang, and H. Cui, “Formation and influence mechanism of keyhole-induced porosity in deep-penetration laser welding based on 3D transient modeling,” *Int. J. Heat Mass Transf.*, vol. 90, pp. 1143–1152, 2015.

[80] H. Gong, K. Rafi, H. Gu, T. Starr, and B. Stucker, “Analysis of defect generation in Ti-6Al-4V parts made using powder bed fusion additive manufacturing processes,” *Addit. Manuf.*, vol. 1, 2014.

[81] D. Gu and Y. Shen, “Processing conditions and microstructural features of porous 316L stainless steel components by DMLS,” *Appl. Surf. Sci.*, vol. 255, no. 5 PART 1, pp. 1880–1887, 2008.

[82] S. Tammas-Williams, H. Zhao, F. Léonard, F. Derguti, I. Todd, and P. B. Prangnell, "XCT analysis of the influence of melt strategies on defect population in Ti-6Al-4V components manufactured by Selective Electron Beam Melting," *Mater. Charact.*, 2015.

[83] J. Karlsson, A. Snis, H. Engqvist, and J. Lausmaa, "Characterization and comparison of materials produced by Electron Beam Melting (EBM) of two different Ti-6Al-4V powder fractions," *J. Mater. Process. Technol.*, vol. 213, no. 12, pp. 2109–2118, 2013.

[84] H. Attar, M. Calin, L. C. Zhang, S. Scudino, and J. Eckert, "Manufacture by selective laser melting and mechanical behavior of commercially pure titanium," *Mater. Sci. Eng. A*, vol. 593, pp. 170–177, 2013.

[85] X. Zhou *et al.*, "3D-imaging of selective laser melting defects in a Co-Cr-Mo alloy by synchrotron radiation micro-CT," *Acta Mater.*, vol. 98, pp. 1–16, 2015.

[86] H. Gong, K. Rafi, T. Starr, and B. Stucker, "The effects of processing parameters on defect regularity in Ti-6Al-4V parts fabricated by Selective Laser Melting and Electron Beam Melting," 2013. [Online]. Available: https://www.scopus.com/record/display.uri?eid=2-s2.0-84898473207&origin=inward&txGid=F0B9DFFCB1C492DBB92AB6287994E3D9.wsnAw8kcdt7IPYLO0V48gA%3A2.

[87] L. C. Zhang and T. B. Sercombe, "Selective Laser Melting of Low-Modulus Biomedical Ti-24Nb-4Zr-8Sn Alloy: Effect of Laser Point Distance," *Key Eng. Mater.*, vol. 520, pp. 226–233, 2012.

[88] J.-P. Kruth *et al.*, "Binding mechanisms in selective laser sintering and selective laser melting," *Rapid Prototyp. J. Rapid Prototyp. J. Iss Rapid Prototyp. J.*, vol. 11, no. 5, pp. 314–326, 2005.

[89] G. A. Rao, K. Satyaprasad, M. Kumar, M. Srinivas, and D. S. Sarma, "Characterization of hot isostatically pressed nickel base superalloy Inconel 718," *Mater. Sci. Technol.*, vol. 19, no. March, pp. 313–321, 2003.

[90] P. Mercelis and J. Kruth, "Residual stresses in selective laser sintering and selective laser melting," *Rapid Prototyp. J.*, vol. 12, no. 5, pp. 254–265, 2006.

[91] M. Shiomi, K. Osakada, K. Nakamura, T. Yamashita, and F. Abe, "Residual Stress within Metallic Model Made by Selective Laser Melting Process," *CIRP Ann. - Manuf. Technol.*, vol. 53, no. 1, pp. 195–198, 2004.

[92] D. D. Gu, W. Meiners, K. Wissenbach, and R. Poprawe, "Laser additive manufacturing of metallic components: materials, processes and mechanisms," *Int. Mater. Rev.*, vol. 57, no. 3, pp. 133–164, 2012.

[93] I. Maskery *et al.*, "Quantification and characterisation of porosity in selectively laser melted Al-Si10-Mg using X-ray computed tomography," *Mater. Charact.*, vol. 111, pp. 193–204, 2016.

[94] R. P. Taylor, S. T. McClain, and J. T. Berry, “Uncertainty analysis of metal-casting porosity measurements using Archimedes’ principle,” *Int. J. Cast Met. Res.*, vol. 11, no. 4, pp. 247–257, 1999.

[95] G. A. Rao, M. Kumar, M. Srinivas, and D. S. Sarma, “Effect of standard heat treatment on the microstructure and mechanical properties of hot isostatically pressed superalloy inconel 718,” *Mater. Sci. Eng. A*, vol. 355, no. 1–2, pp. 114–125, 2003.

[96] R. Cunningham, S. P. Narra, T. Ozturk, J. Beuth, and A. D. Rollett, “Evaluating the Effect of Processing Parameters on Porosity in Electron Beam Melted Ti-6Al-4V via Synchrotron X-ray Microtomography,” *JOM*, vol. 68, no. 3, pp. 765–771, Mar. 2016.

[97] M. Wevers, G. Kerckhofs, and G. Pyka, “X-ray computed tomography for non-destructive testing,” *... Comput. Tomogr.*, pp. 13–29, 2012.

[98] J. Kastner, B. Plank, and G. Requena, “Non-destructive characterisation of polymers and Al-alloys by polychromatic cone-beam phase contrast tomography,” *Mater. Charact.*, vol. 64, pp. 79–87, 2012.

[99] L. Jiang, N. Chawla, M. Pacheco, and V. Noveski, “Three-dimensional (3D) microstructural characterization and quantification of reflow porosity in Sn-rich alloy/copper joints by X-ray tomography,” *Mater. Charact.*, vol. 62, no. 10, pp. 970–975, 2011.

[100] S. Vasić, B. Grobéty, J. Kuebler, T. Graule, and L. Baumgartner, “XRCT characterisation of Ti particles inside porous Al2O 3,” *Mater. Charact.*, vol. 61, no. 6, pp. 653–660, 2010.

[101] A. du Plessis and P. Rossouw, “Investigation of Porosity Changes in Cast Ti6Al4V Rods After Hot Isostatic Pressing,” *J. Mater. Eng. Perform.*, vol. 24, no. 8, pp. 3137–3141, 2015.

[102] G. Ziółkowski, E. Chlebus, P. Szymczyk, and J. Kurzac, “Application of X-ray CT method for discontinuity and porosity detection in 316L stainless steel parts produced with SLM technology,” *Arch. Civ. Mech. Eng.*, vol. 14, pp. 608–614, 2014.

[103] “CIMP-3D | Powder Bed Fusion Systems.” [Online]. Available: http://www.cimp-3d.org/pbf. [Accessed: 27-Jun-2017].

[104] D. M. Lambert and M. A. Adler, “IN718 Additive Manufacturing Properties and Influences,” 2014.

[105] J. Davis, *Nickel, Cobalt, and Their Alloys*. Materials Park, OH: ASM International, 2000.

[106] J. D. Verhoeven, *Fundamentals of Physical Metallurgy*. New York: Wiley, 1975.

[107] “Properties, Identification, and Heat Treatment of Metals,” in *US Army - Fundamentals of Machine Tools TC 9-524*, 1996, pp. 1–14.

[108] “Aerospace Material Specification AMS2801 - Heat Treatment of Titanium Alloy Parts.” SAE International, 2014.

[109] P. Suwanpinij, “The Synchrotron Radiation for Steel Research,” *Adv. Mater. Sci. Eng.*, vol. 2016, 2016.

[110] J. P. Kruth, M. Bartscher, S. Carmignato, R. Schmitt, L. De Chiffre, and A. Weckenmann, “Computed tomography for dimensional metrology,” *CIRP Ann. - Manuf. Technol.*, vol. 60, pp. 821–842, 2011.

[111] “phoenix v tome x m industrial CT scanner| GE Digital Solutions,” *GEMeasurement.com*. [Online]. Available: https://www.gemeasurement.com/inspection-ndt/radiography-and-computed-tomography/phoenix-vtomex-m. [Accessed: 23-Jul-2017].

[112] “CIMP-3D | Inspection Systems.” [Online]. Available: http://www.cimp-3d.org/inspection. [Accessed: 27-Jun-2017].

[113] N. Megherbi, T. P. Breckon, G. T. Flitton, and A. Mouton, “Radon transform based automatic metal artefacts generation for 3D threat image projection,” 2013, p. 89010B.

[114] “TomoPy Documentation.” 2017.

[115] B. Münch, P. Trtik, F. Marone, and M. Stampanoni, “Stripe and ring artifact removal with combined wavelet-Fourier filtering,” *EMPA Act.*, vol. 17, no. 2009–2010 EMPA ACTIVITIES, pp. 34–35, 2009.

[116] D. Paganin, S. C. Mayo, T. E. Gureyev, P. R. Miller, and S. W. Wilkins, “Simultaneous phase and amplitude extraction from a single defocused image of a homogeneous object,” *J. Microsc.*, vol. 206, no. 1, pp. 33–40, 2002.

[117] B. a Dowd, G. H. Campbell, D. P. Siddons, and R. B. Marr, “COMPUTED MICROTOMOGRAPHY AT THE National Synchrotron Light Source,” no. July 1999.

[118] “Software | EXTREMA.” [Online]. Available: http://extrema.ua.ac.be/?q=software. [Accessed: 23-Jun-2017].

[119] E. Maire and P. J. Withers, “Quantitative X-ray tomography,” vol. 59, no. 1, pp. 1–43, 2014.

[120] C. A. Schneider, W. S. Rasband, and K. W. Eliceiri, “NIH Image to ImageJ: 25 years of image analysis,” *Nat. Methods*, vol. 9, no. 7, 2012.

[121] “Avizo.” FEI, 2017.

[122] “UnsharpMask (ImageJ API).” [Online]. Available: https://imagej.nih.gov/ij/developer/api/ij/plugin/filter/UnsharpMask.html. [Accessed: 12-Jul-2017].

[123] A. User, “Avizo ® 9.”

[124] L. Shapiro and G. Stockman, “Computer Vision,” vol. 9, p. 609, 2000.

[125] P. Iassonov, T. Gebrenegus, and M. Tuller, “Segmentation of X-ray computed tomography images of porous materials: A crucial step for characterization and quantitative analysis of pore structures,” *Water Resour. Res.*, 2009.

[126] W. R. T. Ferreira, “ImageJ User Guide IJ 1.46r,” *IJ 1.46r*, p. 185, 2012.

[127] N. T. H. U. Huang, Liang-Kai (Department of Industrial Engineering and N. T. H. U. Wang, Mao-Jiun J. (Department of Industrial Engineering, “Image Thresholding by Minimizing the Measure of Fuzziness,” *Pattern Recognit.*, vol. 28, no. 1, pp. 41–51, 1995.

[128] J. M. S. Prewitt and M. L. Mendelsohn, “The Analysis of Cell Images,” *Ann. N. Y. Acad. Sci.*, vol. 128, no. 3, pp. 1035–1053, 1966.

[129] W.-H. Tsai, “Moment-preserving thresolding: A new approach,” *Comput. Vision, Graph. Image Process.*, vol. 29, no. 3, pp. 377–393, 1985.

[130] C. H. Li and P. K. S. Tam, “An iterative algorithm for minimum cross entropy thresholding,” *Pattern Recognit. Lett.*, vol. 19, no. 8, pp. 771–776, 1998.

[131] J. N. Kapur, P. K. Sahoo, and A. K. C. Wong, “A new method for gray-level picture thresholding using the entropy of the histogram,” *Comput. Vision, Graph. Image Process.*, vol. 29, no. 1, p. 140, 1985.

[132] P. Sahoo, C. Wilkins, and J. Yeager, “Threshold selection using Renyi’s entropy,” *Pattern Recognit.*, vol. 30, no. 1, pp. 71–84, 1997.

[133] A. G. Shanbhag, “Utilization of Information Measure as a Means of Image Thresholding,” *CVGIP Graph. Model. Image Process.*, vol. 56, no. 5, pp. 414–419, Sep. 1994.

[134] S. Ridler, T.W. Calvard, “Picture Thresholding Using an Iterative Slection Method,” *IEEE Trans. Syst. Man Cybern.*, vol. 8, no. 8, pp. 630–632, 1978.

[135] N. Otsu, “A Threshold Selection Method from Gray-Level Histograms,” *IEEE Trans. Syst. Man. Cybern.*, vol. 9, no. 1, pp. 62–66, Jan. 1979.

[136] W. Doyle, “Operations Useful for Similarity-Invariant Pattern Recognition,” *J. ACM*, vol. 9, no. 2, pp. 259–267, 1962.

[137] J. Glasbey, C.A. (Scottish Agricultural Statistics Service, “An Analysis of Histogram-Based Thresholding Algorithms,” *Graph. Model. Image Process.*, vol. 55, no. 6, pp. 532–537, 1993.

[138] J. Kittler and J. Illingworth, “Minimum error thresholding,” *Pattern Recognit.*, vol. 19, no. 1, pp. 41–47, 1986.

[139] G. W. Zack and E. Rogers, “Automatic Measurement of Sister Chromatid Exchange Frequency,” *J. Histochem. Cytochem.*, vol. 25, no. 7, pp. 741–753, 1977.

[140] C. F. C. S. Jui-Cheng Yen, Fu-Juay Chang, and Shyang Chang, “A new criterion for automatic multilevel thresholding,” *IEEE Trans. Image Process.*, vol. 4, no. 3, pp. 370–378, Mar. 1995.

[141] J. Bernsen, “Dynamic Thresholding of Grey-Level Images,” in *Proceedings of the 8th International Conference on Pattern Recognition*, 1986.

[142] G. Landini, C. Rueden, J. Schindelin, M. Hiner, and S. Helfrich, “Auto Local Threshold,” 2017. .

[143] R. Fisher, S. Perkins, A. Walker, and E. Wolfart, “Point Operations - Adaptive Thresholding,” 2003. [Online]. Available: http://homepages.inf.ed.ac.uk/rbf/HIPR2/adpthrsh.htm. [Accessed: 25-Jul-2017].

[144] W. Niblack, *An introduction to Digital Image Processing*. Prentice-Hall, 1986.

[145] N. Phansalkar, S. More, A. Sabale, and D. M. Joshi, “Adaptive Local Thresholding for Detection of Nuclei in Diversely Stained Cytology Images,” *Commun. Signal Process.*, pp. 218–220, 2011.

[146] J. Sauvola and M. Pietikäinen, “Adaptive document image binarization,” *Pattern Recognit.*, vol. 33, no. 2, pp. 225–236, 2000.

[147] “Cassini Lossy Compression.” [Online]. Available: http://www.astro.cornell.edu/research/projects/compression/entropy.html. [Accessed: 26-Jul-2017].

[148] “Amira & Avizo 3D Software,” Jul. 2017.

[149] Z. Chen, “Mechanical Properties of La0.6Sr0.4Co0.2Fe0.8O3 Fuel Cell Electrodes,” no. April, 2014.

[150] C. Schaak and W. Tillmann, “Functional Encapsulation of Laser Melted Inconel 718 by Arc-PVD and HVOF for Post Compacting by Hot Isostatic Pressing,” no. September, pp. 1–7, 2014.

[151] J. Kelley, Paul F., *Fatigue Behavior of Direct Metal Laser Sintered (DMLS) Inconel 718*. 2016.